NOAA Technical Memorandum ERL ETL-276

RADAR REMOTE SENSING OF SCALAR AND VELOCITY MICROTURBULENCE IN THE CONVECTIVE BOUNDARY LAYER

A.B. White

Environmental Technology Laboratory
Boulder, Colorado
January 1997

noaa NATIONAL OCEANIC AND ATMOSPHERIC ADMINISTRATION / Environmental Research Laboratories

NOAA Technical Memorandum ERL ETL-276

RADAR REMOTE SENSING OF SCALAR AND VELOCITY MICROTURBULENCE IN THE CONVECTIVE BOUNDARY LAYER

Allen B. White

Cooperative Institute for Research in Environmental Sciences (CIRES)
The University of Colorado/NOAA Environmental Technology Laboratory

Environmental Technology Laboratory
Boulder, Colorado
January 1997

NOTICE

Mention of a commercial company or product does not constitute an endorsement by NOAA/ERL. Use for publicity or advertising purposes, of information from this publication or concerning proprietary products or the tests of such products, is not authorized.

CONTENTS

PAGE

LIST OF SYMBOLS vi

LIST OF ACRONYMS x

ABSTRACT 1

1. INTRODUCTION 2

1.1 Motivation and Objectives 3
1.2 Radar Applications 4

1.2.1 Wind Profiling 4
1.2.2 Precipitation 4
1.2.3 Turbulence 5
1.2.4 Problems 7

1.3 Organization of the Memorandum 9

2. STATISTICAL PROPERTIES OF TURBULENCE 9

2.1 Random Processes 9

2.1.1 Stationarity 11
2.1.2 Stationary Increments 13

2.2 Random Fields 14

2.2.1 Homogeneity 15
2.2.2 Isotropy 17
2.2.3 Local Homogeneity and Isotropy 19

2.3 Application of the Statistical Theory to Measurements 20

2.3.1 Spectral Coordinates 20
2.3.2 Taylor's Hypothesis 21
2.3.3 Properties of the Inertial Subrange 22

PAGE

3. BEHAVIOR OF STRUCTURE FUNCTION PARAMETER PROFILES AND DISSIPATION RATE PROFILES IN THE CONVECTIVE BOUNDARY LAYER 25

3.1 Scalar Structure Function Parameter Profiles 26

3.1.1 Surface Layer 26
3.1.2 Mixed Layer 28
3.1.3 Interfacial Layer 29
3.1.4 The Top-Down/Bottom-Up Approach 30

3.2 Dissipation Rate Profiles 33

3.2.1 Surface Layer 33
3.2.2 Mixed Layer and Interfacial Layer 34

4. THE NOAA 915-MHZ BOUNDARY-LAYER RADAR/WIND PROFILER 35

4.1 System Description 35
4.2 Signal Processing 35

4.2.1 Detection and Ranging 35
4.2.2 Coherent Integration 38
4.2.3 Spectral Processing 39
4.2.4 Incoherent Integration 40
4.2.5 Radar Dwell Time 42

4.3 The Doppler Spectral Moment Algorithm 42

4.3.1 Signal, Noise, and the Spectral Moments 43
4.3.2 Ground-Clutter Suppression 43

4.4 Data Acquisition 44
4.5 The Doppler Radar Reflectivity Equation 44

5. MEASUREMENT ANALYSES 47

5.1 Tower Measurements 48

5.1.1 Turbulence Sensors 48
5.1.2 Mean Sensors and Instrument Comparisons 48
5.1.3 Structure Function Parameters 55

PAGE

5.2 Comparison of the Refractive Index Turbulence Measurements 58

5.2.1 Data Selection 58
5.2.2 Radar Pulse Coding and Receiver Recovery 59
5.2.3 A Radar C_n^2 Calibration 63

5.3 Radar Measurement of Velocity Turbulence 65

5.3.1 The Radar Averaging Filter 65
5.3.2 Spectral Width Estimation of C_u^2 73
5.3.3 Radar/Tower C_u^2 Intercomparison 78

6. RADAR OPERATING PARAMETER SENSITIVITY STUDIES 81

6.1 Coherent Integration Period 84
6.2 FFT Length 90
6.3 Dwell Time 96
6.4 Discussion 98

7. SUMMARY AND CONCLUSIONS 103

ACKNOWLEDGMENTS 105

REFERENCES 106

APPENDIX: ERROR ANALYSIS 116

A.1 Sampling Uncertainty 116
A.2 Radar C_n^2 118
A.3 Tower C_n^2 121
A.4 Tower C_u^2 123
A.5 Radar C_u^2 124

LIST OF SYMBOLS[†]

a	Gaussian beamwidth (5.16)
a_T	structure function parameter coefficient (5.6)
A	empirical constant in inertial range relation for velocity (2.47)
A_e	effective antenna area (4.17)
A_E	Kolmogorov constant in the inertial range relation for the energy spectrum (Section 5.3.1)
A_p	physical antenna area (Table 4.1)
$A(\mathbf{r})$	beam illumination function (Section 5.3.1)
b	Gaussian pulse length (5.16)
b_Q	structure function parameter coefficient (5.6)
B	empirical constant in inertial range relation for scalars (2.49)
B_N	receiver noise bandwidth (4.20)
c	speed of light (4.2)
C	correlation (Table 5.1)
C_R	radar operating parameter constant (5.9)
$(C_n^2)_T$	tower measurement of the refractive index structure function parameter (Section 5.1.3)
C_x^2	structure function parameter for x (Section 1.2.3)
C_{TQ}	structure function parameter for temperature-humidity correlation (Section 3.1)
D	detectability (4.6)
$D_{ij}(\ )$	structure function tensor (2.38)
$D_x(\ )$	structure function for x (2.11)
E	standard error given by linear regression (Table 5.1)
$E(k)$	energy spectrum (2.23)
f	frequency in cycles per unit time (Section 2.1.1)
$\overline{f'^2}$	ensemble variance of f about $\bar{f}$ (A.1)
f_D	Doppler frequency shift (4.5)
f_i	fluctuations in the ith direction of a vector random field (2.16)
f_N	radar Nyquist frequency (4.4)
$f(t)$	fluctuations of a scalar random process (2.1)
$\mathbf{F}(\mathbf{r})$	vector random field (Section 2.2)
$F(t)$	scalar random process (Section 2.1)
F_N	factor to correct scalar spectra for inaccuracies in Taylor's hypothesis and anisotropy in the inertial subrange (A.24)
F_u	factor to correct velocity spectra for inaccuracies in Taylor's hypothesis and anisotropy in the inertial subrange (A.26)
$F_P(\mathbf{k})$	Fourier transform of the beam illumination function (5.15)

[†]Unless otherwise specified, the reference to the location of the symbol in the text is the equation number where the symbol is first used. Because I have tried to keep the notation in this thesis consistent with that which appears in previously published literature, it was necessary on a limited number of occasions to reuse certain symbols. However, to help avoid possible confusion, each symbol is assigned only once within any given chapter.

$F_T(\mathbf{k})$	Fourier transform of the dwell-time window function (5.28)
g	acceleration due to gravity (Section 3.1.1)
G_o	antenna gain (4.15)
$G(\omega_k)$	filtered and aliased spectral estimate (5.10)
h_b, h_t, h_{tb}	dimensionless top-down/bottom-up gradient functions (3.23)
IPP	interpulse period (Table 4.1)
k	wavenumber magnitude (2.21)
k_a	von Kármán constant (3.2)
$\mathbf{k}$	angular wavenumber vector, $\mathbf{k} = (k_1, k_2, k_3)$ (2.18)
k_B	Boltzmann's constant (4.20)
k_N	wavenumber corresponding to the Nyquist frequency (Section 5.3.1)
K_T	transfer function for dwell-time averaging (5.13)
K_P	transfer function for pulse-volume averaging (5.20)
L	Monin-Obukhov length (3.2)
L	beamwidth broadening associated with the radar dwell time (5.30)
m	linear regression slope (Table 5.1)
m_*	mixed-layer humidity scale (3.13)
n	refractive index (Section 1.2.3)
n_c	number of coherent integrations (Table 4.1)
n_i	unit vector in ith direction (2.39)
n_f	number of Fast-Fourier transform points (Table 4.1)
n_p	number of points used to define the signal peak (A.18)
n_s	number of spectral averages (Table 4.1)
N	number (Table 5.1)
N	dissipation rate of temperature half-variance (Section 3.2.1)
N	noise power (Section 4.3.1)
N	refractivity (5.2)
P	total air pressure (5.3)
P_i	discrete spectral values of the signal in a Doppler velocity spectrum (4.11)
P_N	mean noise spectral density (Fig. 4.2)
P_r	received power (4.15)
P_S	peak spectral density of signal spectrum (4.6)
P_t	peak transmit power (Table 4.1)
q	specific humidity (Section 3.1.1)
Q	absolute humidity (Section 1.2.3)
Q_i	interfacial-layer humidity scale (3.20)
Q_*	surface-layer humidity scale (3.4)
$\mathbf{r}$	spatial position vector, $\mathbf{r} = (x_1, x_2, x_3)$ (Section 2.2)
r	correlation coefficient (Section 2.1)
$r(\ )$	autocorrelation coefficient (2.3)
R	radar range (4.2)
$R(\ )$	autocorrelation function (2.2)
R_g	gas constant for dry air (5.3)
$R_{ij}(\ )$	correlation tensor (2.16)

R_θ, R_Q	ratio of the entrainment flux to the surface flux (3.23)
RCSNR	range-corrected signal-to-noise ratio (5.9)
$s(t)$	complex signal plus noise of radar backscatter (4.1)
S	signal power (4.11)
$S(f)$, $S_x(f)$	measured frequency spectrum (Section 2.3.1)
$S_x(k_1)$	measured one-dimensional wavenumber spectrum for x (2.45)
SNR	signal-to-noise ratio (Section 1.2.3)
t	time (Section 2.1)
t_D	radar dwell time (4.10)
T	air temperature (Section 1.2.3)
T	averaging period (A.1)
T_i	interfacial-layer temperature scale (3.21)
T_o	radar system noise temperature (4.20)
T_o	length of record (5.11)
T_{rx}	receiver noise temperature (Table 4.1)
T_s	sky noise temperature (4.21)
T_*	surface-layer temperature scale (3.3)
$T(t)$	dwell time window function (5.29)
u	horizontal velocity component (Section 1.2.3)
$\overline{u}$	mean wind speed (Section 2.3.2)
u_i	fluctuating velocity component in the ith direction (Section 2.1.1)
u_*	friction velocity (3.1)
U	mean north-south wind component (Section 5.1.2)
v	horizontal velocity component (Section 1.2.3)
v_1, v_2	endpoints defining the signal in a Doppler velocity spectrum (4.11)
v_N	Nyquist velocity (Chapter 6)
v_r	radial velocity (4.5)
V	mean east-west wind component (Section 5.1.2)
V_T	wind speed transverse to the radar beam (5.22)
w	vertical velocity (Section 1.2.3)
w_a	spatially and temporally filtered vertical velocity measured by a Doppler radar (5.27)
w_*	convective scaling velocity (3.11)
W_e	entrainment velocity (3.28)
z	height (Section 3.1.1)
z_i	boundary-layer height (Section 3.1.2)
α	radar system efficiency (Section 4.5)
δ	separation between radar and tower (Section A.1)
δ_{ij}	delta function (2.27)
δ_s	separation between the turbulence sensors on the tower (Section A.3)
δG	uncertainty in the function G (A.10)
Δ	denotes a jump across the interfacial layer (3.17)
Δf	frequency interval (A.25)
ΔR	range resolution (Table 4.1)

Δt	coherent integration period (Section 4.2.2)
Δt	sampling period (5.11)
Δv	velocity resolution in the Doppler velocity spectrum (Chapter 6)
$\Delta\omega$	characteristic frequency (5.11)
ε	turbulent kinetic energy dissipation rate (Section 1.2.3)
ε_r	normalized random error (A.27)
η	radar reflectivity (Section 4.5)
θ	antenna beamwidth (Table 4.1)
θ_h	angular half-width of antenna beam (5.17)
θ_v	virtual potential temperature (3.2)
θ_{v*}	mixed-layer virtual temperature scale (3.17)
θ_*	mixed-layer temperature scale (3.12)
λ	radar wavelength (Table 4.1)
λ_l	integral length scale (A.5)
Λ	microscale (2.5)
ξ	spatial separation magnitude (Section 2.2.2)
$\boldsymbol{\xi}$	spatial separation vector (Section 2.2.1)
ρ	air density (Section 3.1.1)
σ_x^2	variance of x (Section 1.2.3)
σ_a^2	broadening of radar spectrum by antenna properties (5.21)
σ_{ij}^2	variance tensor (2.24)
σ_N	standard deviation of noise spectral density (4.6)
σ_s^2	broadening of radar spectrum by wind shear (5.21)
σ_t^2	total broadening of radar spectrum (5.21)
τ	lag (2.4)
τ	pulse width (Table 4.1)
τ_m	time scale corresponding to frequency at spectral peak (5.12)
ϕ	antenna beamwidth (non-conical beam) (4.15)
$\phi(\omega)$	temporal spectral density function (2.7)
$\phi_{ij}(k)$	one-dimensional spatial spectral density tensor (2.20)
$\Phi_{ij}(\mathbf{k})$	three-dimensional spatial spectral density tensor (2.19)
$\Phi_P(\mathbf{k})$	beam filter function (5.14)
χ	rate of dissipation of scalar variance (Section 1.2.3)
ψ	beam elevation angle (Table 4.1)
$\psi_{ij}(k)$	spherical average spectral density tensor (2.21)
ω	circular frequency (2.7)
ω_k	kth multiple of characteristic frequency (5.10)
ω_m	frequency at spectral peak (5.12)
ω_N	Nyquist frequency (5.10)
ω_s	sampling frequency (5.10)
$\mathfrak{I}$	integral time scale (2.5)

LIST OF ACRONYMS

A/D	analog-to-digital
AGL	above ground level
AMTEX	Air-Mass Transformation Experiment
ARM	Atmospheric Radiation Measurement (Program)
ATI	Applied Technologies, Inc.
BAO	Boulder Atmospheric Observatory
CBL	convective boundary layer
CP	coded pulse
DC	direct current
DSP	digital signal processing
ETL	Environmental Technology Laboratory
FFT	Fast-Fourier transform
FM-CW	frequency modulated - continuous wave
IF	intermediate frequency
IPP	interpulse period
LES	large-eddy simulation
MBL	marine boundary layer
MDT	Mountain Daylight Time
M-O	Monin-Obukhov (similarity)
NBL	NOAA 915-MHz boundary layer (radar)
NOAA	National Oceanic and Atmospheric Administration
PBL	planetary boundary layer
PC	personal computer
POP	profiler on-line program
RASS	radio acoustic sounding system
RF	radio frequency
RFI	radio frequency interference
SNR	signal-to-noise ratio
SP	standard pulse
TKE	turbulent kinetic energy
UHF	ultra-high frequency
VHF	very-high frequency

RADAR REMOTE SENSING OF SCALAR AND VELOCITY MICROTURBULENCE IN THE CONVECTIVE BOUNDARY LAYER

Allen B. White
Cooperative Institute for Research in Environmental Sciences
University of Colorado/NOAA Environmental Technology Laboratory
Boulder, Colorado

ABSTRACT. This memorandum describes a comparison of scalar and velocity microturbulence measurements in the convective planetary boundary layer obtained from a sonic anemometer and an infrared hygrometer mounted on a tower and from a Doppler radar/wind profiler located approximately 200 m from the tower. The signal-to-noise ratios taken from the Doppler velocity spectra measured by the radar are compared to values of the refractive-index structure function parameter, C_n^2, deduced from the temperature and humidity fluctuations measured on the tower. This comparison is used to derive an in situ calibration of radar reflectivity. The C_n^2 measurements from the radar and tower are well correlated ($r = 0.83$). The relative uncertainty in the reflectivity calibration based on the scatter observed in the C_n^2 comparison is ±14%. An experimental and theoretical analysis of the time-and-space filters that are applied to radar measurements of the vertical-velocity variance spectrum is given. An established technique for using radar spectral width to estimate the velocity structure function parameter, C_u^2, is modified to account for the radar time filter. The resulting radar C_u^2 measurements are moderately correlated with the tower measurements ($r = 0.73$). The scatter is mainly attributable to the sampling uncertainty associated with using a 15-min time average. Sensitivity studies were conducted by varying the Doppler signal processing parameters to determine if the radar equations behave properly when the processing parameters are changed. The radar C_n^2 equation used in this analysis correctly accounts for a change in the number of coherent integrations. The standard radar C_u^2 equation does not account for the increased spectral width sensitivity that is observed when the spectral resolution is increased. These studies also show that an increase in spectral resolution and a decrease in dwell time can improve the sensitivity and accuracy of turbulence variables derived from the radial velocity and spectral width measured by the radar. A factor-of-four increase in spectral resolution results in a factor-of-four increase in spectral width resolution and reduces the mean vertical-velocity bias that occurs partly because of insufficient resolution in the Doppler velocity spectrum.

1. INTRODUCTION

During the past two decades, radar remote sensing has played an increasingly important role in atmospheric research. Today, nearly every major field program deploys at least one type of profiling radar. Most of the radars used for atmospheric research operate in the 10 MHz to 100 GHz frequency range. Other distinguishing radar characteristics include size, hardware design, research applications, and cost. Table 1.1 lists three of the radars operated by the National Oceanic and Atmospheric Administration (NOAA). The NOAA 915-MHz boundary-layer radar/wind profiler (NBL radar) is the focus of this memorandum. The portability and relatively low cost of building and operating this particular radar make it ideal for field research. In addition, the NBL radar is now commercially available through a cooperative agreement between NOAA and Radian Corporation.

Table 1.1
Radar characteristics and operating parameters.

	NOAA 50-MHz radar/wind profiler	NOAA Wind Profiler Demonstration Network 404-MHz radar/wind profiler	NOAA 915-MHz boundary-layer radar/wind profiler
Installation site	Christmas Island, Kiribati	Platteville, CO	mobile
Wavelength (cm)	600 (VHF)	74.3 (UHF)	32.8 (UHF)
Antenna type	flat rectangular coaxial-collinear phased array	flat rectangular coaxial-collinear phased array	flat rectangular microstrip-patch phased array
Antenna diameter (m)	100	13.0	2.0
Beamwidth (deg.)	2.1	4.0	12.0
Pulse width (μs)	6.7	1.0-3.0	0.4-1.4
Transmitted peak signal power (kW)	30	12	0.5
Measurements	Doppler velocity radar reflectivity spectral width	Doppler velocity radar reflectivity spectral width	Doppler velocity radar reflectivity spectral width
Resolutions:			
Time (s)	420	360	180 (winds) 15 (turbulence)
Vertical (m)	1000	250	60-210
Estimated replacement cost (thousands)	1000	600	150

1.1 Motivation and Objectives

The NBL radar was designed by NOAA Aeronomy Laboratory engineers (Ecklund et al., 1988) with the primary objective of obtaining mean wind profiles in the lower troposphere. While quite useful, the mean winds are only part of the information required for many boundary-layer applications. Therefore, in this memorandum I investigate the NBL radar's potential for measuring turbulence statistics in the planetary boundary layer (PBL). Given the problems associated with radar measurements of turbulence (see Section 1.2.4), I concentrate on the convective PBL, which is the most well understood case (Wyngaard, 1992).

While many of the previous studies that used wind-profiling radars to measure turbulence variables have shown encouraging results (see Section 1.2.3), most have lacked to some extent one, two, or all three of the following key ingredients: a) an independent observational data base to evaluate the validity of the techniques employed, b) a careful examination of the accuracy of the basic radar measurements used in the analyses, and c) a statement of what is required to apply the empirical or fundamental radar equations used to generate the turbulence variables to general field use. The overall goal of this research, then, is to address these areas with particular attention to the radar measurement of the refractive index and velocity structure function parameters. I perform the following tasks to accomplish this goal:

1) Develop a robust radar reflectivity calibration, i.e., one that can be used when changes are made to signal processing parameters and/or components.

2) Quantify the effects of the filtering applied by the radar's spatial and temporal averaging on measurements of the vertical velocity variance spectrum.

3) Evaluate the use of radars to measure the velocity structure function parameter.

4) Test the universality of the relationships used to derive turbulence statistics from wind-profiler data.

5) Investigate ways in which the radar signal processing can be improved to increase performance for measuring turbulence variables.

For the first three tasks I compare radar measurements with in situ measurements from the 300-m tower at the Boulder Atmospheric Observatory (BAO). I conducted the field experiment for this portion of the research in June–July 1993. The radar and tower were separated horizontally by roughly 200 m. This separation was necessary to avoid interference by the tower and its guy wires on the backscatter returns from the radar. Therefore, even

under conditions where horizontal homogeneity is strictly satisfied, there may be differences in individual pairs of measurements from the radar and tower that illustrate the difficulty of obtaining an independent observational data base to compare with the radar. For the final two tasks I conducted an operating parameter sensitivity study with the NBL radar during a two-week period in June 1995.

1.2 Radar Applications

1.2.1 Wind profiling

The wind profiling capability of the NBL radar and its larger predecessors has been well established (Balsley and Gage, 1982; Weber et al., 1990; Martner et al., 1993) and has resulted in the deployment of an operational wind-profiler network (Chadwick, 1986). The portable NBL radars have been used in high-resolution research arrays such as those deployed during a three-year observational study of atmospheric transport in the valleys of California (Neff et al., 1994).

Even before most wind-profiler networks were available, Kuo et al. (1987) showed that the skill of a short-range numerical model forecast was improved when the model was initialized with data from a simulated wind-profiler network. More recently, complex four-dimensional data assimilation schemes have been developed to take full advantage of the continuous nature of the data provided by wind profilers and other observing networks (e.g., Stauffer and Seaman, 1994).

1.2.2 Precipitation

Because of its operating frequency, the NBL radar fits into the category commonly referred to as "clear-air" radars. The term clear-air is used to describe radars that receive backscatter from refractive-index fluctuations and thus do not require clouds or precipitation to receive a signal. This terminology can be misleading since clear-air radars are also sensitive in varying degrees to hydrometeors, biological targets such as insects and birds, man-made obstacles including buildings and aircraft, and other radio-frequency transmissions. These interfering signals have on occasion plagued meteorologists interested in measuring the winds (Wilczak et al., 1995). On the other hand, others have exploited this information and have ultimately extended the capabilities of wind-profiling radars beyond their originally intended use.

Consider, for example, precipitation. During precipitation, the radar returns are dominated, if not saturated, by backscatter from a dense population of large particles, treated ideally as Rayleigh scatterers. In this case, the Doppler velocity spectrum results from a combination of clear-air velocities (Bragg scattering) and precipitation velocities (Rayleigh scattering). The spectral peaks associated with each scattering mechanism may be visible in

the spectrum (Wakasugi et al., 1986, 1987; Forbes and Carroll, 1987). If separable, the precipitation scattering portion of the spectrum can be used to diagnose the magnitude and distribution of the particle fall velocities (Ralph, 1995). On the other hand, when the droplets are very small, their motions are dominated by turbulent fluctuations in the cloud rather than by their own fall velocities. In this case, the clear-air and cloud-droplet portions of the spectrum often overlap. Gossard and Strauch (1989) and Gossard (1994) developed techniques that employ spectral deconvolution to extract distribution parameters from both the precipitation and cloud-droplet portions of the spectrum.

1.2.3 Turbulence

Part of the desire to measure turbulence statistics with wind-profiling radars has come from the need to test the schemes used to parameterize turbulence in numerical models. For example, air pollution or dispersion models may require such information as the velocity variances, momentum and scalar fluxes, and convective mixed-layer depth. The structure function parameters, C_x^2, where x could be velocity (u, v, or w), temperature (T), humidity (Q) or refractive index (n), are also useful turbulence statistics for describing boundary-layer structure. In addition, the appropriate structure function parameters are related to the turbulent kinetic energy (TKE) and scalar dissipation rates, denoted by ε and χ, respectively (Corrsin, 1951). All of the these turbulence variables have been measured, with varying degrees of success, using wind-profiling radars. Examples of this research follow in the next several paragraphs.

Many studies have illustrated the detail that radars provide of the refractive-index turbulence structure of the atmosphere. A summary appears in Gossard et al. (1995). In addition, the measurement of C_n^2 from radar backscatter is described formally in many standard texts (e.g., Battan, 1973; Gossard and Strauch, 1983; Doviak and Zrnić, 1984). In order to obtain quantitatively accurate results, the radar must be calibrated. The calibration depends on assumptions about the transmitted beam and on properties of the radar hardware, including antenna efficiency and receiver bandwidth.

Because radars measure the three wind components (u, v, and w) via the Doppler technique, it is possible to take time series of these components and calculate the velocity variances, covariances, and even higher-order moments. However, the finite pulse volume imposes a low-pass filter on the spatial structure of turbulence measured by the radar. The velocity fluctuations are also averaged over a finite averaging time (typically ranging from 15 s to 75 s for the NBL radar) known as the dwell time, which imposes additional low-pass filtering on the fluctuations. Thus, the velocity time series measured by a wind-profiling radar contains only the variance corresponding to the low frequencies. The high-frequency structure is recoverable because lines in the Doppler velocity spectrum are broadened by the unresolved frequencies. White and Fairall (1991) found it necessary to account for spectral width in their variance calculations in order to produce the expected shape of the σ_w^2 profile in the convective boundary layer (CBL). If the unresolved frequencies lie in the inertial

subrange, then the spectral broadening can also be used to estimate ε or C_v^2 (e.g., Frisch and Clifford, 1974).

A comparison of different in situ and remote-sensing techniques for detecting the depth of the CBL was given by Kaimal et al. (1982). The remote sensors used in their study consisted of two radars (X-band and FM-CW), a sodar, and a lidar. They demonstrated the capability of these systems to detect boundary-layer depth within ±10%. White (1993) and Angevine et al. (1994) have demonstrated a similar capability for the NBL radar. The technique is based simply on finding the height of the peak associated with the inversion capping the mixed layer in successive signal-to-noise ratio (SNR), or C_n^2, profiles. Both of these studies compared the mixing depths deduced by the NBL radar with the inversion heights detected by rawinsondes and found the error associated with the radar measurement to be comparable to the vertical resolution of the radar. The depth of the CBL is a critical parameter for air pollution or dispersion modelling but is difficult to parameterize accurately. For example, during the 1990 San Joaquin Air Quality Study, the afternoon mixing depths predicted by the boundary-layer parameterization in The Pennsylvania State University/National Center for Atmospheric Research mesoscale model were consistently larger, by as much as a factor of two, than the inversion heights determined from a special set of rawinsonde launches (Seaman, 1992). Real-time detection of CBL depth, therefore, is an important potential application for ground-based remote sensors, including the NBL radar.

An important physical process related to boundary-layer growth is entrainment. Entrainment is difficult both to measure and to parameterize in models. The entrainment velocity is defined as the difference between the total time rate of change of the boundary-layer depth and the average vertical velocity at the top of the boundary layer. Recently, Angevine et al. (1996) attempted to measure the entrainment velocity with a triangle of NBL radars. They computed the horizontal wind divergence from the hourly averaged winds measured at the corners of the triangle (see Eq. 4 in Davies-Jones, 1993). Then they calculated the vertical velocity at the top of the boundary layer by integrating the horizontal wind divergence from the surface to the top of the boundary layer. They examined time-height cross sections of radar reflectivity to determine the evolution of boundary-layer height, but they neglected the advection term in the total derivative. Angevine et al. (1996) calculated reasonable rates of entrainment and detrainment for the CBL using this technique. The average over 26 days indicated an entrainment rate of 0.03 m s^{-1}.

Another way to estimate the entrainment rate explored by White et al. (1991) is to use radar measurements of structure function parameters near the top of the boundary layer in conjunction with an appropriate interfacial-layer model (e.g., Wyngaard and Lemone, 1980). This technique requires knowledge of the jumps in temperature and humidity occurring over the interfacial layer and the lapse rate of temperature above the inversion. However, Gossard et al. (1995) demonstrated how wind-profiling radars equipped with the radio acoustic sounding system (RASS) for measuring temperature can be used to measure temperature and humidity gradients aloft.

Angevine et al. (1993a,b) examined the possibility of using a profiler equipped with RASS to measure profiles of virtual temperature flux and momentum flux. The virtual temperature flux was calculated by the method of Peters et al. (1985), which does not include correlating virtual temperature with vertical velocity at zero lag, because measurement errors in the vertical velocity are directly correlated with errors in the temperatures retrieved from RASS. The momentum flux was computed by the variance differencing technique of Vincent and Reid (1983). The radar heat flux estimates agreed more favorably with coincident aircraft measurements than the momentum flux estimates. For the latter, Angevine (1993b) concluded that additional research was needed to establish whether the radar technique is feasible.

More testing needs to be done before many of these radar measurement techniques can be used for operational or research purposes. If proven viable, these methods could be used to create data bases of remotely-sensed turbulence variables. The data bases could, in turn, be used to evaluate the performance of the boundary- layer parameterizations contained in mesoscale numerical models (e.g., Burk and Thompson, 1989) and the turbulence structure inferred from large-eddy simulation (LES) (e.g., Peltier and Wyngaard, 1995).

1.2.4 Problems

There are several problems associated with using the measurements provided by wind-profiling radars to calculate turbulence variables. Some of these are specific to the NBL radar and others pertain to radars in general. The ultimate solutions to some of the problems can only be accomplished through changes in the radar hardware or signal processing algorithms. But even with the current technology, some improvements can be made by altering the signal processing parameters, which traditionally have been configured to maximize the radar's performance for mean wind profiling rather than for turbulence applications.

The most significant problem is the minimum pulse volume that can be achieved by the NBL radar. In order to minimize the size and cost of the instrument while enhancing its portability, the NBL radar was designed with a relatively small radar antenna (4 m^2). As a result, the beamwidth of the NBL radar is large compared to the beamwidths of other radars that use larger antennas. The larger beamwidth increases the range of velocity scales that are smaller than the pulse volume and, therefore, these scales are unresolved by the radar velocity measurement. As stated earlier, the unresolved scales can, in principle, be recovered, because they contribute to broadening of the Doppler velocity spectrum. However, because additional factors other than turbulence contribute to the broadening (which make it difficult to estimate the turbulence contribution), it is desirable to resolve as much of the velocity variance as possible with the radar velocity measurement.

Another problem associated with large pulse volumes is the increased susceptibility to contamination of the clear-air return by distributed particle scatterers. For example, the

diurnally averaged time series of vertical velocity measured by the NBL radar during the warm season indicated average downward velocities ranging from 0.2-0.4 m s^{-1} in the middle of the CBL. This behavior was observed at a rural site in Alabama (White and Fairall, 1991) and at an agricultural site in Illinois (Angevine, 1996). In a separate study, a comparison of the radar reflectivity measured by the NBL radar and a 10.6-cm radar indicated that the NBL radar detects Rayleigh scatterers in the CBL (Ecklund et al., 1995). It is conceivable, then, that instead of sensing clear-air motions exclusively, the NBL radar was measuring a combination of the atmospheric vertical velocity and the settling velocity of insects. Contamination of the refractive-index turbulence interpretation of the backscatter measured by the NBL radar can also come from clouds, although for clouds in the boundary layer, the clear-air contribution often dominates (see White et al., 1996).

The form of non-atmospheric radar backscatter referred to as ground clutter also interferes with clear-air measurements. Ground clutter occurs primarily in the side lobes of the NBL radar, but its characteristics vary with time and with the location of the radar. Therefore, it is often difficult to distinguish a ground-clutter signal from a clear-air signal in the Doppler velocity spectrum, especially when the two signals overlap. To help prevent the radar signal processing program from selecting a ground-clutter peak to calculate the Doppler spectral moments, the program removes or substantially reduces the spectral energy from the zero velocity spectral bin. As argued in Chapter 6, this procedure introduces a bias in the vertical velocity statistics produced from the radar time series.

Additional features of the Doppler signal processing create obstacles for measuring turbulence. For instance, the peak picking algorithm (see Section 4.3.1) simply chooses the largest spectral density in the spectrum without any consideration for whether the chosen peak is likely to have resulted from atmospheric backscatter. The radial velocity, SNR, and spectral width, collectively referred to as spectral moments, are all calculated from the signal part of the spectrum associated with this peak. To produce mean winds, a consensus algorithm is applied to filter outliers. On the other hand, the unaveraged time series of the three spectral moments must be inspected together carefully to remove outliers. For example, one set of moments might contain reasonable values of SNR and spectral width and an obvious velocity outlier. Instead of throwing out suspect data, the ambitious user has the option of recalculating a new set of spectral moments based on a different spectral peak as long as the full Doppler velocity spectra are recorded.

Spectral averaging is usually applied before the spectral moments are calculated. This process increases the detectability of the signal and ultimately improves the height coverage of the mean wind profiles produced by the consensus algorithm. However, this process also increases the dwell time by a factor equal to the number of spectra that are averaged, which again increases the low-pass filtering of the turbulence. The number of spectral averages is an external parameter that the user specifies.

1.3 Organization of the Memorandum

Following the introduction, three chapters are devoted to background material describing the structure of atmospheric turbulence and the NBL radar. Chapter 2 discusses the classic statistical theory governing atmospheric spectra and structure function parameters.

Chapter 3 summarizes the behavior of structure function parameter profiles and dissipation rate profiles in the CBL.

Chapter 4 describes the NBL radar and includes a detailed account of the signal processing that is applied to the raw backscatter signals in order to produce the Doppler velocity spectrum. I also give a derivation of the radar equation used to calculate C_n^2 from radar SNR in Chapter 4.

Chapters 5 and 6 contain the results of the analysis. Chapter 5 gives the results of the 1993 BAO tower experiment. I compare radar reflectivity with tower measurements of C_n^2 to calibrate the radar. I investigate the space-time filtering imposed by the radar sampling on the measured spectrum of vertical velocity. I also use the radar filter functions to calculate the beam-volume and dwell-time contributions to radar spectral width. After removing the undesired contributions to spectral broadening, I use the remaining spectral width to estimate C_w^2. I compare the radar velocity turbulence measurements with the corresponding measurements made on the BAO tower.

Chapter 6 reports on the radar operating parameter sensitivity study conducted in June 1995. The primary purpose of this study is to test the universality of the radar equations used to calculate C_n^2 and C_w^2 and to see, in general, how the radar spectral moments are affected by changes in the radar operating parameters. The results of this analysis also suggest how the radar could be operated to increase its performance for turbulence applications.

Chapter 7 summarizes the main findings of this research.

The Appendix contains an error analysis of the results presented in Chapter 5.

2. STATISTICAL PROPERTIES OF TURBULENCE

2.1 Random Processes

A time series of vertical velocity measured with a sonic anemometer at the Boulder Atmospheric Observatory (BAO) is shown in Fig. 2.1. The measured variable undergoes irregular oscillations which vary in amplitude and frequency and are superimposed in an apparently random manner. This time series, then, serves as an example of a realization of a random process. Because fluctuating quantities such as the example given in Fig. 2.1 are

stochastic in nature, statistical methods are used to describe their structure. I use the real random function $F(t)$ to describe briefly those methods that are pertinent to this work. A more complete description of the methods and of the underlying theory is given by Lumley and Panofsky (1964).

The most widely used statistic is the mean value $\overline{F(t)}$. The fluctuations $f(t)$ of the function $F(t)$ are given by the standard Reynolds decomposition,

$$f(t) = F(t) - \overline{F(t)}. \tag{2.1}$$

In theory, the overbar in (2.1) denotes an ensemble average; an average over many independent realizations of the function $F(t)$. However, in this and many other practical applications, the ensemble average is replaced by a finite time average. The validity of this

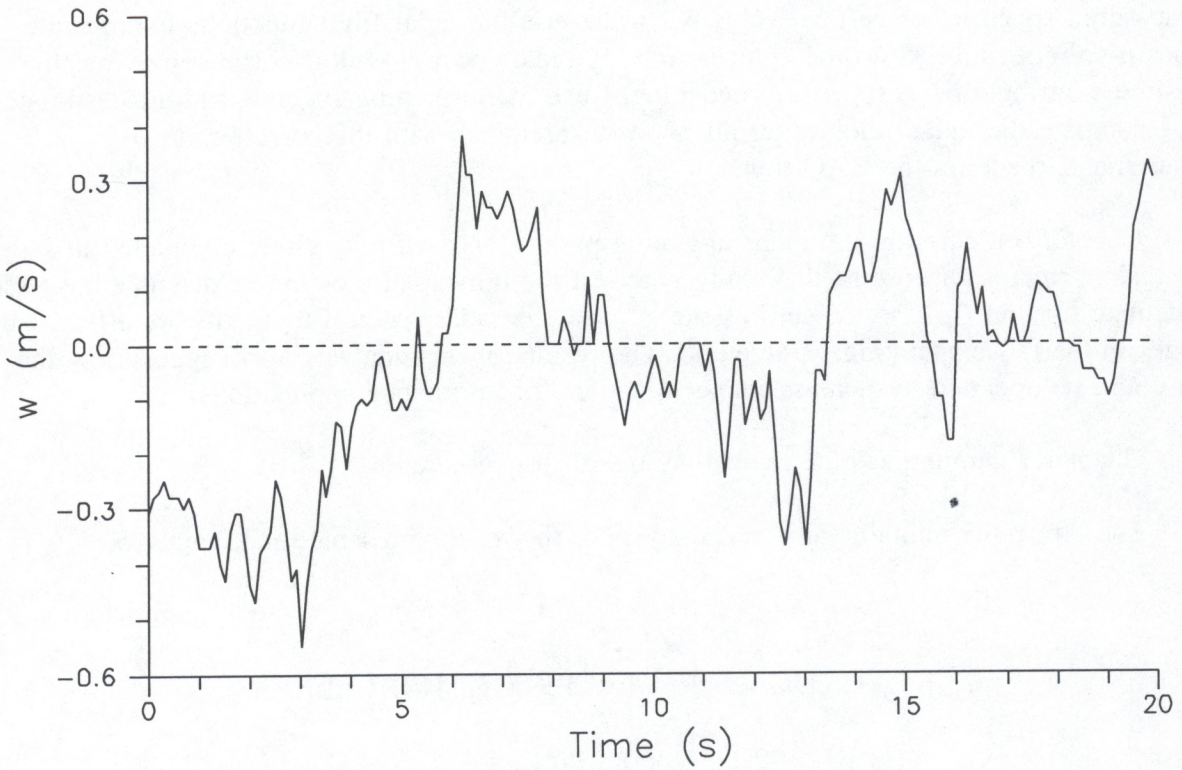

Figure 2.1. A time series of fluctuating vertical velocity in the CBL sampled at a rate of 10 Hz with a sonic anemometer on 15 July 1995 beginning at 16:47:05 GMT. The anemometer was mounted on a 3-m boom which was attached to the 250-m level of the BAO tower located in Erie, Colorado.

substitution depends on whether the random process considered is ergodic. But as Panofsky and Dutton (1984) show, it is not possible to ensure ergodicity from the limited number of realizations that correspond to a particular set of turbulence measurements. Furthermore, strict ergodicity requires the process to be stationary, which, in the atmosphere, requires us to use short averaging times. For example, Kaimal and Finnigan (1994), among others, suggest that to avoid the nonstationarity associated with diurnal changes in the atmosphere, averaging times should not exceed one hour. But the use of a finite time average results in sampling uncertainty, which would occur even if strict ergodicity existed. Thus, the issue of ergodicity becomes less critical than the issue of stationarity.

Another important characteristic of a random process is its autocorrelation function $R(t_1, t_2)$,

$$R(t_1, t_2) = \overline{f(t_1) f(t_2)}. \tag{2.2}$$

The autocorrelation function characterizes the mutual relation between the fluctuations $f(t)$ at different instants of time. If the fluctuations at the times t_1 and t_2 are not related to each other, i.e., if they are statistically independent, then $R(t_1, t_2)$ vanishes. Note that when $t_1 = t_2$, the autocorrelation function is equivalent to the variance, $\sigma^2 = \overline{[f(t)]^2}$. Furthermore, the Schwarz inequality can be used (e.g., Panofsky and Dutton, 1984) to show that

$$-1 \leq \frac{R(t_1, t_2)}{\sigma(t_1)\sigma(t_2)} \leq 1. \tag{2.3}$$

The ratio in (2.3) is called the autocorrelation coefficient, or the normalized autocorrelation function, and is denoted here by $r(t_1, t_2)$.

2.1.1 Stationarity

The mean value of a random process can be constant or can change with time. Similarly, the autocorrelation function $R(t_1, t_2)$ can depend either on the time displacement only or it can depend also on the positions of t_1 and t_2 on the time axis. A random process is stationary if its mean value does not change with time and if its correlation function depends only on the magnitude of the time displacement, i.e.,

$$\overline{F(t)} = \text{const}, \quad R(t_1, t_2) = R(|t_1 - t_2|) = R(\tau). \tag{2.4}$$

Similarly, under stationarity $r(t_1, t_2) = r(\tau)$. Usually the integral and first two derivatives of

$r(\tau)$ are presumed to exist and are used to define two time scales (Lumley and Panofsky, 1964):

$$\int_0^\infty r(\tau)d\tau = \Im, \quad \left.\frac{d^2 r(\tau)}{dt^2}\right|_{\tau=0} = -\frac{2}{\Lambda^2}, \tag{2.5}$$

where $\Im$ and Λ are the integral scale and microscale, respectively. However, trends in meteorological data often prevent $r(\tau)$ from tending toward zero at large τ, so that $\Im$ is difficult to determine.

Another feature of a stationary random process is that its correlation function forms a Fourier transform pair with the power-spectral density (hereafter "spectrum"), $\phi(\omega)$[1]:

$$R(\tau) = \frac{1}{2}\int_{-\infty}^{\infty} e^{-i\omega\tau}\phi(\omega)\,d\omega, \tag{2.6}$$

$$\phi(\omega) = \frac{1}{\pi}\int_{-\infty}^{\infty} e^{i\omega\tau}R(\tau)\,d\tau. \tag{2.7}$$

Here, ω is the circular frequency and $\omega = 2\pi/T = 2\pi f$, where T is the period of a sinusoidal oscillation and f is the frequency in cycles/time or hertz. The integrals in (2.6) and (2.7) are examples of Fourier-Stieltjes integrals. The spectrum $\phi(\omega)$ shows how the energy of the fluctuations $f(t)$ is distributed with respect to ω. This representation relies on the assumption that the correlation function is continuous and integrable, assumptions that are sufficiently unrestrictive to be permissible in nearly any physical situation (Lumley and Panofsky, 1964).

Because of stationarity, $R(\tau) = R(-\tau)$. Thus, (2.7) can be rewritten as

$$\begin{aligned}\phi(\omega) &= \frac{1}{\pi}\int_{-\infty}^{\infty}\cos(\omega\tau)R(\tau)d\tau \\ &= \frac{2}{\pi}\int_0^{\infty}\cos(\omega\tau)R(\tau)d\tau,\end{aligned} \tag{2.8}$$

which implies $\phi(\omega) = \phi(-\omega)$ and allows (2.6) to be rewritten as

---

[1]I have chosen to use the spectral representation convention of Panofsky and Dutton (1984) because written in this way, the spectrum integrated over the positive frequency range gives the variance directly (i.e., without involving a factor of 2).

$$R(\tau) = \int_0^\infty \cos(\omega\tau)\phi(\omega)\,d\omega. \tag{2.9}$$

Earlier, we saw that the correlation function evaluated at zero lag, $R(0)$, is equivalent to the variance. Evaluation of (2.9) with $\tau = 0$ shows that the variance is also found by integrating the spectrum

$$\sigma^2 = R(0) = \int_0^\infty \phi(\omega)\,d\omega. \tag{2.10}$$

2.1.2 Stationary increments

Many physical processes can be described using stationary random functions. One example is the fluctuating voltage appearing across a resistance in a state of thermodynamic equilibrium with the surrounding medium. However, in meteorology, often this is not the case. For example, the diurnal heating cycle causes the air temperature to undergo slow and smooth changes. And even on shorter time scales, as the strength of the wind increases, the mean value of the velocity at any point also increases. In these and many other geophysical cases, it is difficult to determine whether changes in the variable should be regarded as changes in the mean or as slow fluctuations.

One way to relax the constant mean constraint is to use the structure function, first introduced by Kolmogorov (1941), instead of the correlation function discussed above. When the mean value $\overline{f(t)}$ changes with time, the basic idea behind this method is to consider the difference $F_\tau(t) = F(t+\tau) - F(t)$ instead of $F(t)$. For values of τ which are not too large, slow changes in $F(t)$ do not affect the value of $F_\tau(t)$, and, thus, $F_\tau(t)$ can be considered a stationary random function, at least approximately. In this case, $F(t)$ is called a random function with stationary first increments, or simply a random function with stationary increments (Tatarski, 1961).

The structure function, $D(\tau)$, where

$$D(\tau) = \overline{[f(t+\tau) - f(t)]^2}, \tag{2.11}$$

characterizes a random process with stationary increments. The value of $D(\tau)$ is related to the intensity of the fluctuations $f(t)$ that are smaller than or comparable to τ. Structure functions can also be constructed for ordinary stationary functions, which are a special case of functions with stationary increments. Expanding (2.11), we have

$$D(\tau) = \overline{[f(t+\tau) - f(t)]^2} = \overline{[f(t+\tau)]^2} + \overline{[f(t)]^2} - \overline{2f(t+\tau)f(t)}. \quad (2.12)$$

And because $F(t)$ is stationary, it follows that

$$\overline{[f(t)]^2} = \overline{[f(t+\tau)]^2} = R(0). \quad (2.13)$$

Thus, for a stationary process,

$$D(\tau) = 2[R(0) - R(\tau)]. \quad (2.14)$$

Using (2.9) and (2.10), we obtain

$$D(\tau) = 2\int_0^\infty [1 - \cos(\omega\tau)]\phi(\omega)d\omega. \quad (2.15)$$

Tatarski (1961) showed that the same expansion is valid for the structure function of the general random function with stationary increments. The only difference is that $\phi(\omega)$ can have a singularity at the origin, in which case the physical interpretation of the spectrum cannot be the same as it was for the transform of the correlation function, since the energy of the fluctuations must be finite.

2.2 Random Fields

I now consider random functions of three spatial coordinates, or random fields. Examples of random fields in the atmosphere are the turbulent vector wind-velocity field and the turbulent scalar fields of temperature, humidity, and dielectric constant. Since the index of refraction of the atmosphere for electromagnetic waves is a function locally of the temperature and humidity, it too is a scalar random field. In this work, I analyze and compare the turbulent refractive index and velocity structure determined both in the context of a random process and a random field. The volume illuminated by the radar's transmitted pulse constitutes a random field, while the time series of point measurements made on the tower corresponds to a random process.

The concept of a random field, $\mathbf{F}(\mathbf{r})$, is completely analogous to the concept of a random process $F(t)$ discussed in Section 2.1.[2] For example, we can define the mean value

[2]Here, for simplicity, I consider the spatial fluctuations that occur at one point in time, and thus no explicit time dependence is given. Also, I have used a vector function, so that I may include the random velocity field in this discussion.

$\overline{\mathbf{F}(\mathbf{r})}$ as well as the correlation function

$$R_{ij}(\mathbf{r}_1,\mathbf{r}_2) = \overline{f_i(\mathbf{r}_1)f_j(\mathbf{r}_2)}, \tag{2.16}$$

where $i,j = 1,2,3$ correspond to the components of the fluctuations f_i in $\mathbf{F}$, R_{ij} is the correlation tensor, and the overbar denotes a space (volume) average.

2.2.1 Homogeneity

In the case of random fields, the concept of stationarity generalizes to the concept of homogeneity. A random field is homogeneous if its mean value is constant and if its correlation function does not change when the points $\mathbf{r}_1$ and $\mathbf{r}_2$ are both displaced by the same amount in the same direction, i.e., if

$$\overline{\mathbf{F}(\mathbf{r})} = \text{const}, \quad R_{ij}(\mathbf{r}_1,\mathbf{r}_2) = R_{ij}(\mathbf{r}_1+\mathbf{r}_o, \mathbf{r}_2+\mathbf{r}_o). \tag{2.17}$$

Choosing $\mathbf{r}_o = -\mathbf{r}_2$ shows that the correlation function of a homogeneous random field depends only on the vector difference, $\boldsymbol{\xi} = (\mathbf{r}_1 - \mathbf{r}_2)$.

Just as with a stationary random function, the correlation function for a homogeneous random field forms a Fourier transform pair with the spectrum

$$R_{ij}(\boldsymbol{\xi}) = \frac{1}{2^3}\int_{-\infty}^{\infty}\int\int e^{-i\mathbf{k}\cdot\boldsymbol{\xi}}\Phi_{ij}(\mathbf{k})d\mathbf{k} \tag{2.18}$$

$$\Phi_{ij}(\mathbf{k}) = \frac{1}{\pi^3}\int_{-\infty}^{\infty}\int\int e^{i\mathbf{k}\cdot\boldsymbol{\xi}}R_{ij}(\boldsymbol{\xi})d\boldsymbol{\xi}, \tag{2.19}$$

where $\Phi_{ij}(\mathbf{k})$ is the three-dimensional spectral density tensor, $\mathbf{k} = 2\pi/\mathbf{L}$ is the angular wavenumber vector, and $\mathbf{L}$ is the wavelength vector. Because of the symmetry of R_{ii}, Φ_{ii} is purely real, and symmetric: $\Phi_{ii}(\mathbf{k}) = \Phi_{ii}(-\mathbf{k})$. Φ_{ii} represents, for example, the spectrum of a scalar in three dimensions. However, for vectors, the off-diagonal terms ($i \neq j$) of R_{ij} and Φ_{ij} are not so well behaved; R_{12}, for example, can be even or odd, and Φ_{12} can be real or imaginary (Lumley and Panofsky, 1964).

The data-acquisition and processing program used to generate the spectral data presented in Chapter 5 rotates the coordinate system so that the x_1-axis is oriented along the direction of the mean wind. Consequently, the program produces the one-dimensional

spectrum, $\phi_{ij}(k_1)$, which is related to the three-dimensional spectrum $\Phi_{ij}(\mathbf{k})$ by

$$\phi_{ij}(k_1) = \frac{1}{2^2} \int\int_{-\infty}^{\infty} \Phi_{ij}(\mathbf{k})\, dk_2\, dk_3 . \tag{2.20}$$

It is also possible and often convenient to have an expression for the three-dimensional spectrum that is a function of a single scale. By integrating $\Phi_{ij}(\mathbf{k})$ over a spherical shell of radius $k = |\mathbf{k}|$, we have

$$\psi_{ij}(k) = \oiint_{A(k)} \Phi_{ij}(\mathbf{k})\, dA(k) . \tag{2.21}$$

Switching to spherical coordinates gives us

$$\psi_{ij}(k) = k^2 \int_0^{2\pi} \int_{-\pi/2}^{\pi/2} \Phi_{ij}(\lambda, \varphi, k) \cos(\varphi)\, d\varphi\, d\lambda . \tag{2.22}$$

The function $\psi_{ij}(k)$ is sometimes referred to as the spherical average spectrum. Panofsky and Dutton (1984) go on to define an additional spectrum, $E(k)$, where

$$E(k) = \frac{1}{16} \psi_{ii}(k). \tag{2.23}$$

The spectrum $E(k)$ is related to the variance tensor, σ_{ii}^2, by

$$\begin{aligned} \frac{\sigma_{ii}^2}{2} = \frac{1}{2} R_{ii}(0) &= \frac{1}{2^4} \int\int\int_{-\infty}^{\infty} \Phi_{ii}(\mathbf{k})\, d\mathbf{k} \\ &= \frac{1}{2^4} \int_0^{\infty} dk \oiint \Phi_{ii}(\mathbf{k})\, dA(k) = \int_0^{\infty} E(k)\, dk . \end{aligned} \tag{2.24}$$

Since, in the case of velocity, $E(k)$ integrates to give the kinetic energy, it is called the energy spectrum.

2.2.2 Isotropy

A homogeneous random field is isotropic if its statistics are unaffected by rotation or reflection of the coordinate system. As with the consequences of homogeneity, the consequences of isotropy are different for scalars and vectors. For isotropic scalars, $\Phi_{ii}(\mathbf{k})$ must be only a function of $k = |\mathbf{k}|$. Similarly, $R_{ii}(\boldsymbol{\xi})$ can depend only on $\xi = |\boldsymbol{\xi}|$. Using (2.22) and (2.23), we find that

$$E(k) = \frac{1}{16}\psi_{ii}(k) = \frac{\pi k^2}{4}\Phi_{ii}(k). \tag{2.25}$$

Furthermore, when we solve (2.25) for Φ_{ii} and substitute the resulting expression in (2.20), the integration leads to (using k for k_1)

$$E(k) = -\frac{k}{2}\frac{d\phi_{ii}(k)}{dk}. \tag{2.26}$$

With vectors, the consequences of isotropy are somewhat more complex. Based on the assumption of isotropy, however, it can be shown (Batchelor, 1956) that the second rank tensor of a vector must be of the form

$$\Phi_{ij}(\mathbf{k}) = A(k)k_i k_j + B(k)\delta_{ij}, \tag{2.27}$$

where $\delta_{ij} = 1$ if $i = j$ and zero otherwise. To determine the unknown functions A and B, we assume incompressibility, the condition of which is given here by $u_{i,i} = 0$ (the comma denotes partial differentiation with respect to the direction given by the index that follows). This implies $R_{ij,j}(\mathbf{r}) = 0$, and in turn $k_i\Phi_{ij}(\mathbf{k}) = 0$ (Lumley and Panofsky, 1964). Then (2.27) gives

$$B(k) = -k^2 A(k) \tag{2.28}$$

or

$$\Phi_{ij}(\mathbf{k}) = A(k)[k_i k_j - k^2\delta_{ij}]. \tag{2.29}$$

Contracting the tensor by summing i on j and noting that $\delta_{ii} = 3$, we have

$$\Phi_{ii}(k) = -2k^2 A(k). \tag{2.30}$$

Combining (2.25) and (2.30) gives

$$A(k) = -\frac{2E(k)}{\pi k^4}, \tag{2.31}$$

and thus,

$$\Phi_{ij}(\mathbf{k}) = 2\frac{E(k)}{\pi k^4}(k^2\delta_{ij} - k_i k_j). \tag{2.32}$$

Now all that remains is to relate the one-dimensional spectra (the type measured in this work) to the corresponding three-dimensional spectrum. For example, by substituting the expression for $\Phi_{11}(\mathbf{k})$ given by (2.32) into (2.20) and integrating, Panofsky and Dutton (1984) showed that (again using k for k_1)

$$E(k) = \frac{k^3}{2}\left[\frac{d}{dk}\left(\frac{1}{k}\frac{d\phi_{11}(k)}{dk}\right)\right], \tag{2.33}$$

where $\phi_{11}(k_1)$ characterizes the wind fluctuations that occur in the same direction as the line separating the two measurement points and is called the longitudinal spectrum. The spectrum $\phi_{22}(k_1)$ characterizes the wind fluctuations occurring in a direction orthogonal to the line separating the two measurement points and is called the transverse or lateral spectrum. The two spectra are related under isotropy by

$$\phi_{22}(k) = \frac{1}{2}\left[\phi_{11}(k) - k\frac{d\phi_{11}(k)}{dk}\right]. \tag{2.34}$$

We can also use the one-dimensional spectra to calculate the longitudinal and transverse correlation functions, given by R_{11} and R_{22}, respectively:

$$R_{11}(\xi) = \frac{1}{2}\int_{-\infty}^{\infty} e^{-ik\xi}\phi_{11}(k)\,dk \tag{2.35}$$

$$R_{22}(\xi) = \frac{1}{2}\int_{-\infty}^{\infty} e^{-ik\xi}\phi_{22}(k)\,dk. \tag{2.36}$$

Thus, under the assumption of isotropy, the spectrum $\Phi_{ij}(\mathbf{k})$ is reduced to only two independent spectra for vectors and one spectrum for scalars.

2.2.3 Local homogeneity and isotropy

Unfortunately, meteorological fields are not homogeneous and isotropic at all scales. The large-scale components that are always present in atmospheric turbulence often destroy the homogeneity and isotropy of the fields. In addition, because atmospheric turbulence depends highly on the stratification of the atmosphere, which occurs almost always in the vertical direction, some anisotropy is inherent. By examining the consequences of isotropy for the velocity field, we find further indications of anisotropy. Under isotropy, only the diagonal terms of the stress tensor $\overline{u_i u_j}$ can be non-zero since the off-diagonal terms change under a rotation of the coordinate system. We know, however, that the horizontal- and vertical-velocity components are correlated in the surface layer, so isotropy is violated. Furthermore, since the diagonal terms change into each other when the coordinate system is rotated by 90°, then $\overline{u_1^2} = \overline{u_2^2} = \overline{u_3^2}$. However, measurements show that the variances of the velocity components in the atmospheric boundary layer are not necessarily equal.

Therefore, in analyzing the spatial structure of random fields, it is again appropriate to use structure functions (Tatarski, 1961). The idea is based on the observation that the difference between the fluctuating quantities of a random field at two different locations, $[f(\mathbf{r}_1) - f(\mathbf{r}_2)]$, is mainly affected by only those scales of the field with dimensions that do not exceed the distance between $\mathbf{r}_1$ and $\mathbf{r}_2$. If this distance is not too large, then $[f(\mathbf{r}_1) - f(\mathbf{r}_2)]$ will not be influenced by the largest scales, which are inhomogeneous and anisotropic. Therefore, the structure function

$$D(\mathbf{r}_1, \mathbf{r}_2) = \overline{[f(\mathbf{r}_1) - f(\mathbf{r}_2)]^2} \tag{2.37}$$

depends approximately on $\mathbf{r}_1 - \mathbf{r}_2$ only. At the same time, the value of the correlation function $R(\mathbf{r}_1, \mathbf{r}_2)$ depends on inhomogeneities of all scales, and not just those of size characterized by $\mathbf{r}_1 - \mathbf{r}_2$. A random field is locally homogeneous in the region G if the probability distribution functions of the random variable $[f(\mathbf{r}_1) - f(\mathbf{r}_2)]$ do not change when the pair of points $\mathbf{r}_1$ and $\mathbf{r}_2$ are shifted to new locations within the region G (Kolmogorov, 1941; Tatarski, 1961). Therefore, $D(\mathbf{r}_1, \mathbf{r}_2) = D(\mathbf{r}_1 - \mathbf{r}_2)$.

We can make a further simplification if the structure function is also locally isotropic. A locally homogeneous random field is also locally isotropic in the region G if the probability distribution functions of the quantity $[f(\mathbf{r}_1) - f(\mathbf{r}_2)]$ are invariant with respect to rotations and mirror reflections of the vector $\mathbf{r}_1 - \mathbf{r}_2$ within the region G (Kolmogorov, 1941; Tatarski, 1961). The structure function, then, depends only on $\xi = |\mathbf{r}_1 - \mathbf{r}_2|$. Therefore, $D(\mathbf{r}_1 - \mathbf{r}_2) = D(\xi)$.

When we apply the concept of structure functions to the velocity field (i.e., a vector random field), we arrive at a set of nine structure functions (instead of one) involving the components of the vector $\mathbf{u}$:

$$D_{ij}(\boldsymbol{\xi}) = \overline{[u_i(\mathbf{r}+\boldsymbol{\xi}) - u_i(\mathbf{r})]\,[u_j(\mathbf{r}+\boldsymbol{\xi}) - u_j(\mathbf{r})]}. \tag{2.38}$$

However, as was the case with the correlation functions and spectra of isotropic vector random fields, the nine structure functions of locally isotropic random fields are reduced to only two independent structure functions (Kolmogorov, 1941; Batchelor, 1956):

$$D_{ij}(\boldsymbol{\xi}) = [D_{11}(\xi) - D_{22}(\xi)]n_i n_j + D_{22}(\xi)\delta_{ij}, \tag{2.39}$$

where n_i are the components of the unit vector directed along $\boldsymbol{\xi}$,

$$D_{11}(\xi_1) = \overline{[u_1(x_1+\xi_1, x_2, x_3) - u_1(x_1, x_2, x_3)]^2} \tag{2.40}$$

is the longitudinal velocity structure function, and

$$D_{22}(\xi_1) = \overline{[u_2(x_1+\xi_1, x_2, x_3) - u_2(x_1, x_2, x_3)]^2} \tag{2.41}$$

is the transverse velocity structure function. When the velocity field is incompressible, the two are related by

$$D_{22}(\xi) = \frac{1}{2\xi}\frac{d}{d\xi}(\xi^2 D_{11}), \tag{2.42}$$

so that D_{ij} is determined by a single function.

2.3 Application of the Statistical Theory to Measurements

2.3.1 Spectral coordinates

Because the energy of atmospheric turbulence is spread out over a wide range of frequencies, it is customary to use frequency $f = \omega/2\pi$ in cycles/time or Hertz instead of ω when plotting spectra. I use $S(f)$ to denote the spectral density function of a measured one-dimensional spectrum. It is also customary to multiply $S(f)$ by f in order to give weight to the higher frequencies and to plot the spectrum against $\ln f$ instead of f. The latter change has the advantage of collapsing the frequency scale while preserving the area under the spectrum:

$$\int_0^\infty fS(f)\,d\ln f = \int_0^\infty S(f)\,df = \int_0^\infty \phi(\omega)\,d\omega = \sigma^2. \tag{2.43}$$

Later, in Chapter 5, I use a logarithmic scale for $fS(f)$ as well, since this has the advantage of showing constant powers of f as straight lines, although the area-variance equivalence is sacrificed.

2.3.2 Taylor's hypothesis

The notion that turbulent eddies are advected by the mean wind and change only slowly as they are carried along is called the frozen wave hypothesis, or Taylor's hypothesis (Taylor, 1938). In a coordinate system where the mean wind, $\overline{u}$, is oriented along the x_1-axis, Taylor's hypothesis approximates that the autocorrelation functions in space, R_s, and time, R_t, be related by

$$R_s(\xi) = R_t(\tau) \quad \xi = \overline{u}\tau \tag{2.44}$$

and the corresponding spectra by

$$kS_s(k) = fS_t(f) \quad k = \frac{2\pi f}{\overline{u}}, \tag{2.45}$$

where k is the wavenumber in the mean wind direction. This hypothesis is of paramount importance to the experimentalist, since it allows him/her to infer the spatial structure of isotropic or locally isotropic turbulence from time series measurements taken at one point. For example, when Taylor's hypothesis is valid, we can use (2.45) to transform the temporal spectrum of u into the longitudinal one-dimensional spectrum $\phi_{11}(k_1)$. Similarly, the temporal spectra of v or w transform into the transverse one-dimensional spectrum $\phi_{22}(k_1)$.

In order for Taylor's hypothesis to be valid, the turbulence must be stationary and homogeneous in the direction of the mean wind. Ideally, to test Taylor's hypothesis one would then deploy a line of sensors along the mean wind direction. Panofsky (1962) used this approach and confirmed that Taylor's hypothesis was well satisfied at a height of 2 m above a homogeneous surface in Nebraska. For measurements at 250 m AGL, this method is not practical. However, it can be argued to first approximation that in order for an eddy to change negligibly as it advects past a sensor, Taylor's hypothesis requires a low turbulence level. For example, using σ_u as a measure of the intensity of turbulence, Willis and Deardorff (1976) suggest that Taylor's hypothesis is reasonable when

$$\frac{\sigma_u}{\overline{u}} < 0.5. \tag{2.46}$$

For the measurements discussed in Section 5.2.3, $\sigma_u \approx 1$ m s^{-1} and $\overline{u} = 4.1$ m s^{-1}, which gives a ratio of 0.24. Likewise, for the measurements discussed in Section 5.3.3, $\sigma_u \approx 1$ m s^{-1} and $\overline{u} = 4.5$ m s^{-1}, which gives a ratio of 0.22. Based on this simple argument, Taylor's hypothesis should be valid for these measurements. Still, there are indications that the BAO

site does not strictly adhere to the conditions necessary for Taylor's hypothesis to be valid. First, the surrounding terrain in all directions is inhomogeneous. Second, the nearby Rocky Mountains cause disturbances in the flow, such as standing waves, which also give rise to nonstationary conditions. Thus, I must conclude that Taylor's hypothesis is only approximately valid for the measurements obtained at the BAO.

It is also important to consider what is the appropriate average velocity to use in applying Taylor's hypothesis. For example, Panofsky and Dutton (1984) point out that high-frequency structures advect with the mean wind, while lower-frequency structures move with a convective velocity that is somewhat larger than the local wind. However, in geophysical flows we typically use short time samples to calculate high-frequency turbulence spectra. As reported by Hill (1996), the relevant average velocity to use in applying Taylor's hypothesis to these cases is the average calculated over the "short" measurement time. Here, Hill (1996) uses "short" to mean a duration short compared to the time required for the velocity-component joint probability density function to obtain its long-time-averaged form. Therefore, in applying Taylor's hypothesis to the frequency spectra measured on the tower (see Section 5.1.3), I used the mean wind speed measured over the 15-min sampling period.

2.3.3 Properties of the inertial subrange

Kolmogorov (1941) proposed that the spectra of turbulence could be divided into three regions: the energy-containing subrange, the inertial subrange, and the dissipation subrange. Under this hypothesis, there is no direct energy transfer between the energy-containing subrange and the dissipation subrange. However, the rate of energy transfer from the large scales in the energy-containing subrange is equivalent to the rate of energy dissipation at the small scales in the dissipation subrange. In geophysical turbulence (i.e., large Reynolds number turbulence), the large and small scales become statistically independent. The small scales attain a universal structure which is also isotropic.

Over the mid-scales in the inertial subrange, the bulk of the energy transfer is from the larger scales to the smaller scales. In the case of velocity, energy is transferred at the rate ε. For scalars, this rate is χ. The one-dimensional spectra of velocity in the inertial subrange depend only on k_1 and ε. This argument was originally presented by Kolmogorov (1941) for the energy spectrum. Likewise, the spectra of scalars depend only on k_1, χ, and ε. The velocity scale imbedded in ε is important to the rate of destruction of scalar variance because scalar fluctuations are produced by the air motions associated with velocity turbulence.

By dimensional analysis, the spectral densities of velocity components in the inertial subrange are given by

$$S_\alpha(k_1) = A\varepsilon^{2/3}k_1^{-5/3}, \tag{2.47}$$

where the subscript α could be u, v, or w, and A is an empirical constant. Lumley and

Panofsky (1964) list a number of the earlier studies that confirm the -5/3 power law expressed in (2.47). Some of these studies found that for one-dimensional spectra, a -5/3 dependence extended to spatial scales that were large compared to the distance from the ground and, thus, would be expected to lie outside of the inertial subrange. Note that (2.47) follows from the "energy cascade" assumption, not from isotropy.

Upon inserting the $k^{-5/3}$ dependence in (2.34), we obtain

$$S_v(k_1) = S_w(k_1) = \frac{4}{3} S_u(k_1). \tag{2.48}$$

Thus, in order for (2.47) to apply to all velocity spectra, the constant A must be different by a factor of 4/3 for the longitudinal and lateral cases. Fairall and Larsen (1986) suggest using $A = 0.52$ for S_u, which gives $A = 0.69$ for S_v and S_w. For scalars, dimensional analysis gives

$$S_\theta(k_1) = B\varepsilon^{-1/3}\chi_\theta k_1^{-5/3}, \tag{2.49}$$

where the subscript θ denotes a scalar variable. The value of B is taken to be 0.4 (Fairall and Larsen, 1986).

Using the same reasoning, we can derive a similar law for structure functions in the inertial subrange. We begin with the Fourier transform of the structure function given by (2.15), except now in terms of a one-dimensional wavenumber spectrum instead of a frequency spectrum:

$$D_x(\xi_1) = 2\int_0^\infty [1 - \cos(k_1\xi_1)]\phi_x(k_1)\,dk_1, \tag{2.50}$$

where the subscript x could be θ or α, i.e., a scalar or velocity component. Using ξ for ξ_1, k for k_1, and differentiating with respect to ξ, we obtain

$$\frac{\partial D_x}{\partial \xi} = 2k\int_0^\infty \sin(k\xi)\phi_x(k)\,dk. \tag{2.51}$$

Then, taking the inverse transform we find that

$$\phi_x(k) = \frac{1}{\pi k}\int_0^\infty \frac{\partial D_x(\xi)}{\partial \xi}\sin(k\xi)\,d\xi. \tag{2.52}$$

Now suppose that the form for structure functions in the inertial subrange is given by

$$D_x = C_x^2 \xi^m. \tag{2.53}$$

This dependence on separation follows from the classical similarity theory of Kolmogorov that was applied earlier to the spectra. Differentiating with respect to ξ gives

$$\frac{\partial D_x}{\partial \xi} = C_x^2 m \xi^{m-1}, \tag{2.54}$$

so that ϕ_x is given by

$$\phi_x(k) = \frac{C_x^2 m}{\pi k} \int_0^\infty \xi^{m-1} \sin(k\xi)\, d\xi, \tag{2.55}$$

which can also be written in the form

$$S_x(k) = \frac{C_x^2}{\pi} \Gamma(m+1) \sin\left(\frac{m\pi}{2}\right) k^{-(m+1)}. \tag{2.56}$$

However, because (2.47) and (2.49) have $S_x \sim k^{-5/3}$, (2.56) requires that $m = 2/3$. The constant of proportionality C_x^2 is called the structure function parameter and is given by

$$C_x^2 = \frac{D_x}{\xi^{2/3}}. \tag{2.57}$$

Evaluation of (2.56) with $m = 2/3$ gives

$$S_x(k) = 0.25\, C_x^2 k^{-5/3}. \tag{2.58}$$

Using the expressions for S_x given by (2.47) and (2.49), we arrive at

$$C_\alpha^2 = 4A\varepsilon^{2/3}. \tag{2.59}$$

and

$$C_\theta^2 = 4B\varepsilon^{-1/3}\chi_\theta \tag{2.60}$$

These expressions result from the inertial-range turbulence theory of Corrsin (1951), and thus they are commonly referred to as Corrsin relations.

To summarize, in this chapter I reviewed some of the basic statistical properties of turbulence. The discussion led to theoretical expressions for spectra and structure functions of isotropic turbulence in the inertial subrange which allow me to infer the turbulent kinetic energy (TKE) and scalar dissipation rates without making direct measurements of these quantities. In Chapter 5 I apply this theory to scalar and velocity microturbulence measurements.

3. BEHAVIOR OF STRUCTURE FUNCTION PARAMETER PROFILES AND DISSIPATION RATE PROFILES IN THE CONVECTIVE BOUNDARY LAYER

Our knowledge of atmospheric boundary-layer structure has developed from a combination of laboratory simulations, numerical models and simulations, and atmospheric measurements. Of the many different types of boundary layers that have been studied with these techniques, the cloud-free, convective boundary layer (CBL) is the best understood in terms of the development of simplified conceptual models and useful scaling laws or parameterizations (Fairall, 1987a), although Wyngaard (1992) reports that progress has been made with regard to the stable boundary layer (e.g., Nieuwstadt, 1984).

The CBL is usually defined in terms of three height regions: the surface layer, the mixed layer, and the interfacial layer. Of these, the surface layer has received the most attention and is the best understood, primarily because of its accessibility to measurement. The Monin-Obukhov (M-O) similarity hypothesis has brought order to surface-layer observations (Wyngaard, 1992). But even our understanding of the surface layer can be considered tenuous, for example, in the presence of nonhomogeneous surface conditions. And while evidence supports a mixed-layer scaling, there are questions as to its applicability for boundary layers over complex terrain (Kustas and Brutsaert, 1987). Furthermore, the effects of entrainment on turbulence statistics in the boundary layer are not fully understood.

The profiles of structure function parameters have been studied rigorously since the 1960s, primarily because of an interest in the effects of turbulence on the propagation of acoustic and electromagnetic waves. A number of studies (e.g., Neff, 1975; Thomson et al., 1978; and Coulter and Wesley, 1980) have demonstrated the use of sodar to measure profiles of C_T^2 and C_v^2. Similarly, Gossard et al. (1990) and White et al. (1991), among others, have used properly calibrated radars to measure profiles of C_n^2 and C_Q^2. Success of a more qualitative nature has been achieved with radar measurements of C_u^2 (or alternatively, ε) (e.g., Hocking, 1985; Gossard et al., 1990; and Cohn, 1995). Part of the problem with validating these techniques has been the lack of direct observations available for comparison.

This chapter summarizes the current understanding of how structure function parameter and dissipation rate profiles behave in the CBL. In Section 3.1, I discuss scalar structure function parameters. Discussion pertaining to the velocity structure function parameter, which is related to ε through inertial range turbulence theory, is presented in Section 3.2.

3.1 Scalar Structure Function Parameter Profiles

As shown in Chapter 5 [see (5.6) - (5.8)], the refractive-index structure function parameter, C_n^2, receives contributions from temperature (C_T^2), humidity (C_Q^2), and temperature-humidity correlation (C_{TQ}). For remote sensors, the relative magnitudes of these contributions depend on pressure, temperature, humidity, and the operating wavelength of the instrument (see Wesley, 1976). Fairall (1991) looked at this dependence for clear-air radars, such as the one used in this study, and found that given the wide range of surface Bowen ratios observed over land, it is necessary to evaluate the relative contributions of C_T^2, C_{TQ}, and C_Q^2 to C_n^2 in the convective boundary layer on a case-by-case basis. In the marine boundary layer, C_n^2 is typically dominated by C_Q^2.

3.1.1 Surface layer

Wyngaard et al. (1971a) showed that the profiles of structure function parameters in the surface layer are well described by M-O similarity theory. The principal idea behind M-O similarity is that the statistical structure of turbulence in the surface layer is determined by four governing parameters: the height above the surface, z; the friction velocity,

$$u_* = [(\overline{uw})_s^2 + (\overline{vw})_s^2]^{1/4}, \tag{3.1}$$

where the "s" denotes a surface value; the buoyancy parameter, g/T, where g is the acceleration due to gravity; and the surface temperature flux, $(\overline{\theta w})_s$. These four parameters by themselves or in combination define two length scales, z and

$$L = \frac{-u_*^3 T}{k_a g (\overline{\theta_v w})_s}, \tag{3.2}$$

where k_a is the von Kármán constant, traditionally taken to be 0.4, and $(\overline{\theta_v w})_s = (\overline{\theta w})_s + 0.61 T (\overline{qw})_s / \rho$ is the surface virtual temperature flux, where ρ is the density of air and q the specific humidity. In addition, the governing parameters define a velocity scale, u_*; a temperature scale,

$$T_* = \frac{(\overline{\theta w})_s}{u_*}; \tag{3.3}$$

and a humidity scale,

$$Q_* = \frac{(\overline{qw})_s}{u_*}. \tag{3.4}$$

With M-O similarity, the variables that describe the surface-layer turbulence structure, when made dimensionless by these scales, are hypothesized to be universal functions of z/L. For example, when applied to structure function parameters, the scaling hypothesis leads to (Wyngaard et al., 1971a)

$$\frac{C_T^2 z^{2/3}}{T_*^2} = f_1(z/L), \tag{3.5}$$

$$\frac{C_{TQ} z^{2/3}}{T_* Q_*} = f_2(z/L), \tag{3.6}$$

$$\frac{C_Q^2 z^{2/3}}{Q_*^2} = f_3(z/L), \tag{3.7}$$

where the functions f_1, f_2, and f_3 must be determined experimentally. Wyngaard et al. (1971a) measured f_1 over a range of stable and unstable conditions using data from the 1968 Kansas experiment. Subsequent studies by Davidson et al. (1978), Fairall et al. (1980), Kohsiek (1982), and Smith et al. (1983), among others, have supported the M-O prediction.

At the outer edge of the surface layer, Wyngaard et al. (1971b) argued that under unstable conditions, the surface-layer expressions approach a "local free convection" height dependence. Here, z continues to be the significant length scale, but u_* is no longer the appropriate velocity scale and should therefore drop out of (3.5) - (3.7). In order for this to occur, f_1, f_2, and f_3 must be proportional to u_*^2, and thus to $(-z/L)^{-2/3}$. Therefore, in the local free convection limit, the structure functions are predicted to obey a $z^{-4/3}$ height dependence:

$$C_T^2 \sim \overline{\theta w}_s^{\,2} \left(\frac{g}{T} \overline{\theta_v w}_s \right)^{-2/3} z^{-4/3}, \tag{3.8}$$

$$C_{TQ} \sim \overline{\theta w}_s \, \overline{qw}_s \left(\frac{g}{T} \overline{\theta_v w}_s \right)^{-2/3} z^{-4/3}, \tag{3.9}$$

$$C_Q^2 \sim \overline{qw}_s^{\,2} \left(\frac{g}{T} \overline{\theta_v w}_s \right)^{-2/3} z^{-4/3}. \tag{3.10}$$

3.1.2 Mixed layer

In the mixed layer the turbulence structure continues to be insensitive to u_*. Deardorff (1970) hypothesized that in addition to z, z_i becomes an important length scale, because here, convective turbulence dominates mechanical turbulence, and in convective turbulence the largest eddies have a vertical scale of the order z_i. The velocity, temperature, and humidity scales are then replaced, respectively, by

$$w_* = \left(\frac{g}{T} (\overline{\theta_v w})_s \, z_i \right)^{1/3}, \tag{3.11}$$

$$\theta_* = \frac{(\overline{\theta w})_s}{w_*}, \tag{3.12}$$

$$m_* = \frac{(\overline{qw})_s}{w_*}. \tag{3.13}$$

Using these mixed-layer scales to nondimensionalize (3.8) - (3.10), Wyngaard and Lemone (1980) obtained

$$\frac{C_T^2 z_i^{2/3}}{\theta_*^2} = A(z/z_i)^{-4/3}, \tag{3.14}$$

$$\frac{C_{TQ} z_i^{2/3}}{\theta_* m_*} = B(z/z_i)^{-4/3}, \tag{3.15}$$

$$\frac{C_Q^2 z_i^{2/3}}{m_*^2} = C(z/z_i)^{-4/3}, \tag{3.16}$$

where A, B, and C are constants that again must be determined experimentally. Kaimal et al. (1976) tested this theory with data from the 1973 Minnesota experiment. They observed the mixed-layer height dependence of the temperature structure function parameter up to about 70% of the depth of the mixed layer. The value of $A = 2.7$ used for their analysis agrees with the value found by Wyngaard et al. (1971a) for the Kansas data. Similar results were obtained by Caughey and Palmer (1979) for another over-land case. Other results summarized by Wyngaard and LeMone (1980) for four marine boundary layers (MBLs) showed that the profiles of C_T^2, C_{TQ}, and C_Q^2 normalized by mixed-layer scales also had a $z^{-4/3}$ height dependence over at least some portion of the MBL. However, substantial deviations from this height dependence did occur, sometimes even at the lowest parts of the mixed layer (see Figs. 2 and 4 in Wyngaard and LeMone, 1980). These data also suggested that the values of A, B, and C are all different.

3.1.3 Interfacial layer

Wyngaard and LeMone (1980) realized that the strong peaks in C_T^2 and C_Q^2 observed near the inversion were caused by entrainment. Entrainment is the process which brings free tropospheric air into the boundary layer (Tennekes and Driedonks, 1981). Wyngaard and LeMone (1980) developed a model that predicts the values of the interfacial-layer[3] averaged structure function parameters using approximate forms of interfacial-layer averaged Corrsin relations. The interfacial-layer-averaged scalar dissipations were calculated by integrating the variance budget equations over the depth of the interfacial layer, where it was argued that dissipation was in balance with production. Because the scalar structure function parameters are a relatively weak function of ε (e.g., $C_T^2 \propto \varepsilon^{-1/3}$), a simpler parameterization was used for ε. They assumed that $\varepsilon(z)$ decreases linearly from its value at the bottom of the interfacial layer, where $\varepsilon \approx 0.4 g(\overline{\theta_v w})_s / T$ (Lenschow et al., 1980), to zero at the top. The resulting expressions (details of the calculations are given by Wyngaard and LeMone, 1980) for the interfacial-layer structure functions are

$$\langle C_Q^2 \rangle = \frac{3.9(\Delta Q)^2 \theta_{v*}}{z_i^{2/3} \Delta\Theta_v}, \tag{3.17}$$

$$\langle C_{TQ} \rangle = \frac{Q_i \theta_{v*}}{z_i^{2/3}}, \tag{3.18}$$

[3]The interfacial layer is defined by Deardorff (1979) to be the region at the top of the boundary layer where the virtual temperature flux is negative.

$$\langle C_T^2 \rangle = \frac{T_i \theta_{v*}}{z_i^{2/3}}, \tag{3.19}$$

where the angle brackets denote an average over the interfacial layer, $\theta_{v*} = (\overline{\theta_v w})_s / w_*$ is the mixed-layer virtual temperature scale, and $\Delta\Theta_v$ and ΔQ are the jumps in virtual temperature and humidity over the interfacial layer. The interfacial-layer humidity and temperature scales Q_i and T_i are given by

$$Q_i = \Delta Q \left[2.2 - \frac{2.4T}{\Delta\Theta_v} \frac{\Delta Q}{\rho} \right], \tag{3.20}$$

$$T_i = \Delta\Theta_v \left[0.5 - \frac{2.6T}{\Delta\Theta_v} \frac{\Delta Q}{\rho} + 1.4 \left(\frac{T}{\Delta\Theta_v} \frac{\Delta Q}{\rho} \right)^2 \right]. \tag{3.21}$$

Wyngaard and LeMone (1980) compared their model with observations from a limited number of cases where $\Delta\Theta_v$ and ΔQ were available and found good agreement despite the highly intermittent nature of the interfacial layer. However, it remained unclear how to calculate the structure function parameters in the region of transition from where the mixed-layer expressions are valid to where their interfacial-layer model is applicable.

3.1.4 The top-down/bottom-up approach

Realizing that the diffusion of scalar fluxes at the top and bottom of the boundary layer behave differently, Wyngaard and Brost (1984) developed a new and important approach to boundary-layer modelling that treats "top-down" and "bottom-up" processes separately. Entrainment fits naturally in this modelling framework because it is a top-down process. Fairall (1987b) used this technique to develop a model for C_T^2 and C_Q^2 that could be applied over the entire depth of the mixed layer. Like Wyngaard and LeMone (1980), he obtained the structure function parameters from the Corrsin relations, calculated the scalar dissipation rates from the scalar variance budget equations, and used the convective limit for ε in the form $\varepsilon^{1/3} \approx 0.7 w_* / z_i^{1/3}$.

However, with the top-down/bottom-up scaling approach, the total variance of a scalar is expressed as the sum of top-down and bottom-up components (Moeng and Wyngaard, 1984), e.g.,

$$\overline{\theta^2} = \overline{(\theta_b + \theta_t)^2} = \overline{\theta_b^2} + \overline{\theta_t^2} + 2\overline{\theta_t \theta_b}, \tag{3.22}$$

where the subscripts t and b refer to top-down and bottom-up, respectively. Variance budget equations are then maintained for each of the variance components in (3.22). Fairall (1987b) neglected the advection and local time rate of change terms in the budget equations and, thus, assumed that the dissipation term was in balance with the sum of the gradient production term and the transport term. He evaluated the gradient production term using existing top-down and bottom-up dimensionless gradient profile functions (Wyngaard and Brost, 1984; Moeng and Wyngaard, 1984) and the transport term using the large-eddy simulation (LES) results of Moeng and Wyngaard (1984). The resulting expressions for C_T^2 and C_Q^2 (see Fairall, 1987b for further details) are given by

$$\frac{C_T^2 z_i^{2/3}}{\theta_*^2} = [h_b(\xi) + R_\theta h_{tb}(\xi) + R_\theta^2 h_t(\xi)], \tag{3.23}$$

$$\frac{C_Q^2 z_i^{2/3}}{m_*^2} = [h_b(\xi) + R_Q h_{tb}(\xi) + R_Q^2 h_t(\xi)], \tag{3.24}$$

where $\xi = z/z_i$ and R_θ and R_Q are defined as the ratio of the entrainment flux to the surface flux. The dimensionless top-down and bottom-up gradient functions defined by Fairall (1987b) were modified by Fairall (1991) using the more recent top-down/bottom-up diffusion LES computations of Moeng and Wyngaard (1989)

$$h_b(\xi) = 10(-z_i/L)^{2/3}[\xi(1 - 7z/L)]^{-2/3}, \tag{3.25}$$

$$h_{tb}(\xi) = 8(1 - 0.8\xi), \tag{3.26}$$

$$h_t(\xi) = 10(1 - \xi)^{-2/3}(2 - \xi)^{-1}. \tag{3.27}$$

In the free convection limit, L drops out, and (3.25) is given by $h_b(\xi) = 2.7\xi^{-4/3}$.

Immediately, one can see that this model differs from those shown previously because it requires specification of the entrainment fluxes, which are often expressed in terms of the entrainment velocity, W_e. For example,

$$(\overline{\theta w})_i = -W_e \Delta\Theta. \tag{3.28}$$

However, the entrainment velocity is no easier to measure than the fluxes at the top of the boundary layer. Therefore, Fairall (1987b) used a parameterization for R_θ that he based on the result of Tennekes and Driedonks (1981) for the cloud-free, entraining, convective boundary layer: $W_e \approx 0.2(\overline{\theta w})_s / \Delta\Theta$. After including a term to account for entrainment induced by surface shear (Fairall, 1984), Fairall (1987b) arrived at

$$R_\theta = -0.2[1 + 3.2(-L/z_i)]. \tag{3.29}$$

He then computed R_Q from

$$R_Q = \frac{\Delta Q}{\Delta\Theta} \frac{\theta_*}{m_*} R_\theta. \tag{3.30}$$

Fairall (1987b) compared his model results against observations and found that the model was able to predict deviations from the mixed-layer prediction of a $z^{-4/3}$ height dependence that were qualitatively similar to those observed in the atmosphere. However, a profile-by-profile comparison yielded poorer results. Typically, the model underestimated the value of C_T^2 in the upper half of the boundary layer by as much as a factor of ten, suggesting that the effects of entrainment were being underestimated. Fairall (1987b) listed a variety of entrainment-producing mechanisms that were not included in his model that may have contributed to this result. Other possibilities he mentioned were that the effects of entrainment on C_T^2 may have been greater in the atmosphere than implied by the particular LES that he used or that some other aspect of the LES pertaining to his evaluation of the terms in the variance budget equations may have been inadequate.

One particular comparison reported by Fairall (1987b) involved C_Q^2 measurements made by Druilhet et al. (1983) where the surface humidity flux was negligible. In fact, the effects of entrainment were so dominant for this particular case that the C_Q^2 profile exhibited a positive slope with respect to z throughout the boundary layer. This was a particularly interesting case to analyze because it isolated the top-down component. For this comparison (see Fig. 6 in Fairall, 1987b) the top-down component of the model agreed well with the observations.

The qualitative picture that emerges from both observations and theory is that the profile of C_n^2 decreases in the surface layer according to M-O similarity, becomes a weaker function of z (depending on the influences of entrainment) in the mixed layer, increases sharply to a peak associated with the inversion capping the mixed layer, and then decreases rapidly to its free tropospheric value above the boundary layer. Comparisons between the structure function parameter profiles observed by remote-sensing techniques and the models

described above require measurements of the stress and scalar fluxes at the surface as well as the scalar jumps at the inversion. The radar used in my research is not capable of observing the expected surface-layer behavior except for extremely deep (~3 km) boundary layers because of its minimum detectable range (~150 m) and maximum vertical resolution (60 m).

3.2 Dissipation Rate Profiles

The rates of turbulent kinetic energy (TKE) dissipation and scalar dissipation are important because these quantities appear as terms in the second-order budgets of momentum and scalar variances. Unfortunately, only a few data bases include complete profiles of ε and χ, mainly because of the difficulty and expense associated with obtaining in situ measurements over the entire depth of the boundary layer. As shown in Chapter 2, inertial range turbulence theory allows us to relate dissipation rates to structure function parameters. The scalar dissipation rates are not determined independently because χ appears as a product with $\varepsilon^{-1/3}$ in the scalar Corrsin relations. For velocity, there is a direct relationship between the velocity structure function parameter and $\varepsilon^{2/3}$.

3.2.1 Surface layer

Using data from the Kansas experiment, Wyngaard and Coté (1971) derived empirical functions for the normalized TKE dissipation rate, $k_a z\varepsilon/u_*^3$, as a function of z/L. Kaimal et al. (1976) replaced z and u_* with mixed-layer scales and arrived at an asymptotic surface-layer prediction for C_v^2,

$$\frac{C_v^2 z_i^{2/3}}{w_*^2} = \text{constant}. \qquad \textbf{(3.31)}$$

They observed that a constant value of C_v^2 is reached only at heights above $0.1z_i$. In the region $0.01z_i \le z \le 0.1z_i$, they found C_v^2 to be approximated by

$$\frac{C_v^2 z_i^{2/3}}{w_*^2} = 1.3 + 0.1(z/z_i)^{-2/3}. \qquad \textbf{(3.32)}$$

Assuming $C_v^2 \approx 2\varepsilon^{2/3}$,

$$\frac{\varepsilon z_i}{w_*^3} = \left[\frac{1.3 + 0.1(z/z_i)^{(-2/3)}}{2}\right]^{3/2}. \qquad \textbf{(3.33)}$$

The same general behavior was observed by Lenschow et al. (1980) with aircraft data from the Air Mass Transformation Experiment (AMTEX), although the AMTEX values of ε were consistently smaller than those observed in Minnesota. In addition, the value of 1.5 for the constant in (3.31) evaluated by Kaimal et al. (1976) was higher than the value of unity reported by Wyngaard and Coté (1971) for the Kansas data.

On the other hand, the values of ε measured in the upper part of the boundary layer over Aschurch, England, merged quite well with the Minnesota data, even though the topography was markedly different at the two sites (Caughey and Palmer, 1979). This suggests that the disagreement involving the constant in (3.31) may be partially explained by differences in the measurement techniques. During the Kansas experiment, ε was calculated from the fluctuating velocity time series measured by hot-wire probes mounted on a tower. For both the Minnesota and Aschurch data sets, ε was determined by analyzing the inertial subrange of velocity spectra measured by turbulence probes mounted on a balloon tether. As reported by Haugen et al. (1975), balloon motion can cause overestimates in the longitudinal and lateral wind variances measured on a balloon tether by as much as 15–30%. The corresponding velocity spectra must then also be affected, as recognized by Kaimal et al. (1976), who attempted to correct the Minnesota velocity spectra for motion contamination.

The variances of temperature and vertical velocity were much less affected by balloon motion in the study by Haugen et al. (1975). Since the temperature spectra are also less likely to be corrupted, it is not surprising to find less scatter in the normalized C_T^2 data than in any other variable examined by Kaimal et al. (1976). Using $C_T^2 \approx 3.2N\varepsilon^{-1/3}$, where N is the dissipation rate of $\theta^2/2$, Kaimal et al. (1976) also demonstrated that $N\varepsilon^{-1/3}$ obeyed the $z^{-4/3}$ height dependence predicted by the local free convection theory of Wyngaard et al. (1971a). Lenschow et al. (1980) showed the same behavior for χ_Q down to a height of $0.01z_i$.

3.2.2 Mixed layer and interfacial layer

As mentioned earlier, Kaimal et al. (1976) found that C_v^2 approached a constant above $0.1z_i$. In the Minnesota data, this behavior was observed up to the inversion, although there was some indication of a slight decrease in C_v^2 near the inversion, which was more pronounced in the ε profiles measured by Caughey and Palmer (1979) and Lenschow et al. (1980). This behavior is also observed in numerical and laboratory studies (Deardorff, 1974; Willis and Deardorff, 1974).

The profile of N also approaches a constant in the mixed layer but at a much higher level in the boundary layer: $0.5z_i$ for the Minnesota data (see Kaimal et al., 1976). However, in contrast to C_v^2, N has an elevated maximum associated with the inversion capping the mixed layer. Caughey and Palmer (1979) showed an increase in N of nearly an order of magnitude over its mixed layer value beginning at about $0.7z_i$. Above the inversion both N and C_v^2 decrease as a result of a reduction in high-frequency temperature and velocity fluctuations (Caughey and Palmer, 1979).

4. THE NOAA 915-MHZ BOUNDARY-LAYER RADAR/WIND PROFILER

4.1 System Description

The National Oceanic and Atmospheric Administration (NOAA) 915-MHz boundary-layer radar/wind profiler (NBL radar)[4] (Fig. 4.1) was developed at the NOAA Aeronomy Laboratory (Ecklund et al., 1988). The radar was designed to provide wind profiles in the lower troposphere at up to 60-m vertical resolution. The conceptual design was based on earlier work by Ashkenazy et al. (1983). The first operation of the prototype occurred during the summer of 1986. Since then, these radars have been used by NOAA and other research organizations on land, on ice, and onboard ships, at dozens of sites throughout the world.

Portability requirements dictated that the system be rugged, lightweight, and easily transportable. Aeronomy Laboratory engineers met these requirements by using microstrip technology in the design of the radar antenna. The particular NBL radar deployed at the Boulder Atmospheric Observatory (BAO) uses a single, flat, square, phased-array antenna. The antenna consists of four 1-m by 1-m panels, giving an aperture of 4 m^2. Each panel contains 16 individual microstrip patches. The circuit board for each patch contains all requisite etched transmission lines and is phased for broadside radiation (Ecklund et al., 1988). An antenna enclosure was designed to help reduce the impact of ground clutter (Russell and Jordan, 1991). The definitions and values of the principal operating parameters and characteristics for the NBL radar during the BAO experiment are given in Table 4.1.

4.2 Signal Processing

The return backscattered signals received by the radar undergo five steps in signal processing: detection, ranging, coherent integration (time domain averaging), spectral analysis, and incoherent integration (spectral averaging). The resulting Doppler velocity spectrum is then numerically analyzed to provide the spectral moments. In the remainder of this section, I discuss these processing steps in detail.

4.2.1 Detection and ranging

First, the return signal must be coherently detected. The radio frequency (RF) signal is mixed with a coherent local (reference) signal and down-converted to an intermediate frequency (IF) before it is passed to a quadrature detector. At this point, the complex signal plus noise, $s(t)$, can be expressed in the form (Röttger, 1988)

---

[4]The portable NOAA 915-MHz radar discussed here should not be confused with the much larger NOAA 915-MHz radar that is permanently installed at Stapleton Airport in Denver, Colorado.

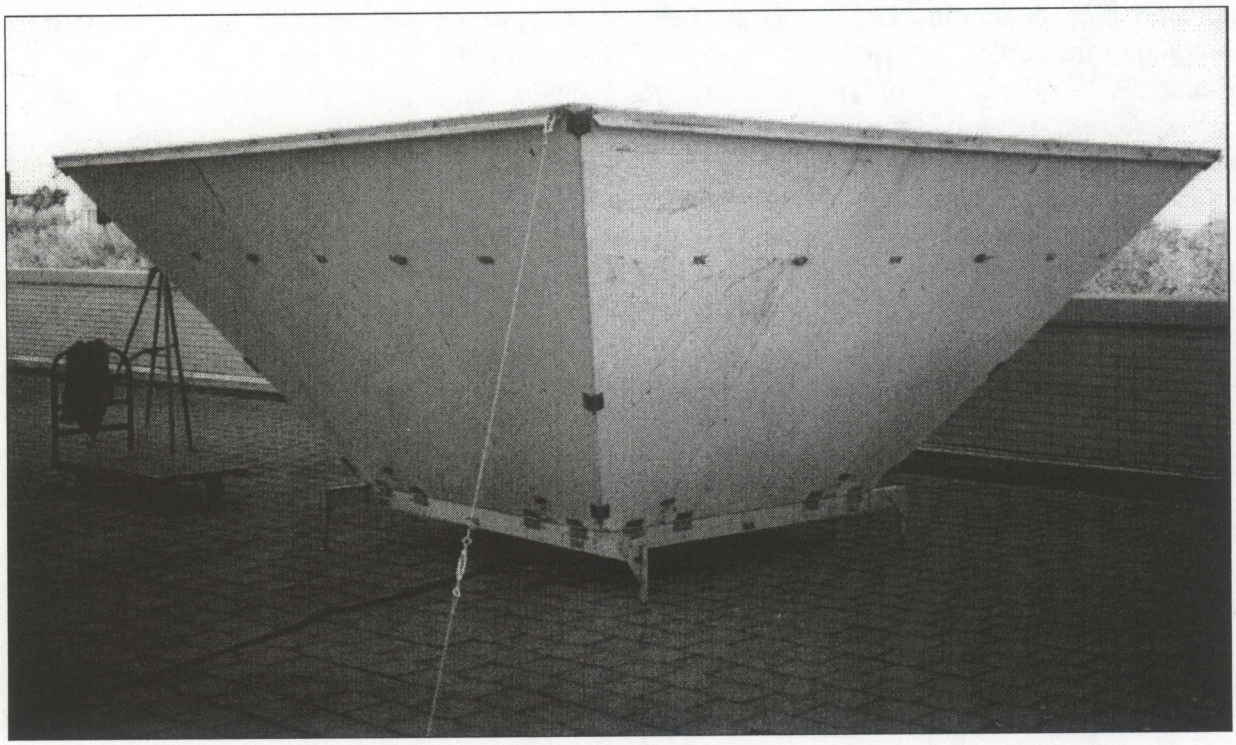

Figure 4.1. The NOAA 915-MHz boundary-layer radar/wind profiler shown with its clutter fence enclosure. The radar antenna (not visible) is located near the base of the clutter fence.

$$s(t) = x(t) + iy(t), \tag{4.1}$$

where $x(t) = a(t)\cos[\theta(t)]$ and $y(t) = a(t)\sin[\theta(t)]$ are the quadrature components (I and Q). The amplitude $a(t)$ is the sum of the squared amplitudes of the received premixed, band-limited signals. The time-varying nature of the phase $\theta(t)$ is caused by changes in position and scattering efficiency of the scatterers in the radar volume. Quadrature detection produces time series of sine and cosine components, which are digitized in the analog-to-digital (A/D) converters.

Table 4.1
NBL radar characteristics and operating parameters.

Symbol	Parameter	Value	
		Standard Pulse	Coded Pulse
λ	Wavelength (cm)	32.8	32.8
A_p	Physical antenna area (m^2)	4	4
θ	Beamwidth (deg)	12	12
τ	Pulse width (ns)	400	400
	Coded pulse width (ns)	N/A	1600
IPP	Interpulse period (μs)	25	32
ΔR	Range resolution (m)	60	60
P_t	Peak pulse power (W)	500	500
n_c	Number of coherent integrations	320	250
n_f	Number of FFT points	64	64
n_s	Number of spectral averages	30	30
T_{rx}	Receiver noise temperature (K)	150	150
T_s	Sky noise temperature (K)	30	30
ψ	Beam elevation angle	90	90

The digital signals are then sampled at discrete time intervals. The range gate height or simply range, R, is given by

$$R = \frac{c t_r}{2}, \tag{4.2}$$

where $c = 3.0 \times 10^8$ m s^{-1} is the speed of light and t_r is the round-trip travel time between transmission and detection. A similar expression is given for the range resolution, ΔR:

$$\Delta R = \frac{c \tau}{2}, \tag{4.3}$$

where τ is the transmitted pulse width in seconds.

4.2.2 Coherent integration

The next step in signal processing is coherent integration, also referred to as time-domain averaging. This process averages n_c consecutive phase-coherent pulses, thereby reducing the number of data points by a factor of n_c. But the primary benefit of coherent integration is an improvement in the signal-to-noise ratio (SNR). When the random noise amplitudes of the complex signal are integrated over n_c samples, the resultant noise power is increased by n_c. On the other hand, when n_c coherent signals are summed, the resultant signal amplitude is increased by n_c; thus, the integrated signal power is increased by n_c^2. Consequently, the coherent integration of n_c pulses improves the SNR by a factor of n_c. However, in the radar signal processing program, the integrated amplitudes for signal and noise are normalized by n_c. Therefore, the signal power remains constant with coherent integration, and the enhancement in SNR is seen as a reduction in noise power.

The number of samples used in the integration must be carefully selected. To ensure phase coherence between pulses, the integration period, Δt, must be shorter than the typical time scale of the signal variations. Signal phase and amplitude variations are caused by movement of scatterers relative to each other within the scattering volume, the mean movement of scatterers by the background wind, and changes in the relative efficiency of individual scatterers. The relative motions of the scatterers are estimated by a correlation time, which depends on the radar wavelength, antenna beamwidth, and the sensed altitude (Gossard and Strauch, 1983).

The sampling frequency defined by Δt determines the maximum frequency that can be resolved after integration. Since at least two points within one cycle are needed to specify a sinusoidal oscillation, the maximum frequency that can be resolved, or the Nyquist frequency, f_N, is equal to half of the sampling frequency:

$$f_N = \frac{1}{2\Delta t}. \tag{4.4}$$

Signals with frequencies outside of $\pm f_N$ will leak through and contaminate or alias the signal within the fundamental frequency band. An inherent feature of coherent integration is that it bandpass filters the return signals, thereby significantly reducing the intensities of components outside of $\pm f_N$.

4.2.3 Spectral processing

A set of n_f coherent integrations is processed by the Fast-Fourier transform (FFT) method, where n_f is a power of 2. The direct current (DC) component is zeroed out and the transform is then interpolated across DC. In more recent versions of the radar control program, the long-term mean value at DC is subtracted from the transform. DC filtering is done primarily to remove energy resulting from ground clutter. Ground clutter refers to radar backscatter from non-atmospheric targets such as trees, buildings, power transmission lines, and, in our case, the BAO tower and its guy wires. Clutter in a more general sense includes reflections from insects, birds, and airplanes, as well as from other radio frequency transmissions. Clutter can occur in both the main part of the transmit beam and in its side lobes. Here, we are concerned with any interference at or near DC. It is important to note that even if ground clutter did not exist, DC filtering would be required in about the lowest 1 km of range gates because residual transmit power leaks out of the circulator and into the receiver electronics, resulting in a significant DC component (Jordan, 1995).

The user has the option of applying a Hanning window to the transformed data to reduce the effect of spectral leakage caused by using time series of finite length. In the time domain, windowing is equivalent to multiplying the time series by the window function. In the spectral domain, this process is represented by the convolution of the Fourier transforms for the time series and window function. An attractive feature of the Hanning window is that under the discrete Fourier transform, windowing in the spectral domain is equivalent to multiplying the coefficients of the transform by the weighting function (-1/4 +1/2 -1/4) (Harris, 1978). The position of the peak in the Doppler velocity spectrum does not change when the window is applied. Therefore, the window does not affect the accuracy of the velocity measurement. However, windowing will broaden the spectrum and, therefore, have an impact on the estimate of the spectral width and its application to velocity microturbulence.

The last step of spectral processing computes the power spectrum by squaring the transform. When the frequency scale is converted to a velocity scale, the power spectrum is referred to as a Doppler velocity spectrum. The radial velocity, v_r, is related to the mean Doppler frequency shift, f_D, by

$$v_r = \frac{\lambda f_D}{2}, \tag{4.5}$$

where a positive radial velocity is defined in the direction pointing toward the radar. An example of a typical Doppler velocity spectrum is shown in Fig. 4.2.

4.2.4 Incoherent integration

The last stage of signal processing is incoherent integration, or spectral averaging. The effect of this process is to improve the detectability of the signal. Referring to Fig. 4.2, the detectability, D, of a Doppler velocity spectrum is defined as

$$D = \frac{P_S}{\sigma_N}, \tag{4.6}$$

where P_S is the peak spectral density of the signal spectrum, and σ_N is the standard deviation of noise spectral density.

To understand how incoherent integration effects detectability, consider a random variable x with a Gaussian distribution,

$$a(x) = \frac{1}{(2\pi)^{1/2}} \exp(-x^2/2), \tag{4.7}$$

where the mean value and standard deviation are assumed to be 0 and 1, respectively. When intensities of x are integrated or summed as

$$y = x_1^2 + x_2^2 + x_3^2 + \ldots\ldots x_M^2, \tag{4.8}$$

it can be shown that y has a χ^2 distribution with mean value, $\mu = M$, and standard deviation $\sigma = (2M)^{1/2}$, where M is called the degrees of freedom of the χ^2 distribution. The ratio between the mean value and standard deviation becomes

$$\frac{\mu}{\sigma} = \left(\frac{M}{2}\right)^{1/2}. \tag{4.9}$$

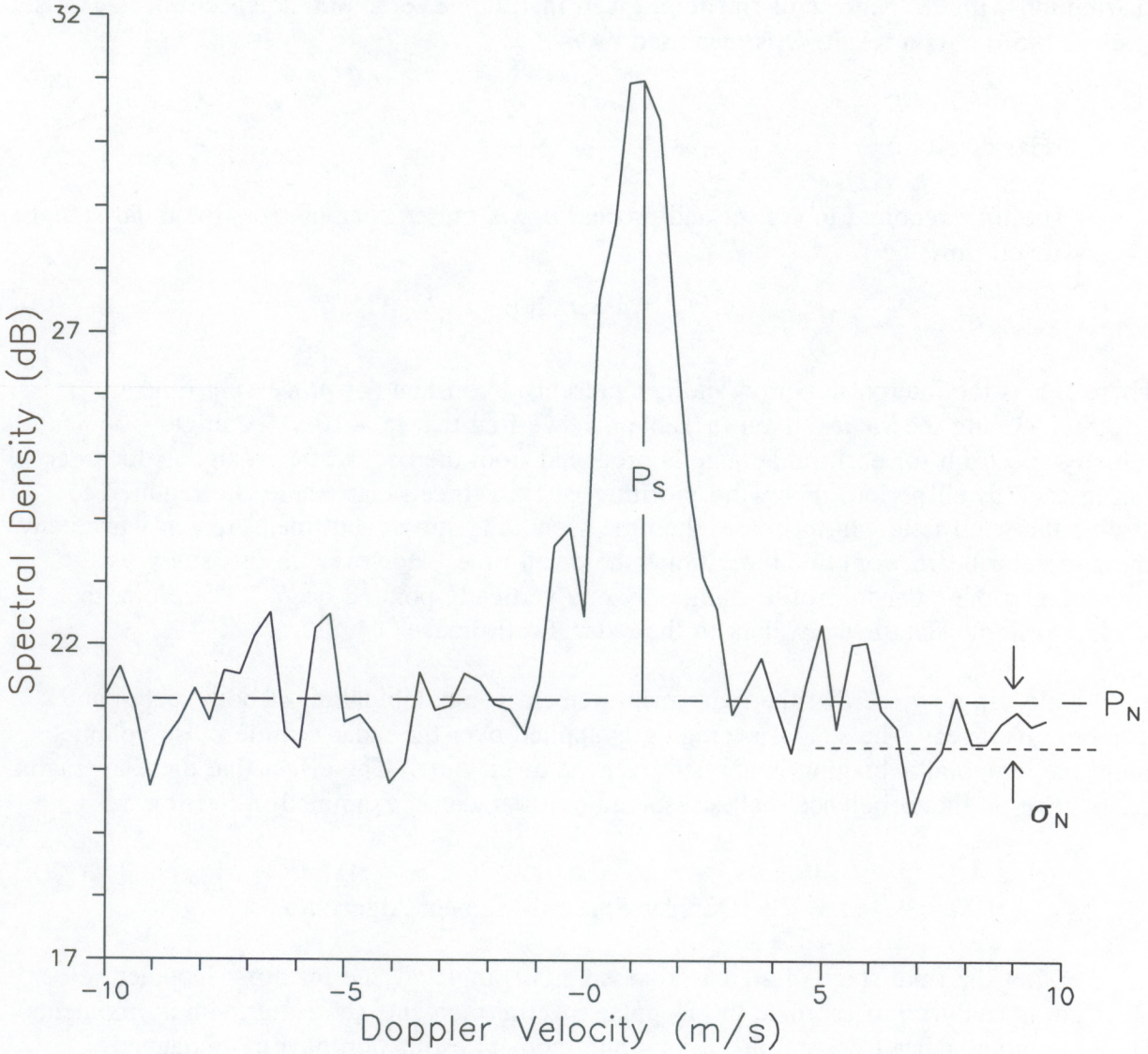

Figure 4.2. A typical Doppler velocity spectrum measured with the NBL radar from the third radar range gate centered at 278 m AGL. The spectrum was measured at Erie, Colorado, on 26 July 1993 beginning at 00:08:52 GMT. The spectral processing parameters are those listed for the standard pulse in Table 4.1. Spectral densities for the signal peak and noise are denoted by P_S and P_N, respectively. The standard deviation of noise spectral density is represented by σ_N. The dB scale for spectral density is referenced to 1 W s m^{-1}.

When n_s spectra are averaged, the mean values for the spectral densities of both the signal and noise do not change. Therefore, the ratio P_S/P_N remains unchanged. But according to (4.9), the ratio P_N/σ_N becomes $n_s^{1/2}$ because n_s integrations of the noise produces a χ^2-distribution with $2n_s$ degrees of freedom, given that the noise amplitude spectrum is Gaussian (Tsuda, 1988). As a result, D is increased by $n_s^{1/2}$.

4.2.5 Radar dwell time

The time required to collect and process $n_c n_f n_s$ pulses characterizes the radar sampling time or dwell time, t_D:

$$t_D = n_c n_f n_s \, \mathrm{IPP} + t_p, \tag{4.10}$$

where IPP is the interpulse period and t_p represents a constant for processing time ($\approx$ 0.5 s). Using the values given in Table 4.1, we find that $t_D \approx 16$ s. A single Doppler velocity spectrum for each range gate is produced from the backscattered signals recorded during each dwell period. For wind profiling, at least three radar beams are required to resolve the wind field. In this case, the time separating subsequent measurements from any one particular beam would be three times the dwell time. However, in this study we programmed the radar to profile using only one vertically pointed beam. Therefore, the resolution in our data is equivalent to the radar dwell time.

We can now see that the radar measurement is a combination of both spatial and temporal averages. The spatial averaging is applied over the radar's finite pulse volume, while the temporal averaging is applied over the dwell time. The effect that these averaging filters have on the turbulence that is resolved by the radar is examined in Section 5.3.1.

4.3 The Doppler Spectral Moment Algorithm

After the final stage of signal processing is completed, the resulting Doppler velocity spectrum is analyzed to estimate the Doppler spectral moments (hereafter, simply moments). The basic approaches to signal processing and moment estimation have not changed significantly from the time that automated signal processing was first implemented with the research wind profilers. However, now that the routine use of wind-profiler data for both research and commercial purposes has uncovered a number of quality-control problems (e.g., Wilczak et al., 1995), there has been increasing pressure from a growing user community to reexamine the profiler signal processing and moment estimation procedures. At the time of this work, a research program devoted to this problem is underway at the NOAA/Environmental Technology Laboratory (ETL).

4.3.1 Signal, noise, and the spectral moments

First, the mean noise spectral density (or noise "floor"), P_N, is estimated objectively using the technique of Hildebrand and Sekhon (1974). The total noise power per velocity bin, $N/\Delta v$, is then calculated by multiplying P_N by the transform length (64 in our case). Next, the position of the peak in the spectrum is determined simply by locating the maximum spectral density. The signal is then interpreted as the interval on either side of the spectral peak where the spectral density is greater than P_N.

The noise floor is subtracted from the spectral values over the signal interval before calculating the moments. The 0th moment gives an estimate of the total signal power per velocity bin, $S/\Delta v$:

$$\frac{S}{\Delta v} = \sum_{i=v_1}^{v_2} (P_i - P_N), \tag{4.11}$$

where P_i are the spectral values between the points (v_1 and v_2) where the spectrum crosses the noise floor. The SNR is then defined as the ratio, S/N. The first moment gives a reflectivity weighted radial velocity estimate:

$$v_r = \frac{\sum_{i=v_1}^{v_2} i(P_i - P_N)}{S/\Delta v}. \tag{4.12}$$

The second moment gives an estimate of the radial velocity variance:

$$\sigma_v^2 = \frac{\sum_{i=v_1}^{v_2} (i - v_r)^2 (P_i - P_N)}{S/\Delta v}. \tag{4.13}$$

Spectral width is defined as $2\sigma_v$. Careful scrutiny must be applied to each set of moments, since the algorithm produces values even when there is no detectable signal.

4.3.2 Ground-clutter suppression

Ideally, all of the energy resulting from ground clutter would reside in the single frequency bin at DC, in which case the DC filtering discussed in Section 4.2.3 would eradicate the clutter. However, this is rarely, if ever, the case. Clutter is broadened in the frequency domain by the wind (e.g., moving leaves on trees or vibrating wires). In addition,

artificial broadening occurs because of the signal processing. To combat the problem, Anthony Riddle of the NOAA Aeronomy Laboratory developed a ground-clutter algorithm.

The algorithm uses a type of spatial (in height) pattern recognition to determine if ground clutter is present in a Doppler velocity spectrum. The user specifies the height below which the ground-clutter algorithm is to be applied. Within this range, if the algorithm detects a signal that is nearly symmetric about DC, then those points from the spectrum are ignored in the search for the peak signal. However, if the signal detected at the height immediately above the range covered by the algorithm is very close to DC, then the algorithm is turned off for all heights below.

This algorithm has been shown to be quite effective in retrieving the atmospheric signals from spectra measured by oblique beams that are contaminated by ground clutter. However, it is unclear how well the algorithm works with vertical-velocity spectra because the part of the spectra resulting from atmospheric backscatter often overlaps with the ground-clutter portion of the spectra. This makes identification and separation of the two components more difficult. Therefore, it is best to choose a radar site that minimizes ground clutter for radar applications that make use of the measured vertical velocities.

4.4 Data Acquisition

The profiler operations and data acquisition are controlled by the profiler on-line program (POP). The software runs on a personal computer (PC) equipped with a digital signal processing (DSP) card for expediting the DSP computations. A consensus algorithm is used to produce average wind profiles over a specified averaging period (e.g., 1 hour) from the individual radial velocities measured by the radar. However, in this work I am more interested in the high time-resolution Doppler velocity spectra.

The first three moments of the velocity spectrum are calculated in POP and recorded on a chosen storage medium. In the past, the cost of massive storage media, or, alternatively, the cost associated with a technician transferring data periodically to smaller storage media, dictated that only the moments of the spectra be recorded. However, with the advent of optical media, it is now practical to record the complete Doppler velocity spectra. This additional information is often needed to evaluate completely the integrity of the spectral moments. Currently, the spectra and moments are stored in a compressed (binary) format. Special software has been written at NOAA/ETL to allow users quick and easy access to the radar moments data in the form of time-height displays.

4.5 The Doppler Radar Reflectivity Equation

The radar reflectivity or scattering cross section per unit volume, η, is a measure of the radar-scattering intensity. In clear air, this intensity is caused by refractive-index

fluctuations present in the scattering volume. If the radar half-wavelength lies within the inertial subrange, then (Hardy et al., 1966)

$$C_n^2 = \frac{\eta}{0.38}\lambda^{1/3}, \tag{4.14}$$

where η is in m^{-1} and λ is in meters, giving units of $m^{-2/3}$ for C_n^2. The goal here, then, is to relate η to a quantity that is directly measurable by the radar. The more common approach is to calibrate the power output by the signal processor. However, this technique is based on a receiver calibration that depends on the radar operating parameters in use at the time of the calibration. A different approach that relates SNR to η avoids this problem by not requiring a separate receiver calibration.

Starting with the radar equation of Probert-Jones (1962), the power received at the antenna port, P_r, is related to the transmit power, P_t, by

$$P_r = \frac{c\tau\lambda^2 P_t G_o^2 \theta\phi\eta}{1024\pi^2 \ln(2) R^2}, \tag{4.15}$$

where G_o is the antenna gain and θ and ϕ are the beamwidths describing the shape of the transmitted beam (i.e., if $\theta = \phi$, then the beam is conical). We use two expressions for the antenna gain,

$$G_o\theta\phi \approx \pi^2 \tag{4.16}$$

and

$$G_o = \frac{4\pi A_e}{\lambda^2}, \tag{4.17}$$

where A_e is the effective antenna area, to obtain

$$P_r = \frac{\pi c\tau P_t A_e \eta}{256 \ln(2) R^2}. \tag{4.18}$$

The effective antenna area is related to the physical antenna area, A_p, by the antenna efficiency. This relationship is well-known for the more conventional parabolic antennas, but has not yet been determined for the flat, rectangular, phased-array design. Because A_e is unknown, I introduce the radar "system" efficiency parameter, α, to account for the antenna

efficiency, and I use A_p in place of A_e. I also use α to account for absorptive and radiative losses in the transmission line and antenna (VanZandt et al., 1978). The signal power at the input to the receiver, S, is then given by

$$S = \frac{\pi \alpha^2 P_t A_p \sin(\psi) \eta \Delta R}{128 \ln(2) R^2}, \tag{4.19}$$

where I use (4.3) to replace $c\tau$ by $2\Delta R$. A factor of $\sin(\psi)$, where ψ is the beam elevation angle, appears in the numerator of (4.19) for cases when $\psi < 90°$. Note that two factors of α are required to account for the two-way losses in the transmission line and antenna.

We obtain the system noise power, N, from

$$N = k_B T_o B_N, \tag{4.20}$$

where $k_B = 1.3803 \times 10^{-23}$ J mol^{-1} K^{-1} is Boltzmann's constant, B_N is the receiver noise bandwidth, and T_o is the system noise temperature, given by

$$T_o = \alpha T_s + T_{rx}, \tag{4.21}$$

where T_s and T_{rx} are the noise temperatures in degrees Kelvin for the sky and for the radar receiver, respectively. At 915 MHz, the geometric-mean galactic temperature for an elevation angle of 90° is about 30 K (Doviak and Zrnić, 1984). Because $\alpha < 1$, and given the value of T_{rx} from Table 4.1, we expect $\alpha T_s << T_{rx}$. Therefore, it is a reasonable approximation to neglect sky noise in this analysis. The receiver noise bandwidth is inversely proportional to τ:

$$B_N \approx \frac{1}{\tau} = \frac{c}{2\Delta R}. \tag{4.22}$$

If we substitute (4.22) in (4.20) and let $T_o = T_{rx}$, then

$$N = \frac{c k_B T_{rx}}{2\Delta R}. \tag{4.23}$$

The SNR at the input to the signal processor is found by dividing (4.19) by (4.23):

$$\frac{S}{N} = \frac{\pi\alpha^2 P_t A_p \sin(\psi)}{64\ln(2)ck_B T_{rx}}\left(\frac{\Delta R}{R}\right)^2 \eta. \tag{4.24}$$

The SNR at the output of the signal processor is a factor of n_c larger than the value given by (4.24) because of the enhancement associated with coherent integration (see Section 4.2.2). Solving for η, we obtain

$$\eta = \frac{64\ln(2)ck_B T_{rx}}{\pi\alpha^2 P_t A_p \sin(\psi) n_c}\left(\frac{R}{\Delta R}\right)^2 \text{SNR}. \tag{4.25}$$

Once α has been determined, (4.25) allows us to calibrate radar reflectivity measurements, which in turn can be used to determine C_n^2. Substituting (4.25) in (4.14) gives us

$$C_n^2 = \frac{1.54\times 10^{-13} T_{rx}\lambda^{1/3}}{\alpha^2 P_t n_c A_p \sin(\psi)}\left(\frac{R}{\Delta R}\right)^2 \text{SNR}. \tag{4.26}$$

We now see the advantage of using a radar equation based on SNR rather than signal power. Note that in (4.25) the radar system noise power is known, so that calibrated values of η can be obtained from SNR measurements. No calibration of the radar receiver is required because noise and signal undergo the same processing steps. On the other hand, if we calibrated the received power in terms of the signal power at the output to the signal processor, then a new calibration would be required every time the signal processing parameters or the gain of a receiving component were changed.

5. MEASUREMENT ANALYSES

This chapter summarizes the results obtained during the Boulder Atmospheric Observatory (BAO) Radar Calibration Experiment conducted in July 1993. In Section 5.1, following a brief overview of the in situ sensors used in this study, the theory summarized in Chapter 2 is applied to the measured time series of scalar and velocity fluctuations in order to calculate the desired structure function parameters. Section 5.2, then, compares the measurements of C_n^2 made on the tower with the remotely-sensed measurements of C_n^2 made by the National Oceanic and Atmospheric Administration (NOAA) 915-MHz boundary-layer radar/wind profiler (NBL radar) in order to calibrate radar reflectivity, which is the

fundamental measurement of the radar. Section 5.3 considers radar measurements of velocity turbulence. I first examine the filtering associated with the radar sampling, using both theory and observations. I then use an established technique modified to account for dwell time averaging to estimate C_u^2 from the radar measurement of spectral width and compare these results with the results obtained from the turbulence sensor mounted on the tower.

5.1 Tower Measurements

5.1.1 Turbulence sensors

I selected state-of-the-art fast response sensors to obtain direct in situ measurements of velocity, temperature, and humidity microturbulence. For velocity and temperature, I used the ATI 200-kHz sonic anemometer/thermometer (hereafter "ATI"). For humidity, I used the Ophir fast infrared hygrometer (hereafter "Ophir"). Engineers from the Environmental Technology Laboratory (ETL) mounted these instruments on a 3-m boom at the 250-m level of the BAO tower (see Fig. 5.1).

The ATI measured fluctuations in temperature and the three-dimensional wind field at a rate of 10 Hz. The Ophir measured coincident fluctuations in absolute humidity at a rate of 20 Hz. The humidity data were then pair-averaged to 10 Hz to match the resolution of the ATI. I acquired the signals from both instruments with a common personal computer (PC)-based data system. The data-acquisition program calculated means, variances, and covariances for each 15-min data segment. In addition, the program produced spectra and cospectra using an 8192-point Fast-Fourier transform (FFT). The time series were tapered with a Hamming window prior to computing the FFT to reduce spectral leakage. The resulting power spectra were smoothed in a manner that maintains roughly equivalent spacing between frequency points on a logarithmic plot. The variances, covariances, spectra, and cospectra were rotated into the mean wind direction measured by the ATI. The 15-min statistics and spectral data were recorded in hourly files on magnetic tape. The 10-Hz data were not saved, because the data-acquisition and real-time processing program used up most of the available computational resources on the PC we used.

5.1.2 Mean sensors and instrument comparisons

In addition to the turbulence measurements, I obtained mean measurements of wind speed, direction, temperature, and dew point at five levels on the tower (100 m, 150 m, 200 m, 250 m, 300 m). The RM Young (Model 8002) propvane anemometer provided the wind measurements and the EG&G (Model 200M) probe was used for temperature and dew point (see Fig. 5.1). The data from these sensors were acquired with Campbell Scientific (Model CR-21X) data loggers. The data (5-min means) were then transferred to the ETL via phone lines. The configuration of instrument booms on the BAO tower at the 250-m level is shown in Fig. 5.2.

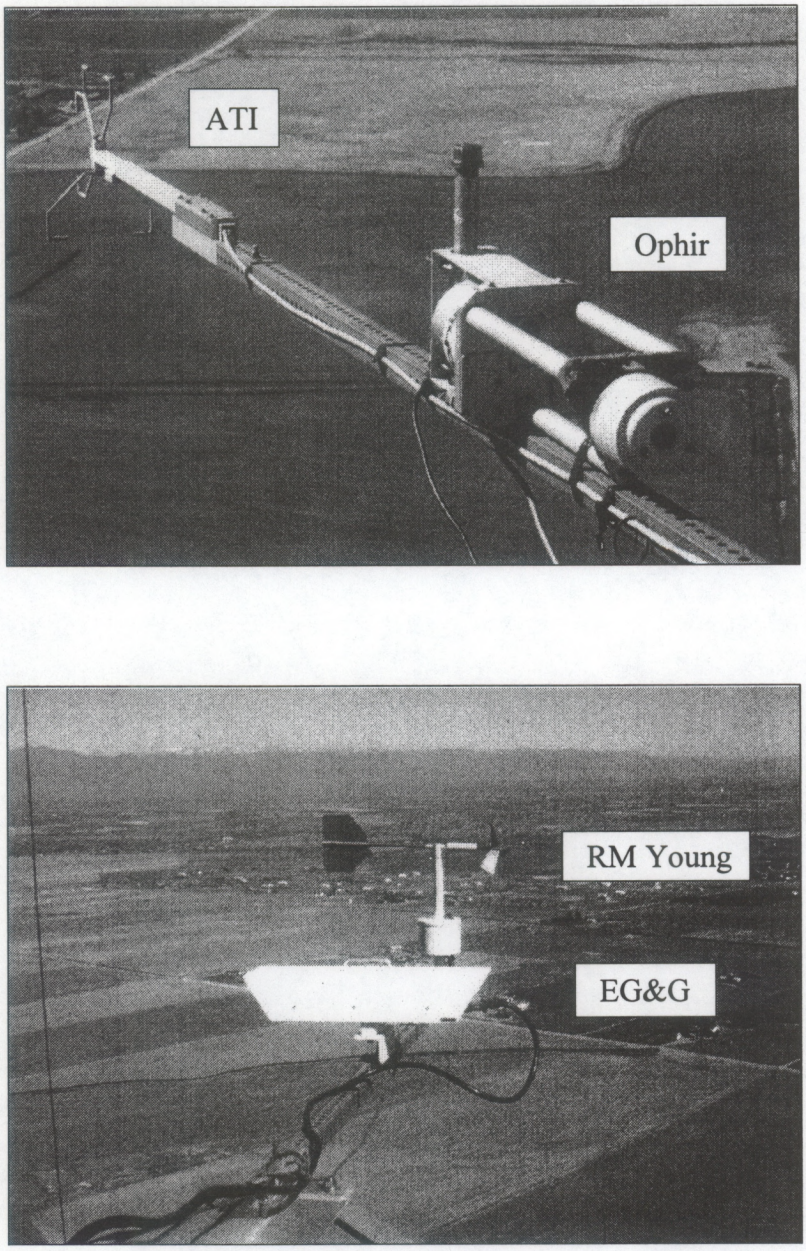

Figure 5.1. Photographs showing the sonic anemometer (ATI) and infrared hygrometer (Ophir) mounted on the turbulence sensor boom (top) and the propvane anemometer (RM Young) and mean temperature/dew- point sensor (EG&G) mounted on the mean sensor boom (bottom). Both booms are attached to the BAO tower at the 250-m level. The boom orientations are shown in Fig. 5.2.

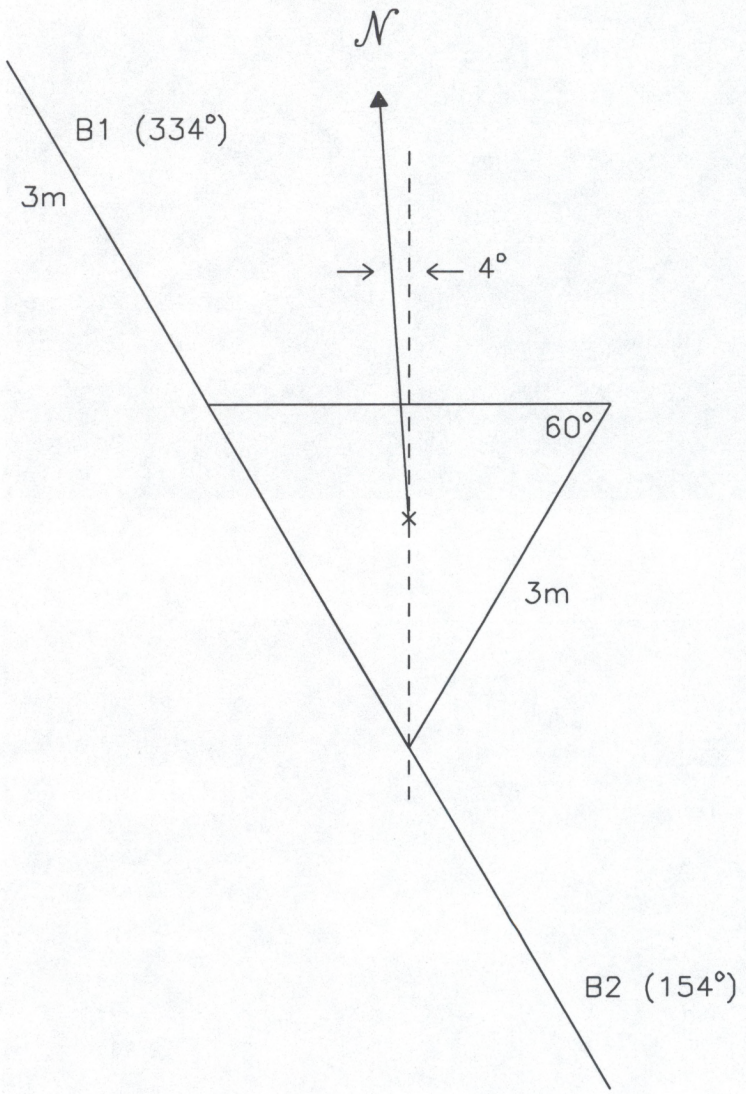

Figure 5.2. Configuration of the 250-m tower level depicting the tower structure (solid lines forming the equilateral triangle) and the orientation of the mean sensor (B1) and turbulence sensor (B2) booms. The center line of the tower (dashed line) is rotated 4° from north.

I produced 15-min averages from the mean sensor measurements and compared them to the mean values measured by the turbulence sensors. Validation of the mean winds measured by the ATI is important, since I use the mean wind speed and direction in the application of Taylor's hypothesis. The data-acquisition program also uses the mean wind direction to rotate the second moment and spectral velocity data. The mean temperature and humidity from the turbulence sensors are used to calculate refractivity (see Section 5.1.3).

A comparison of wind velocity data from all wind directions indicated flow contamination caused by the tower structure. A schematic indicating the estimated range of the contaminated wind directions for each of the instrument booms is shown in Fig. 5.3. The lines tangent to the tower from the tip of each boom span an angle of 30°. To be conservative I added an additional 30° to either side of this angle, giving a total contamination sector of 90° for each boom. I used the remaining flow directions (34-94 deg and 184-304 deg) in the wind comparisons.

Scatterplots comparing the mean north-south, U, and east-west, V, components, speed, and direction measured by the sonic and propvane anemometer are shown in Fig. 5.4. Although the data are highly correlated, there is a noticeable bias for the larger magnitudes of both velocity components and the resultant speed. Because I could not determine which instrument caused these unexpected biases, I decided to compare the sonic anemometer data from the 250-m level with the propvane anemometer data from adjacent levels (i.e., 200 m and 300 m). The results of the comparisons for all three levels are summarized in Table 5.1. Notice that the correlation is slightly lower and the scatter is larger for the wind comparisons between adjacent levels (i.e., at 200 m and 300 m), but the linear regression slope is much closer to 1.0. Therefore, I attribute much of the difference between the mean winds measured at the 250-m level to calibration errors involving the propvane anemometer at that location.

Unfortunately, the mean temperature and humidity sensors at the 250-m level were found to be even less robust than the wind sensor. The problem was later traced to improper grounding of the cables for this level. Thus, I was again compelled to use the mean sensor data collected at 200 m and 300 m. For the temperature and humidity mean comparisons I included all wind directions. Periods of data were removed when the ATI was incorrectly calibrated for the temperature measurement and when the EG&G dew-point sensors were not operating properly. Scatterplots comparing the mean temperature and humidity measured by the turbulence probes with the corresponding means measured by the mean sensors at the 200-m level are shown in Fig. 5.5. Correlation statistics for the temperature and humidity measurement comparisons are included in Table 5.1.

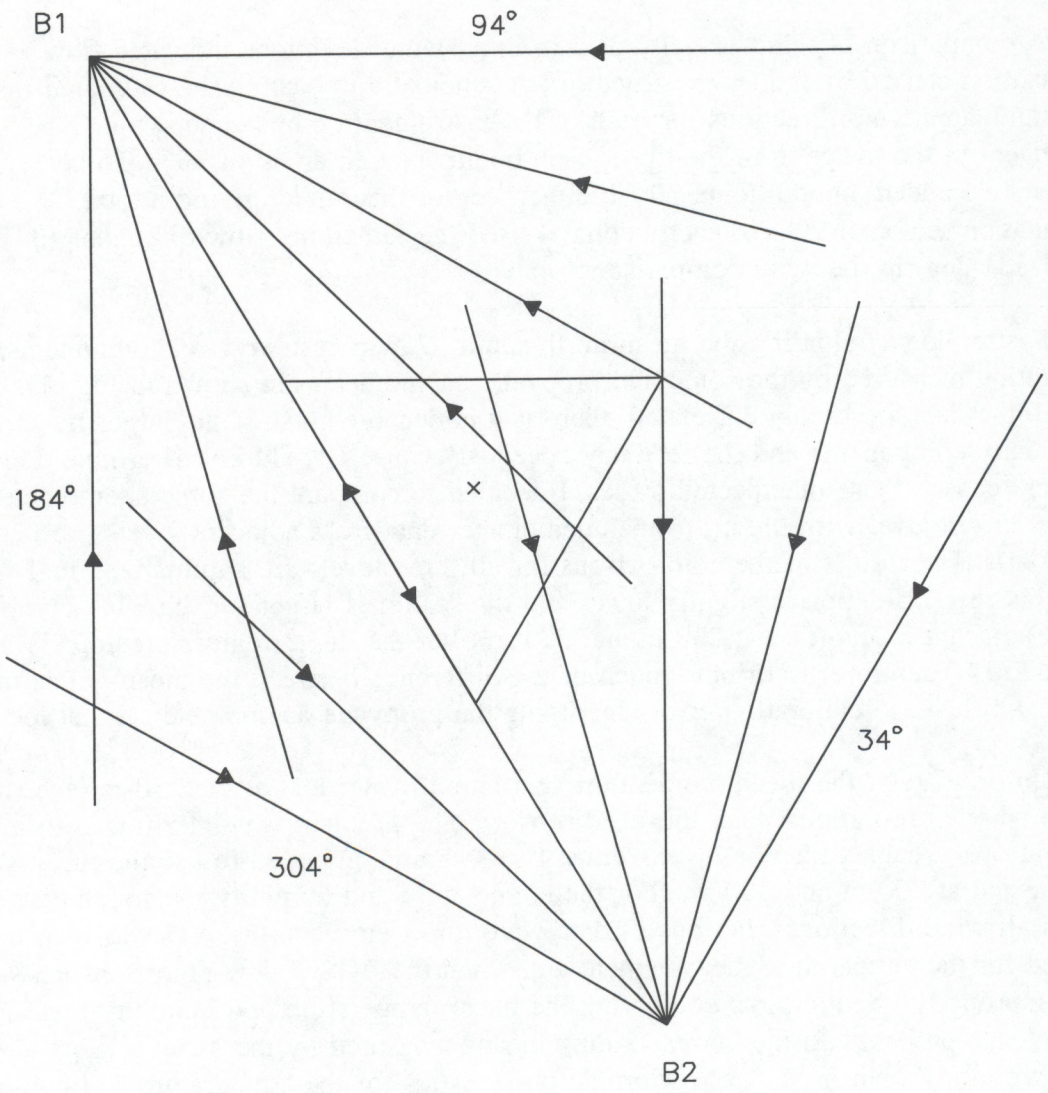

Figure 5.3. Schematic showing the two flow direction sectors that were eliminated from the wind data sets for the comparisons between the mean and turbulence sensors because of the possibility of flow distortion caused by the tower structure.

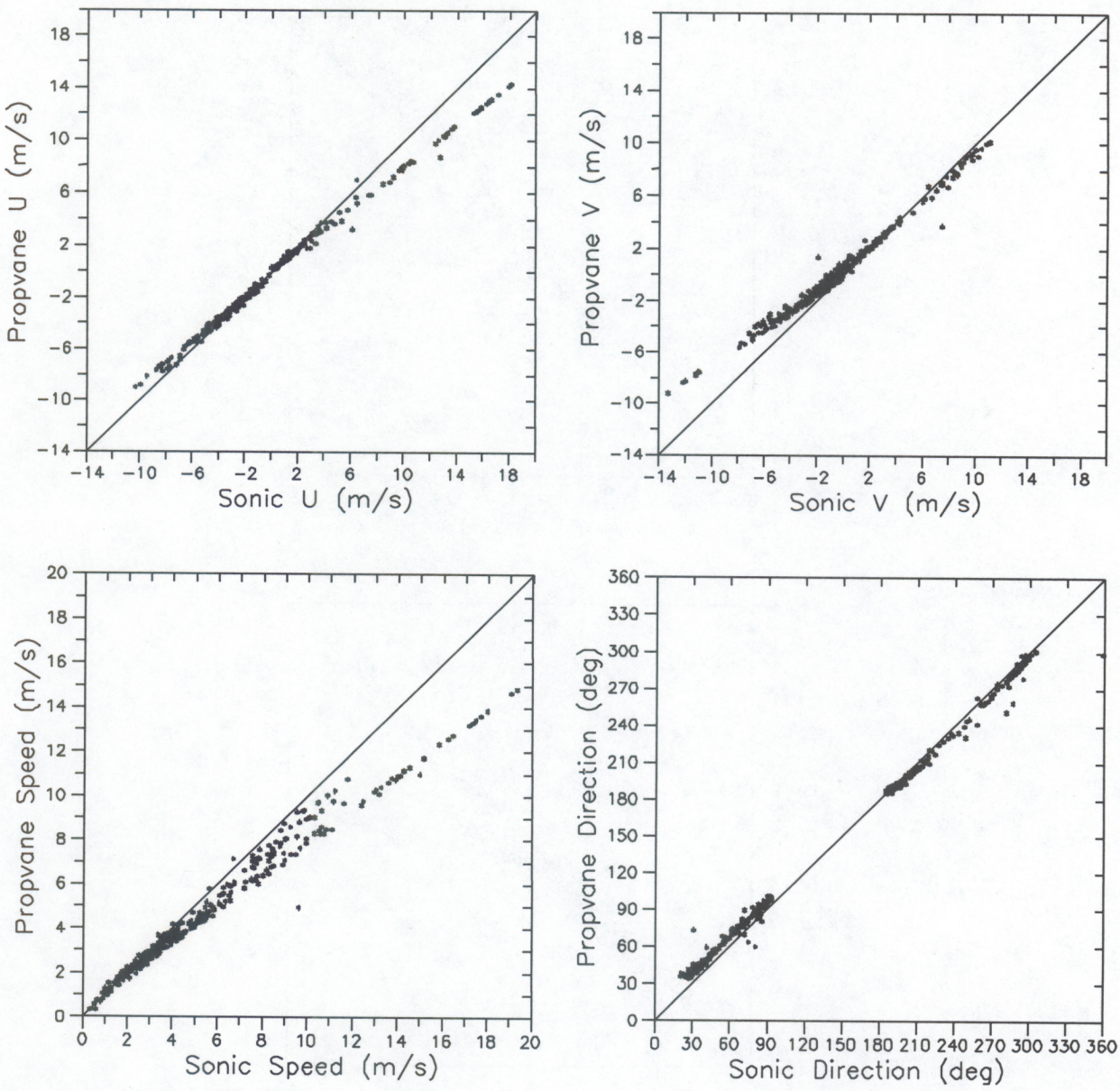

Figure 5.4. Scatterplots comparing the 15-min mean wind components, speed, and direction measured with the sonic and propvane anemometers at the 250-m tower level.

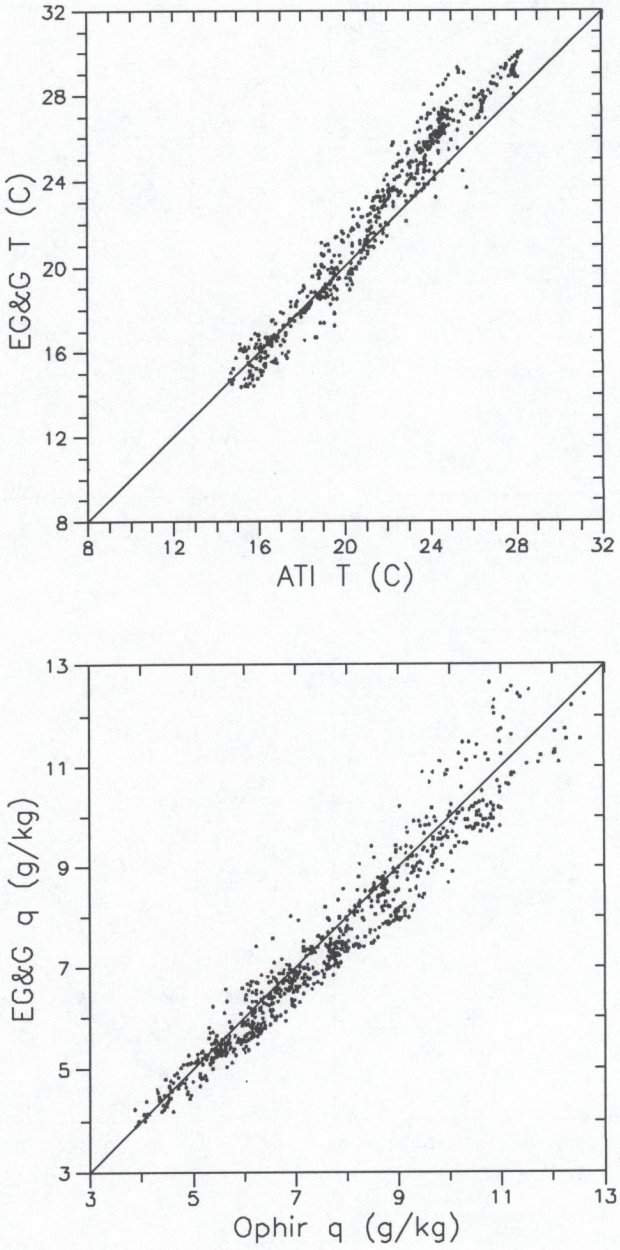

Figure 5.5. Scatterplots comparing the 15-min means of temperature (top) and specific humidity (bottom). For these comparisons, the EG&G temperature and humidity data from the 200-m level are compared to the ATI and Ophir data from the 250-m level.

Table 5.1
Correlation statistics for the turbulence/mean sensor comparisons[†].

	200 m				250 m				300 m			
Variable	N	*E*	*C*	*m*	N	*E*	*C*	*m*	N	*E*	*C*	*m*
U (m s^{-1})	290	1.10	0.96	0.95	337	0.35	0.99	0.84	362	0.79	0.98	1.1
V (m s^{-1})	290	0.97	0.94	0.98	337	0.43	0.98	0.82	362	0.76	0.97	0.96
Speed (m s^{-1})	290	0.74	0.96	0.99	337	0.42	0.98	0.77	362	0.57	0.98	0.95
Direction (∘)	290	13.3	0.98	1.1	337	5.0	0.99	0.93	362	10.0	0.99	0.86
T (C)	604	0.91	0.96	1.2	594	1.1	0.88	0.86	602	0.85	0.96	1.1
q (g kg^{-1})	771	0.45	0.94	0.97	----	----	----	----	1015	0.35	0.95	0.83

[†]The 15-min means measured by the turbulence sensors deployed at the 250-m tower level are compared to the means measured by the mean sensors located at three different tower levels. The four statistics given for each variable at each tower level are the number of observations (N), the standard error of the estimate given by linear regression (E), the correlation (C), and the slope of the regression line (m).

5.1.3 Structure function parameters

I applied Taylor's hypothesis to the frequency spectra measured by the ATI and Ophir in order to calculate the desired velocity and scalar structure function parameters. After applying (2.45) to (2.58), C_x^2 is given by

$$C_x^2 = 4\left(\frac{2\pi}{\overline{u}}\right)^{2/3} S_x(f) f^{5/3}, \tag{5.1}$$

where $\overline{u}$ is the mean horizontal wind measured by the ATI. I examined many spectra to find the frequency range for which the product $fS_x(f)$ most often exhibited the -2/3 power law characteristic of the inertial subrange. I chose to use the median spectral density of the individual spectral bins in this range (0.1-0.5 Hz). Figure 5.6 shows some examples.

I used the temperature and humidity fluctuation data and their corresponding spectra to estimate C_n^2. First, note that it is convenient to use refractivity, N, instead of refractive index, n, where

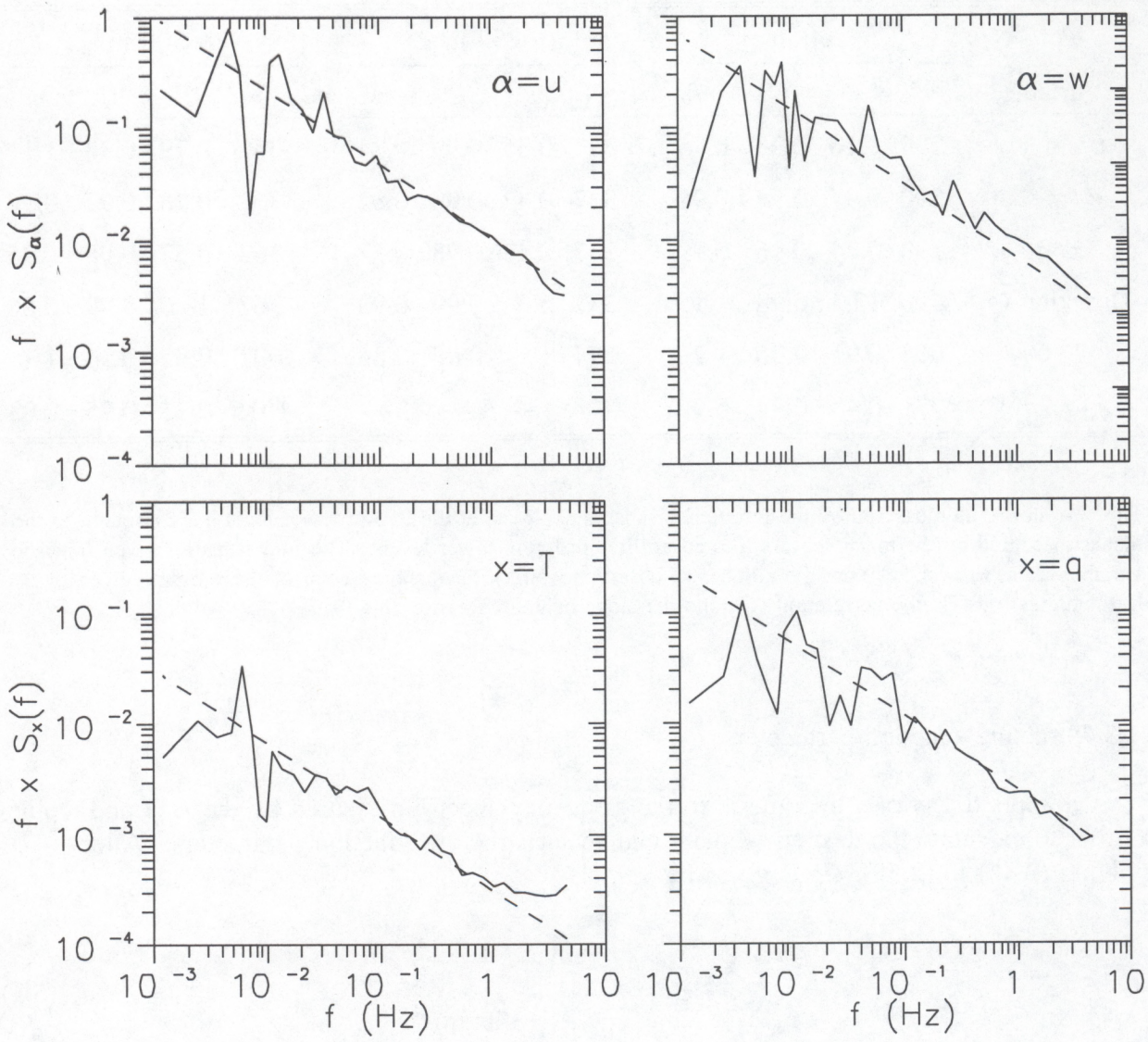

Figure 5.6. Examples of normalized power spectra in the CBL (z/z_i = 0.4) produced from 8192-point (13.6 min) time series measured with the turbulence sensors mounted on the BAO tower. The time series were collected on 16 July 1993 beginning at 17:15:00 GMT. The dashed lines are drawn with a -2/3 slope and pass through the median spectral density in the 0.1 to 0.5 Hz range.

$$N \equiv (n-1) \times 10^6. \tag{5.2}$$

For absolute humidity, Q, in units of g m^{-3} and temperature, T, in K, N is given by

$$N = \frac{77.6P}{T}\left(1 + \frac{7733QR_g}{P}\right), \tag{5.3}$$

where $R_g = 2.87 \times 10^{-3}$ mb m^3 g^{-1} K^{-1} is the gas constant for air and P is the total pressure in millibars. Equation (5.3) follows from Doviak and Zrnić (1984), except that N has been rewritten in terms of absolute humidity, rather than vapor pressure.

I decomposed each of the variables, N, T, Q, and P into a mean, denoted by an overbar, and a fluctuating part, denoted by a prime[5], such that

$$\begin{aligned} N &= \overline{N} + N' \\ T &= \overline{T} + T' \\ Q &= \overline{Q} + Q' \\ P &= \overline{P} + P'. \end{aligned} \tag{5.4}$$

In this analysis, pressure fluctuations can be ignored (Burk, 1980). After substituting (5.4) in (5.3), we arrive at an equation for the fluctuating refractivity:

$$N' = -\left(\frac{77.6P + 1722\overline{Q}}{\overline{T}^2}\right)T' + \left(\frac{1722}{\overline{T}}\right)Q'. \tag{5.5}$$

I used the 10-Hz data and 15-min averages in (5.5) to calculate N' with P = 827 mb. Spectra of N' also were produced using an 8192-point FFT. Equation (5.1) is then used to estimate C_N^2. To convert from C_N^2 to C_n^2, we simply multiply C_N^2 by 10^{-12}. I refer to the tower-deduced values of C_n^2 using this method as $(C_n^2)_T$.

---

[5]The prime is used here instead of lowercase letters (as in Chapter 2) for the fluctuating part to avoid ambiguity with other variable definitions.

Alternatively, I could have used the structure functions for temperature, humidity, and temperature-humidity correlation to estimate C_N^2. The dependence of C_N^2 on C_T^2 and C_Q^2 is found by taking the square of (5.5),

$$C_N^2 = a_T^2 C_T^2 - 2a_T b_Q C_{TQ} + b_Q^2 C_Q^2, \tag{5.6}$$

where

$$a_T = -\frac{(77.6P + 1722\overline{Q})}{\overline{T}^2}, \tag{5.7}$$

and

$$b_Q = \frac{1722}{\overline{T}}. \tag{5.8}$$

However, this method requires that I estimate C_T^2, C_Q^2, and C_{TQ} from the spectral data. I found, in particular, difficulty in estimating C_{TQ}. Because the first method described requires only one structure function, I decided to use this method for the tower C_n^2 calculations. In addition, because using the median spectral density in the range of 0.1 to 0.5 Hz could be a source of error in the $(C_n^2)_T$ data, I visually inspected each individual spectrum to determine the most appropriate value of $S_N(f)$ to use in (5.1).

5.2 Comparison of the Refractive-Index Turbulence Measurements

5.2.1 Data selection

Gaps in the radar and tower time series caused by instrument failures reduced the number of 15-min data pairs available for this analysis. I also applied several different data selection criteria to both the tower and radar data sets, which reduced by 87% the number of data pairs that I chose to use in the analysis. These data selection criteria are explained below.

The decreased length and time scales of nocturnal turbulence, compared to those associated with daytime convective boundary-layer turbulence, violate my crude assumptions of stationarity and homogeneity. For example, a layer of turbulence may be present in part of the radar pulse volume but at the same time be above or below the sensors on the tower. This point is supported by the degradation in correlation that I observed between tower C_n^2 and radar reflectivity at night. Therefore, in this comparison I chose to use only daytime data. Furthermore, I used time-height displays of radar reflectivity to determine the evolution

of the mixed-layer height. This allowed me to select periods when the 250-m level was located well within the convective boundary layer (CBL), where it is more likely that the turbulence fills the radar pulse volume. Also, because of the Rayleigh scattering contribution to radar reflectivity caused by rain, I removed periods of rain prior to the analysis.

I used three other data selection criteria for the tower data. First, because Taylor's hypothesis is not valid for very light wind conditions, I used only those data collected during periods when the mean wind speed exceeded the threshold given by (2.46) of 2.0 m s^{-1}. Second, visual inspection of the refractivity spectra indicated times when an inertial subrange could not be determined with a satisfactory level of confidence. Many of these cases were caused simply by low signal (i.e., weak turbulence). On the other hand, some power spectra with considerable energy were rejected because of excessive high-frequency noise contamination. Third, in addition to its effect on the measured velocity fluctuations, the tower can create temperature fluctuations whenever the wind blows through the tower and the tower is at a different temperature than the air (e.g., when the tower is warmer than the air because of absorption of solar radiation). Likewise, humidity fluctuations can be created by the tower when the tower is wet. The latter is not likely to have occurred during the periods I chose for this analysis. And even though the $(C_n^2)_T$ calculations were dominated by humidity fluctuations much of the time, I decided to remove periods of data when the mean wind direction fell within the flow contamination sector defined in Fig. 5.3 for the turbulence sensor boom.

5.2.2 Radar pulse coding and receiver recovery

I programmed the radar to alternate between sampling with a standard pulse (SP) and a coded pulse (CP). Pulse coding effectively increases the pulse width, resulting in increased average transmitted power, without sacrificing a loss in range resolution. Because the power intensification effect of pulse coding is not fully realized until the fourth range gate, a comparison with and without pulse coding was necessary to calibrate CP radar reflectivities in the lowest three range gates.

An additional factor that affects the signal power in the lowest few range gates of both the SP and CP operating modes is receiver recovery from the blanking pulse. In order for the receiver to be sensitive to the signal amplitudes resulting from atmospheric backscatter (which contain only a small fraction of the transmitted power), a high-gain stage is required at the front end of the receiver. Users of radar data often want to obtain measurements as close to the ground as possible, which means that the shortest possible delay time between transmission and reception should occur. However, the transmitter does not produce a perfectly square pulse in time, and the receiver must be protected from the residual pulse power during a period of recovery after the receiver is switched on. Therefore, a blanking pulse is used to effectively place a ramp on the receiver gain. During this process, the received signals do not acquire their full gain such that, after signal processing, the signal-to-noise ratio (SNR) is reduced. The number of range gates that are affected by the blanking

pulse depends on the delay time between transmission and reception, which ultimately determines the height of the first range gate.

I produced median profiles of radar range-corrected SNR for both the SP and CP modes. The results are shown in Fig. 5.7. From the SP profile, it appears that only the first two range gates are influenced by the blanking pulse. To estimate the effective loss in SNR for these gates, I linearly extrapolated the part of the SP profile between 278 m (gate 3) and 878 m (gate 13) down to 150 m. The difference between the extrapolation and the SP profile results in the receiver recovery loss factors listed in Table 5.2. The same correction factors are applied to the CP profiles because both operating modes used the same delay time.

The remaining difference between the CP profile and the SP profile in the lowest three range gates is caused by incomplete pulse coding. The difference profile of range-corrected SNR for the CP and SP modes is shown in Fig. 5.8. I compared the average difference in range gates 5–20 to the difference in the first three range gates to determine the partial decoding loss factors. The results are listed in Table 5.2. The numbers in parentheses were calculated by Ghebrebrhan (1990) using a mathematical model. Aside from the second range gate, the model and observations agree within 10% (~0.4 dB). The strange result I obtained for the second range gate has been observed by others and is currently being investigated by radar engineers at NOAA. For gate 3, the gate used in the comparisons with the tower, the combined loss in SNR due to receiver recovery and partial decoding is -3.2 dB.

Table 5.2
SNR loss factors for receiver recovery and partial decoding[†].

	SNR Loss Factors	
Gate	Receiver Recovery	Partial Decoding
1	-5.6	-9.6 (-10)
2	-0.6	-4.3 (-7.8)
3	**0.0**	**-3.2** (-3)
4	0.0	+0.4 (0)
5	0.0	-0.3 (0)
6	0.0	-0.2 (0)

[†]Values are in dB. Data highlighted in bold are for the radar range gate used in the calibration. The numbers in parentheses are from Ghebrebrhan (1990).

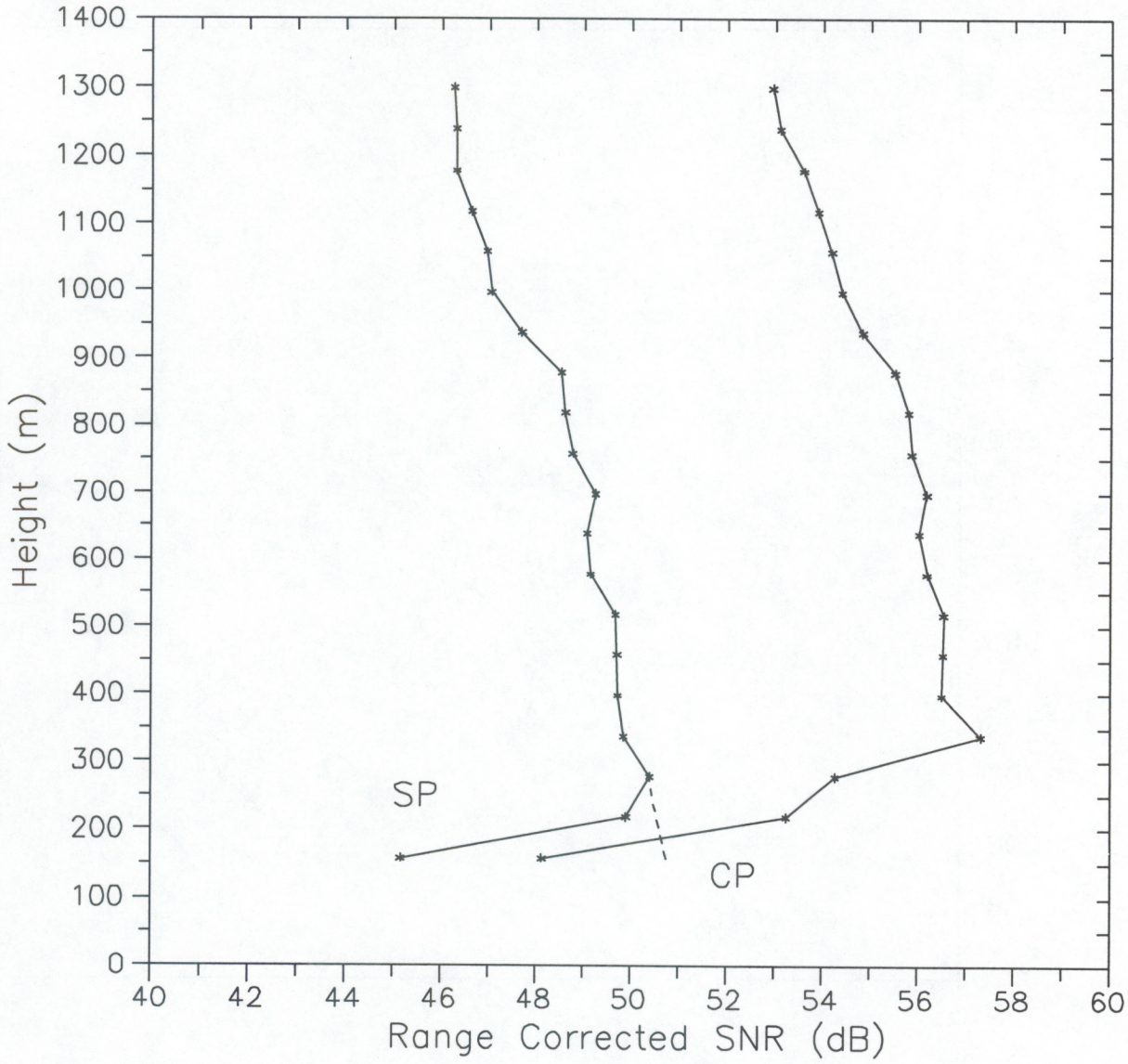

Figure 5.7. Median profiles of SP and CP range-corrected SNR measured with the NBL radar. The dashed line near the bottom of the standard pulse profile shows the extrapolation used to estimate the receiver recovery loss factor.

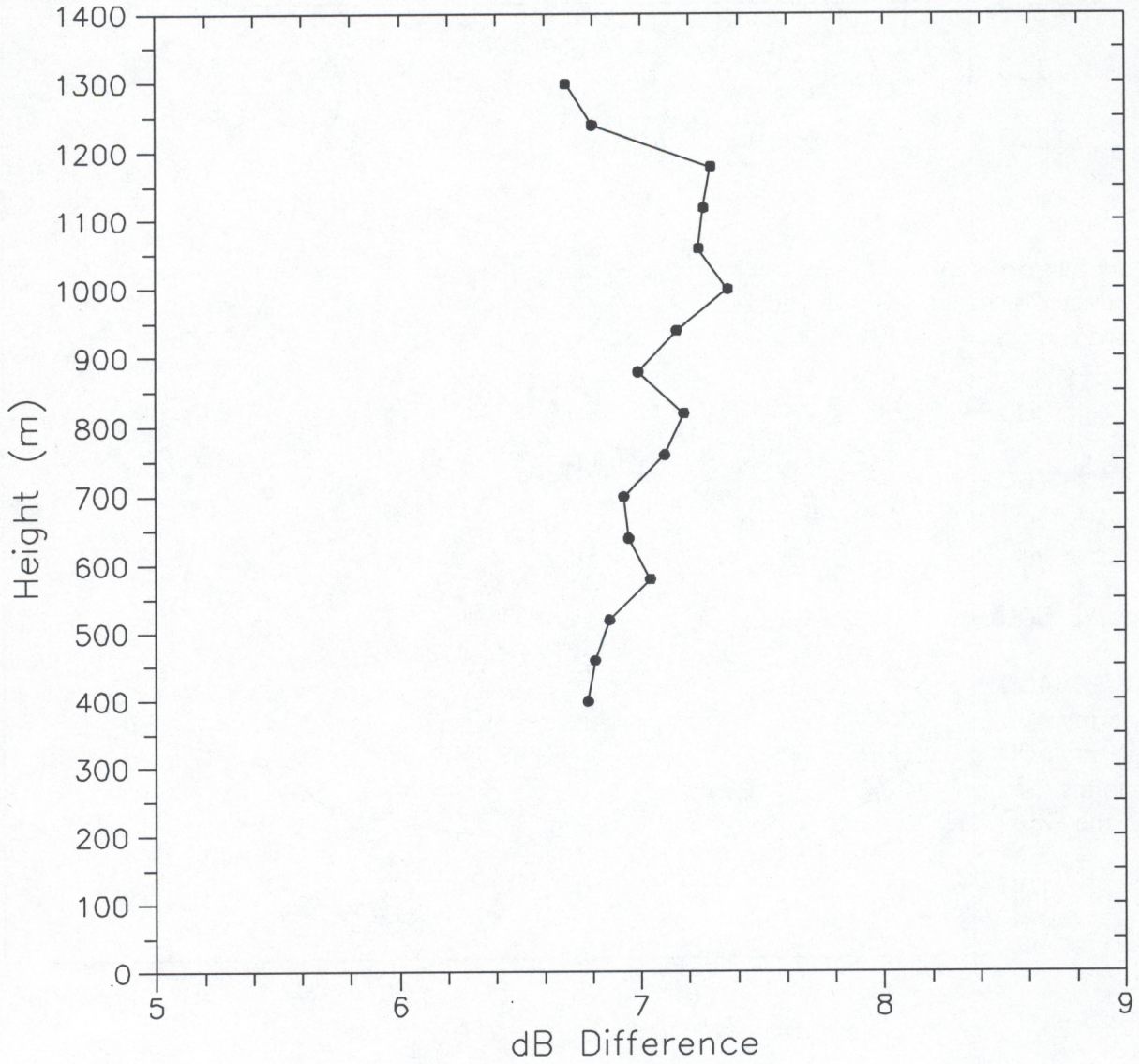

Figure 5.8. Difference profile for range-corrected SNR with the radar alternating between a CP mode and an SP mode.

5.2.3 A radar C_n^2 calibration

Here, I compare the $(C_n^2)_T$ estimates to measured values of radar reflectivity in order to calibrate the radar system efficiency parameter α. I emphasize that this calibration is based on the assumption that the radar and the tower see identical turbulence structure over the horizontal distance separating them, and over the specified averaging period. The radar was located approximately 200 m from the tower. This separation was required to prevent tower echoes from contaminating the radar backscattered signals. The averaging period is defined by the tower, since $(C_n^2)_T$ values were computed from spectra containing an 8192-point time series, which translates to a 14-min averaging period. As mentioned earlier, I was forced to preselect an averaging period because of computational resource limitations. I chose a 14-min averaging period partly to resolve a significant portion of the inertial subrange. I extracted the median from each corresponding 14-min time series of radar reflectivity data. I used a median instead of an average to reduce the impact of outliers.

I estimated the radar calibration constant by substituting $(C_n^2)_T$ for C_n^2 in (4.26):

$$\log_{10}(\alpha^2) = \frac{RCSNR}{10} - \log_{10}(C_n^2)_T + \frac{C_R}{10}, \tag{5.9}$$

where C_R takes the place of all constants and radar operating parameters, RCSNR = R^2SNR, and both C_R and RCSNR are in dB. Using the values given in Table 4.1, C_R = -201.6 dB for the SP mode. For the CP mode, C_R = -206.6 dB (a factor of four is included to account for the increased length of the CP). The appropriate loss factors from Table 5.2 were added to the radar SNR data before using (5.9) to compute α. The results of the calibration are summarized in Table 5.3. A scatterplot comparing C_n^2 from the tower with C_n^2 from the radar in the CP mode is shown in Fig. 5.9.

Table 5.3
NOAA 915-MHz radar system efficiency.

	Coded Pulse	Standard Pulse
Log average	0.25	0.20
Median	0.23	0.19
Linear average	0.27	0.23

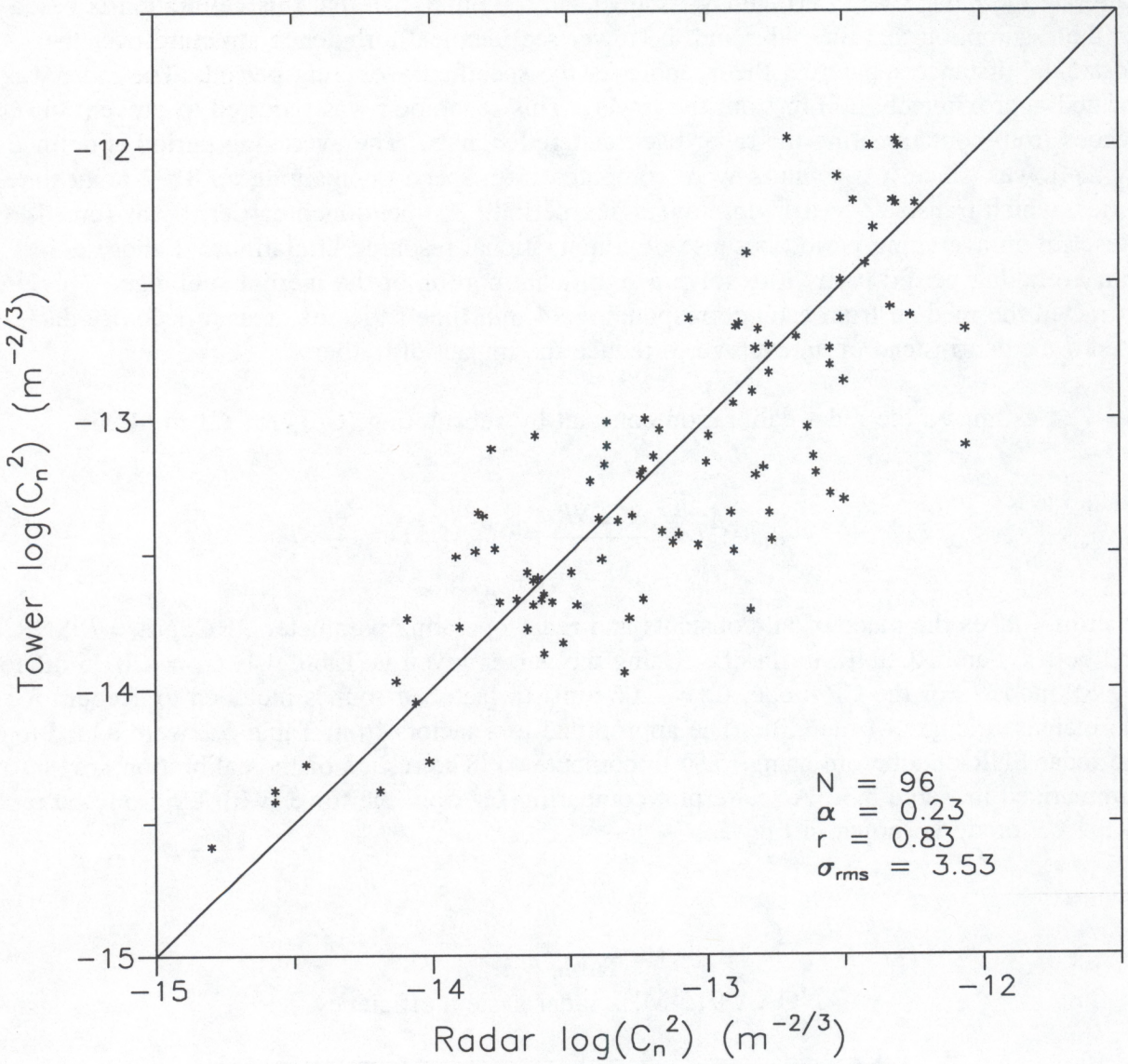

Figure 5.9. Scatterplot comparing C_n^2 measured remotely with the radar and C_n^2 measured in situ on the tower. The measurements were obtained in the CBL using a 14-min averaging period. The number of data points, the radar system efficiency determined from the calibration, the correlation coefficient, and the rms error are shown in the lower right corner.

There is a significant amount of scatter, which is under-emphasized in Fig. 5.9, because the data are plotted on a logarithmic scale covering five orders of magnitude. The scatter may be partially attributable to spatial inhomogeneity as well as to the spatial and temporal sampling differences between the radar and the tower instruments. The implications that these sampling differences have on velocity microturbulence measurements are discussed in Section 5.3. Other errors, including sampling uncertainty, are discussed in the Appendix.

The relative uncertainty of the calibration is determined by calculating the uncertainty in the mean value of α, which is given by $\sigma/\sqrt{N}$ = 0.36 dB. However, according to Fig. 4.8 and Table 4.2, if the tower sensors were located at a different height, so that I was forced to use the radar SNR data from a different range gate, then the mean value of SNR could change by ±0.4 dB. Using (5.9), the corresponding value of α would change by ±0.2 dB. Thus, I estimate the total relative uncertainty in the calibration to be approximately 0.56 dB, or 14%. The absolute uncertainty includes any systematic errors associated with the turbulence sensors on the tower. These errors are discussed in the Appendix.

5.3 Radar Measurement of Velocity Turbulence

5.3.1 The radar averaging filter

Using a time series of vertical velocity measured by the radar to estimate the vertical-velocity variance, σ_w^2, one might expect a priori that the radar sampling would smooth fluctuations on scales shorter than the dwell time and smaller than the pulse volume. Therefore, one would also expect the radar-deduced variance to underestimate the true variance. I examined the degree to which the velocity field is filtered by the radar sampling by forming a spectrum from the radar time series and comparing it to the spectrum measured by the ATI. I used an hour-long time series of radar vertical velocities interpolated onto a 256-point temporal grid to compute the radar spectrum. The time series and resulting spectrum were processed the same way that the ATI data were processed, except that the radar time series was visually inspected to remove a few obvious outliers before computing the spectrum. I produced an hourly averaged ATI spectrum by averaging the four 14-min spectra obtained within the hour. I then interpolated the ATI spectrum to match the frequencies at the low-frequency end of the radar spectrum. Figure 5.10 shows an example.

I found 50 hours of CBL data for which I judged the ATI spectra to be of high quality. The average vertical-velocity spectra measured by the radar and ATI is shown in Fig. 5.11. The ratio of radar spectral density to ATI spectral density as a function of frequency is also shown in Fig. 5.11. Here, one can see that at the lower frequencies (less than 0.01 Hz) the radar measures nearly the same spectral density on average as the ATI measures. However, as frequency increases, the ratio drops off. The attenuation of radar spectral density results from the averaging imposed by the radar sampling.

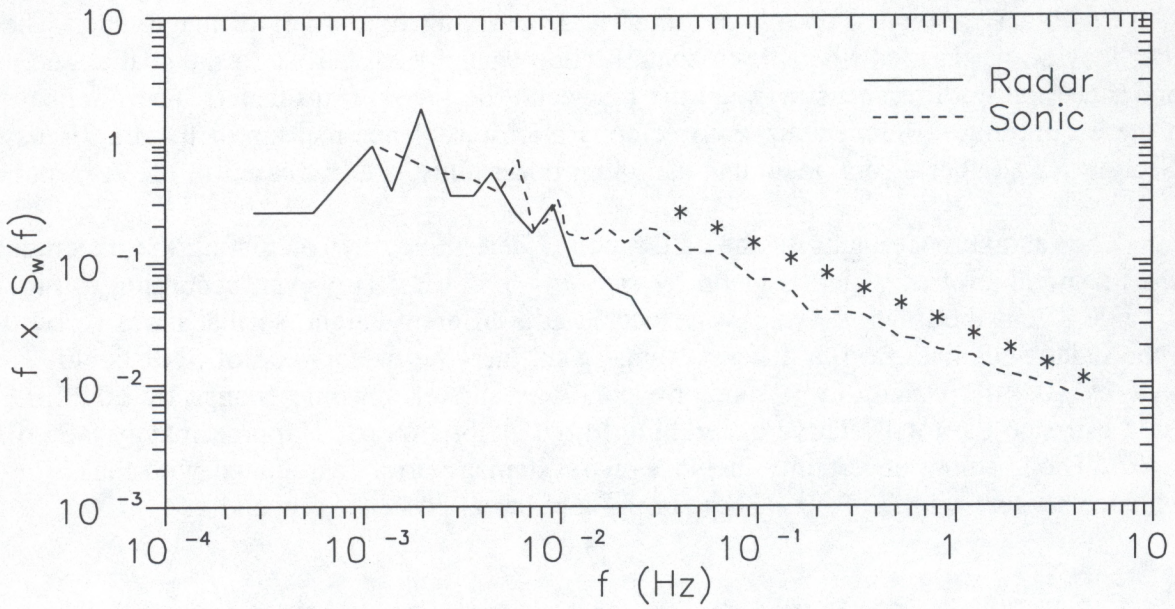

Figure 5.10. An example of the normalized vertical velocity power spectra deduced from time series measured concurrently with the radar and ATI. A line of -2/3 slope indicated by the asterisks is shown for comparison. The radar spectrum was computed from a 1-hr time series of vertical velocity, whereas the ATI spectrum was computed by averaging the four 14-min spectra obtained within the hour. The measurements were taken in the CBL (z/z_i = 0.2) on 15 July 1993 beginning at 21:00 GMT.

I first evaluated the filtering effects of the dwell time and the pulse volume independently using mathematical models found in the literature. The process of averaging the radar signals over the dwell time is analogous to estimating the power spectrum of a discrete time series of finite length, a problem that was addressed by Kristensen (1971). Discrete sampling results in aliasing, which allows energy at frequencies larger than the Nyquist frequency to leak back into the resolved spectrum. As shown by Kristensen (1971) and stated in Section 4.2.2, averaging acts as a low-pass filter on the signal, thereby diminishing the effects of aliasing.

Following the notation of Kristensen (1971), the filtered and aliased spectral estimate, $G(\omega_k)$, is given by

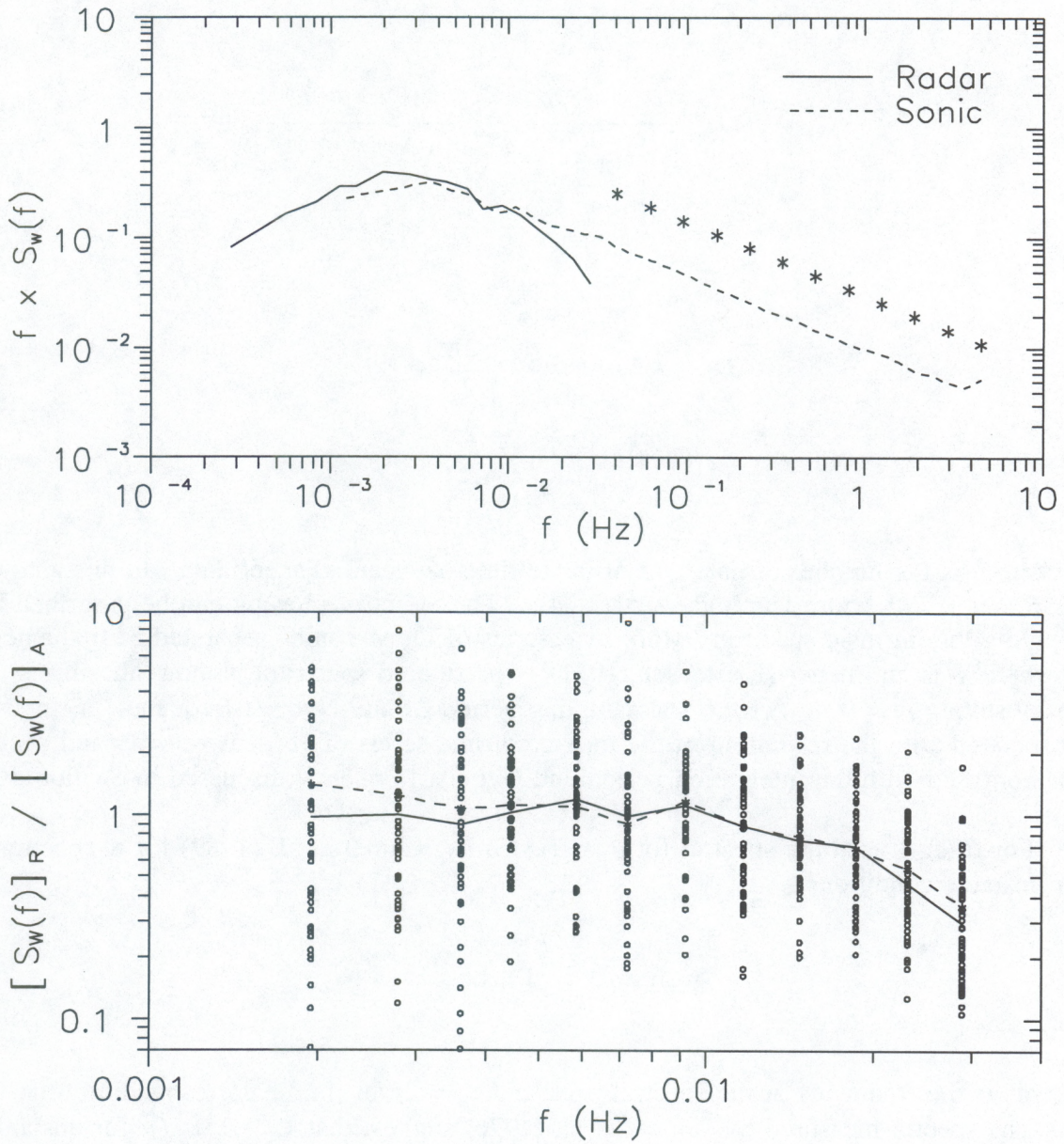

Figure 5.11. A statistical comparison of the vertical-velocity spectra measured concurrently with the radar and ATI. The top panel shows the average spectra calculated from 50 hours of CBL data. A line of -2/3 slope is indicated by the asterisks. The circles in the bottom panel show the ratio (radar to ATI) of spectral density for each of the 50 individual spectra. The solid curve is drawn through the median ratio occurring at each discrete frequency. The dashed curve gives the ratio between the average spectra. Both curves illustrate the combined filtering effects of pulse-volume and dwell-time averaging.

$$G(\omega_k) = \frac{\sin^2\left(\frac{\pi}{2}\frac{\omega_k}{\omega_N}\right)}{\left(\frac{\pi}{2\omega_N}\right)^2} \sum_{m=-\infty}^{\infty} \frac{\phi(\omega_k + m\omega_s)}{(\omega_k + m\omega_s)^2}, \tag{5.10}$$

where

$$\omega_k = k\Delta\omega \quad \Delta\omega = \frac{2\pi}{T_o}$$
$$T_o = n\Delta t \quad \omega_s = \frac{2\pi}{\Delta t} = 2\omega_N, \tag{5.11}$$

and where n is the number of data and Δt is the time between adjacent data. In this analysis, $n = 256$ and $T_o = 1$ hour, which gives $\Delta t = 14$ s. The effect of aliasing can be described by multiplying the intrinsic spectrum, $\phi(\omega)$, by a series of Dirac combs separated in frequency by $m\omega_s$, where m is an integer (Kristensen, 1971). The filtered spectrum without aliasing is given by setting $m = 0$ in (5.10). The sampling period Δt and Nyquist frequency ω_N in (5.11) are associated with the resolution of the measured time series of vertical velocity and should not be confused with the integration period and Nyquist frequency discussed in Section 4.2.2.

For $\phi(\omega)$, I used the spectral form suggested by Kaimal et al. (1989) for w spectra under unstable conditions:

$$\phi(\omega) = \sigma^2\tau_m\left(1 + 1.5\frac{\omega}{\omega_m}\right)^{-5/3}, \tag{5.12}$$

where ω_m is the frequency at the spectral peak and $\tau_m = 2\pi/\omega_m$ is the corresponding time scale. The spectra measured by Kaimal et al. (1976) suggest that $\tau_m \approx 1.0 z_i / \overline{u}$ for unstable conditions. The average wind speed recorded by the ATI for the 50 hours of data was 4.1 m s^{-1}, and the average z_i estimated from the SNR profiles measured by the radar was 1400 m, so $\tau_m \approx 6$ min. The function $G(\omega)$ was evaluated numerically over the interval $0 \le \omega/\omega_N \le 1$.

The ratio of G to ϕ is defined by Kristensen (1971) as the pseudo transfer function (i.e., it is not a true transfer function, because it depends on the choice of ϕ). I adopt the notation of Kaimal et al. (1989) and denote the transfer function by

$$K_T(\omega) = \frac{G(\omega)}{\phi(\omega)}, \tag{5.13}$$

where the subscript "T" is used to identify the transfer function resulting from averaging over the radar dwell time. I evaluated this function with and without the effect of aliasing, and the results are shown in Fig 5.12.

I now focus on the filtering associated with the pulse volume. This problem has been addressed by Srivastava and Atlas (1972), Frisch and Clifford (1974), and Gossard and Strauch (1983). If x_1 is the direction along the radar beam and x_2 is the direction perpendicular to x_1 and along the direction of the mean wind, then at a fixed height, the radar measures the transverse spectrum of vertical velocity

$$S_w(k_2) = \frac{1}{4}\int\int_{-\infty}^{\infty} \Phi_{11}(\mathbf{k})\Phi_P(\mathbf{k})\,dk_1\,dk_3, \tag{5.14}$$

where

$$\Phi_P(\mathbf{k}) = (2\pi)^6 |F_P(\mathbf{k})|^2 \tag{5.15}$$

is the beam filter function associated with the pulse volume, and $F_P(\mathbf{k})$ is the Fourier transform of $A(\mathbf{r})$, the two-way beam illumination function (Srivastava and Atlas, 1972). Frisch and Clifford (1974) and Gossard and Strauch (1983) used Gaussian functions to describe the pulse length and horizontal beam cross section. If a circular cross section is assumed, then

$$|F_P(\mathbf{k})|^2 = \frac{1}{(2\pi)^6} \exp[-k_1^2 b^2 - a^2(k_2^2 + k_3^2)]. \tag{5.16}$$

The Gaussian beam half-width, a, and pulse half-length, b, are given by Gossard et al. (1990):

$$a = \frac{R\theta_h}{\sqrt{2\ln 2}} \qquad b = 0.3\Delta R, \tag{5.17}$$

where R = 278 m is the height at the center of the range gate used in this study, and θ_h is the angular half-width of the antenna beam in radians.

If the turbulence is isotropic, then the functional form for $\Phi_{11}(\mathbf{k})$ is given by (2.32). We also know from (2.26) and (2.47) that $E(k) = A_E\varepsilon^{2/3}k^{-5/3}$. The value of A_E is approximately

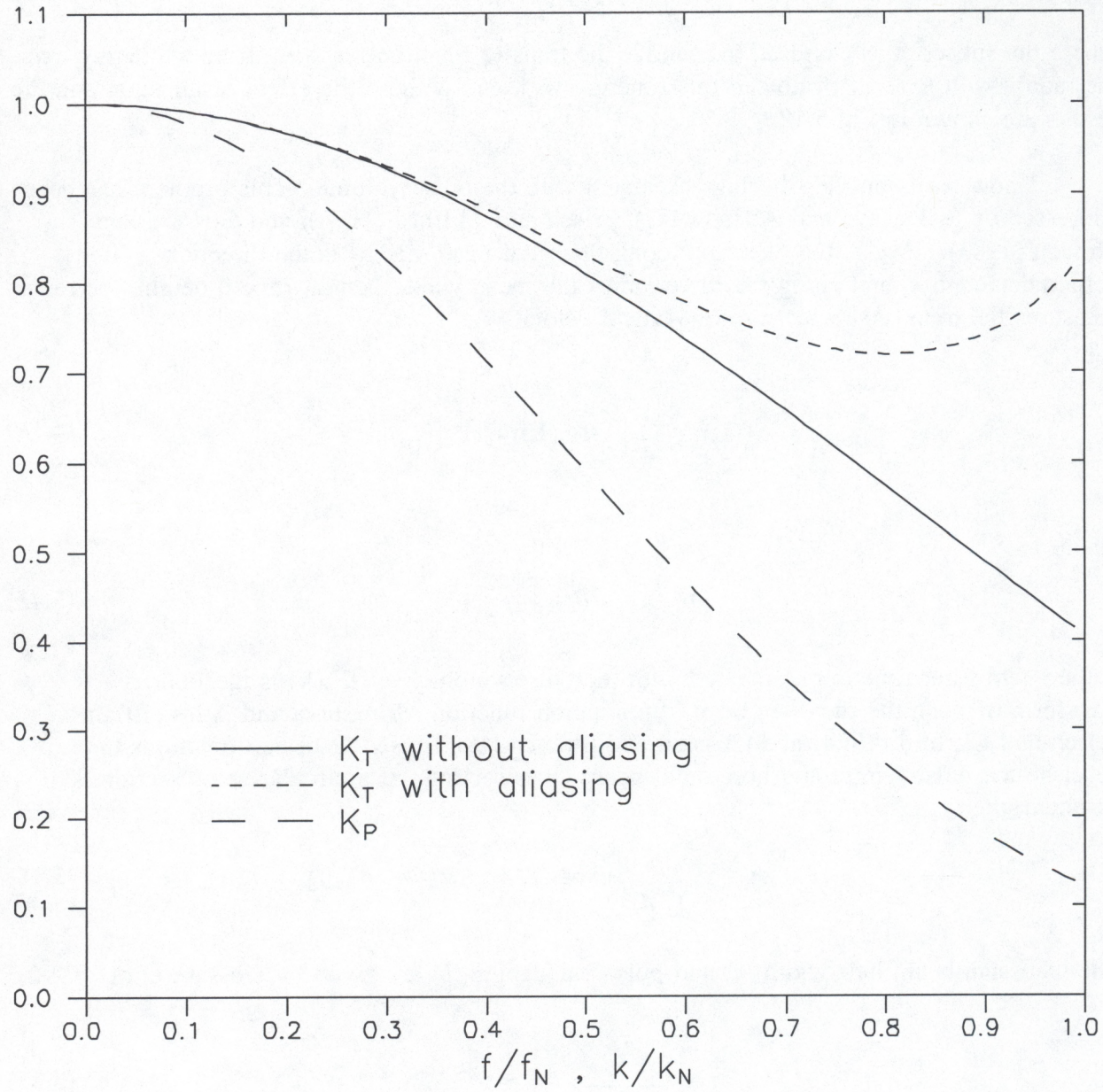

Figure 5.12. The theoretical transfer functions for dwell-time averaging (K_T) and pulse-volume averaging (K_P) treated separately and plotted as a function of the frequency (or wavenumber) normalized by the Nyquist value. The dwell-time transfer function is shown with and without the effects of spectral aliasing.

1.6 (Gossard et al., 1990). Using (2.20) and (2.32), we have for the isotropic one-dimensional lateral spectrum:

$$\phi_{11}(k_2) = \frac{1}{4}\int_{-\infty}^{\infty}\int \Phi_{11}(\mathbf{k})\,dk_1\,dk_3 = \frac{A_E\varepsilon^{2/3}}{2\pi}\int_{-\infty}^{\infty}\int k^{-11/3}\left(1-\frac{k_1^2}{k^2}\right)dk_1\,dk_3. \qquad \textbf{(5.18)}$$

The filtered spectrum measured by the radar is then given by

$$S_w(k_2) = \frac{A_E\varepsilon^{2/3}}{2\pi}\exp(-a^2k_2^2)\int_{-\infty}^{\infty}\int k^{-11/3}\left(1-\frac{k_1^2}{k^2}\right)\exp(-b^2k_1^2-a^2k_3^2)\,dk_1\,dk_3. \qquad \textbf{(5.19)}$$

The transfer function for pulse volume averaging, K_P, is found by taking the ratio of (5.19) to (5.18). Using k for k_2, we have

$$K_P(k) = \frac{S_w(k)}{\phi_{11}(k)}. \qquad \textbf{(5.20)}$$

The function K_P is also plotted in Fig. 5.12 as a function of the ratio k/k_N, where k_N is the wavenumber corresponding to ω_N. For the given measurement height and average wind speed, the radar pulse volume filters more of the turbulence than the radar dwell time.

The overall transfer function for the radar is found by combining the contributions from dwell-time averaging and pulse-volume averaging in a multiplicative manner. The result is shown in Fig. 5.13, along with the transfer function determined from the radar and ATI observations (see Fig. 5.11). The radar sampling results in less aliasing than is predicted by the model.

However, we must remember that the estimation of the radar moments is a noisy process. For example, in Fig. 4.2 only a small region of the velocity spectrum near the peak could be identified because the rest of the spectrum was imbedded in noise. Noise is associated with the velocity estimate because the first moment is weighted by the value of the spectrum (i.e., signal plus noise) at each frequency point within the signal interval. It is unclear exactly what effect this type of sampling uncertainty has on the spectrum produced from a time series of radar velocity estimates. However, if the energy that is aliased because of finite sampling is mostly uncorrelated, then we would not expect to see a strong functional dependence on frequency in the aliased spectrum.

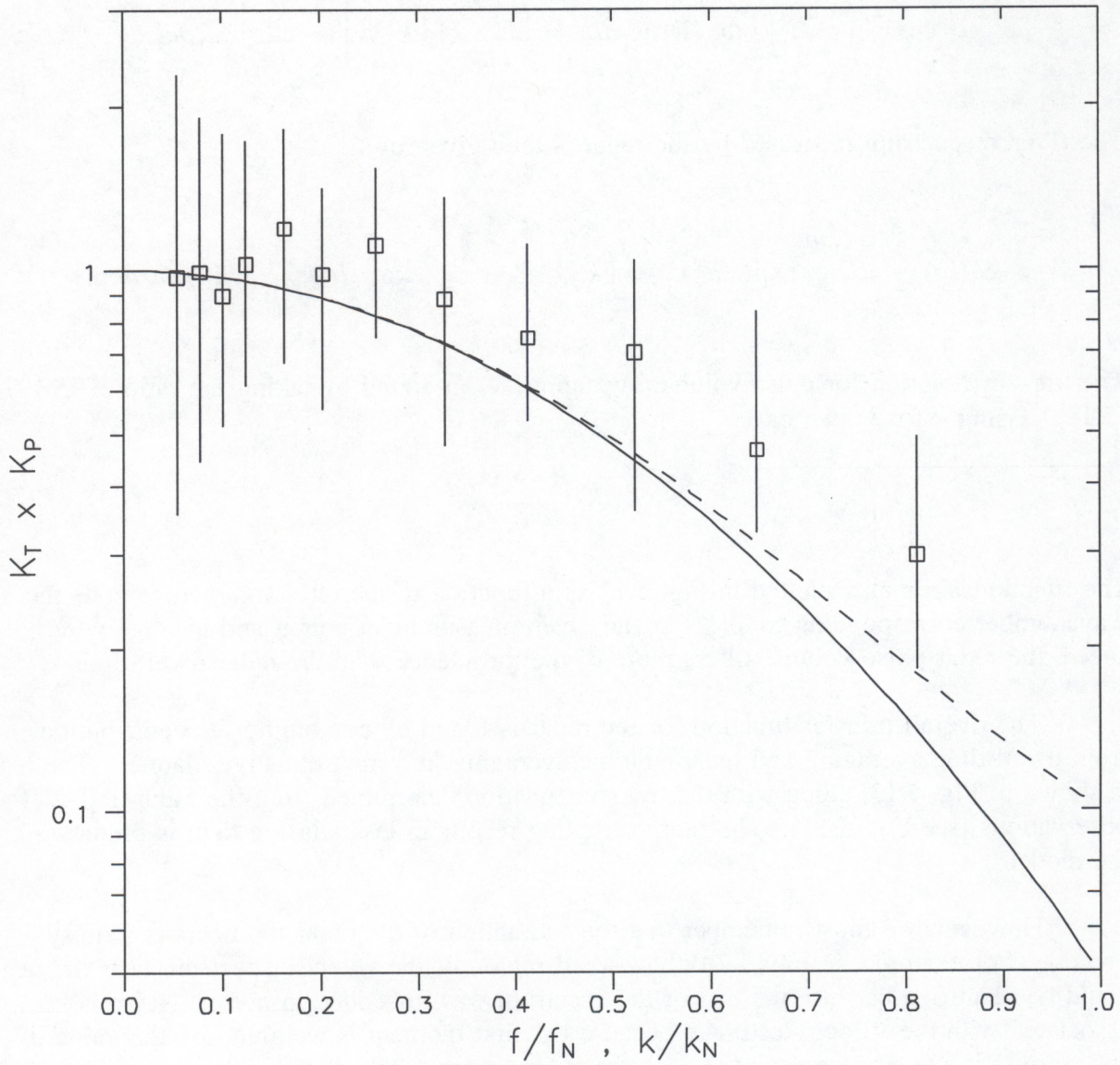

Figure 5.13. The radar transfer function calculated with (dashed curve) and without (solid curve) spectral aliasing, along with the median transfer function from Fig. 5.11 that was determined by comparing the power spectra from the radar and ATI (open squares). The error bars include the second and third quartiles of the distributions shown in Fig. 5.11.

5.3.2 Spectral width estimation of C_u^2

Gorelick and Mel'nichuk (1963, 1968) were among the first to recognize that the turbulent kinetic energy (TKE) present in scales smaller than the pulse volume appeared in the variance of the Doppler spectrum. Unfortunately, several other factors can contribute to the spectral width (Gossard, 1990). For clear air, the total broadening of the spectrum, σ_t^2, is approximately given by

$$\sigma_t^2 = \sigma_s^2 + \sigma_a^2 + \sigma_{11}^2, \tag{5.21}$$

where σ_s^2 is the contribution due to wind shear in both the transverse and radial directions, σ_a^2 is the contribution due to antenna properties, and σ_{11}^2 is the variance of the velocity component in the radial direction due to turbulence. Two antenna effects broaden the spectrum. If the antenna rotates, the spectrum is broadened by the antenna motion. For non-rotating antennas, σ_a^2 reduces to the effect of a finite width beam which is often referred to as beam broadening. To demonstrate this effect, consider a horizontal wind blowing through a vertically pointed beam. Even in a uniform wind, the radial direction sensed by the radar varies over the width of the beam so that a range of velocities is measured. For example, it is easy to show that the radial velocities sensed by the leading and trailing edges of the beam are opposite (i.e., toward and away from the radar).

Gossard (1990) gives parameterizations to correct for the shear and beam broadening effects. I evaluated these functions for the NBL radar and found that given its relatively wide beam (see Table 4.1), $\sigma_a^2 >> \sigma_s^2$, so beam broadening dominates shear broadening. The beam broadening is given by Gossard (1990):

$$\sigma_a^2 = \frac{V_T^2 \theta_h^2}{2.76}, \tag{5.22}$$

where V_T is the wind speed transverse to the radar beam. Assuming successful removal of the contamination, the spectral width that remains is equivalent to twice the standard deviation of radial velocity fluctuations that are associated with eddies smaller than the radar pulse volume. As shown in Section 5.3.1, the dwell time should also be accounted for in the broadening of the spectrum. However, we should treat these two filtering processes together, since they occur simultaneously during the radar measurement.

Following the notation of Gossard et al. (1990), the spatially averaged velocity measured by the radar can be written as

$$\overline{w} = \frac{1}{V}\iiint A(\mathbf{r})\, w(\mathbf{r})\, d\mathbf{r}, \tag{5.23}$$

where $\mathbf{r}$ is a point of measurement along the beam. If we generalize to include time

dependence, then

$$\overline{w(t)} = \frac{1}{V}\iiint A(\mathbf{r})\, w(\mathbf{r},t)\, d\mathbf{r}. \tag{5.24}$$

The Fourier transform of $w(\mathbf{r},t)$ is given by

$$w(\mathbf{r},t) = \iiint dW(\mathbf{k})\, e^{i\mathbf{k}\cdot(\mathbf{r}-\mathbf{v}t)}\, d\mathbf{k}, \tag{5.25}$$

where the spectral form of Taylor's hypothesis has been used, i.e., $\omega = \mathbf{k}\cdot\mathbf{v}$ is the angular frequency induced by wavenumber $\mathbf{k}$. Inserting (5.25) in (5.24) and rearranging terms gives us

$$\overline{w(t)} = \iiint dW(\mathbf{k})\, d\mathbf{k}\left[\frac{1}{V}\iiint A(\mathbf{r})\, e^{i\mathbf{k}\cdot\mathbf{r}}\, d\mathbf{r}\right] e^{-i\mathbf{k}\cdot\mathbf{v}t}. \tag{5.26}$$

The term enclosed in brackets is the beam filter function $F_P(\mathbf{k})$. Dwell-time effects are included by averaging $\overline{w(t)}$ over the dwell time. The temporally and spatially averaged vertical velocity measured by the radar is thus given by

$$w_a = \int_{-T/2}^{T/2} \overline{w(t)}\, dt = \iiint dW(\mathbf{k})\, F_P(\mathbf{k})\, d\mathbf{k} \int_{-T/2}^{T/2} e^{-i\mathbf{k}\cdot\mathbf{v}t}\, dt. \tag{5.27}$$

More generally,

$$w_a = \iiint dW(\mathbf{k})\, F_P(\mathbf{k})\, F_T(\mathbf{k})\, d\mathbf{k}, \tag{5.28}$$

where

$$F_T(\mathbf{k}) = \int_{-\infty}^{\infty} T(t)\, e^{-i\mathbf{k}\cdot\mathbf{v}t}\, dt \tag{5.29}$$

is the Fourier transform of the dwell-time window function, $T(t)$. I assume that the process of averaging over the dwell time can be represented by a rectangular window function. Then, in Fourier space, $F_T(\mathbf{k})$ is given by

$$F_T(\mathbf{k}) = \frac{\sin(k_2 L/2)}{k_2 L/2}, \tag{5.30}$$

where $L = V_T t_D$.

Ultimately, I am interested in the spectral broadening due to turbulence. This can be expressed in terms of the corresponding point-measured and space- and time-averaged variances (Frisch and Clifford, 1974):

$$\sigma_{11}^2 = \sigma_{\text{point}}^2 - \sigma_{w_a}^2. \tag{5.31}$$

The first term on the right side can be determined by integrating the spectrum given by (5.18). For the second term I must first modify (5.19) to include the dwell-time averaging function before integrating. The end result is given by

$$\frac{4\pi\sigma_{11}^2}{A_E\varepsilon^{2/3}} = \int_{-\infty}^{\infty}\int\int k^{-11/3}\left[1-\left(\frac{k_1}{k}\right)^2\right]\left[1-\frac{\sin^2(k_2L/2)}{(k_2L/2)^2}\,e^{-b^2k_1^2-a^2(k_2^2+k_3^2)}\right]dk_1\,dk_2\,dk_3. \tag{5.32}$$

Gossard et al. (1990) took a different approach. They treated the spatial and temporal averaging processes separately. The pulse volume averaging contribution was found by evaluating (5.32) without the sine term. An analytical solution to this integral was found by Frisch and Clifford (1974) and Labbitt (1981). The pulse volume contribution denoted by Gossard et al. (1990) as σ_{Vw}^2, is given by

$$\sigma_{Vw}^2 = \frac{3}{2}A_E(\delta\varepsilon)^{2/3}\Gamma(5/3)\gamma^2, \tag{5.33}$$

where for $b \le a$

$$\delta = a$$

$$h = 1-\left(\frac{b}{a}\right)^2$$

$$\gamma^2 = 1-\frac{h}{15}-\frac{h^2}{105}-\ldots$$

and for $b > a$

$$\delta = b$$

$$h = 1 - \left(\frac{a}{b}\right)^2$$

$$\gamma^2 = 1 - \frac{4h}{15} - \frac{8h^2}{105} - \ldots$$

Gossard et al. (1990) approximated the time averaging contribution by

$$\sigma_T^2 = \int_{k_0}^{k_c} E(k)dk, \tag{5.34}$$

where $k_0 = 2\pi/(V_T t_D)$ and $k_c = 2\pi/\delta$. After integrating (5.35), they obtained

$$\sigma_T^2 = \frac{3}{2} A_E \left(\frac{\varepsilon}{2\pi}\right)^{2/3} [(V_T t_D)^{2/3} - \delta^{2/3}]. \tag{5.35}$$

Combining (5.33) and (5.35) gives

$$\frac{4\pi\sigma_{11}^2}{A_E \varepsilon^{2/3}} = 6\pi\delta^{2/3}\left\{\Gamma(5/3)\gamma^2 + (2\pi)^{-2/3}\left[\left(\frac{V_T t_D}{\delta}\right)^{2/3} - 1\right]\right\}. \tag{5.36}$$

Gossard et al. (1990) ignored the right-hand term in braces unless $V_T t_D > \delta$. I find two problems with this result. First, the proper dimension with which to compare $V_T t_D$ is 2δ, since δ is based on the half-dimensions of the pulse volume. Second, with a non-zero wind speed, beam broadening should occur with any amount of time averaging, not just after L exceeds (2)δ. If I remove the right-hand term in brackets from (5.36), replace δ with 2δ (Dr. Gossard has agreed to these changes in principle), and insert the proper pulse volume dimensions for the NBL radar, then (5.36) may be rewritten as

$$\frac{4\pi\sigma_{11}^2}{A_E \varepsilon^{2/3}} = 128.3 + 3.5(V_T t_D)^{2/3}. \tag{5.37}$$

Figure 5.14 compares the space- and time-filtered variance functions described by (5.32) and (5.37). The triple integral in (5.32) was evaluated numerically for selected values of L. The solid curve drawn in Fig. 5.14 represents a fourth-order polynomial fit to the

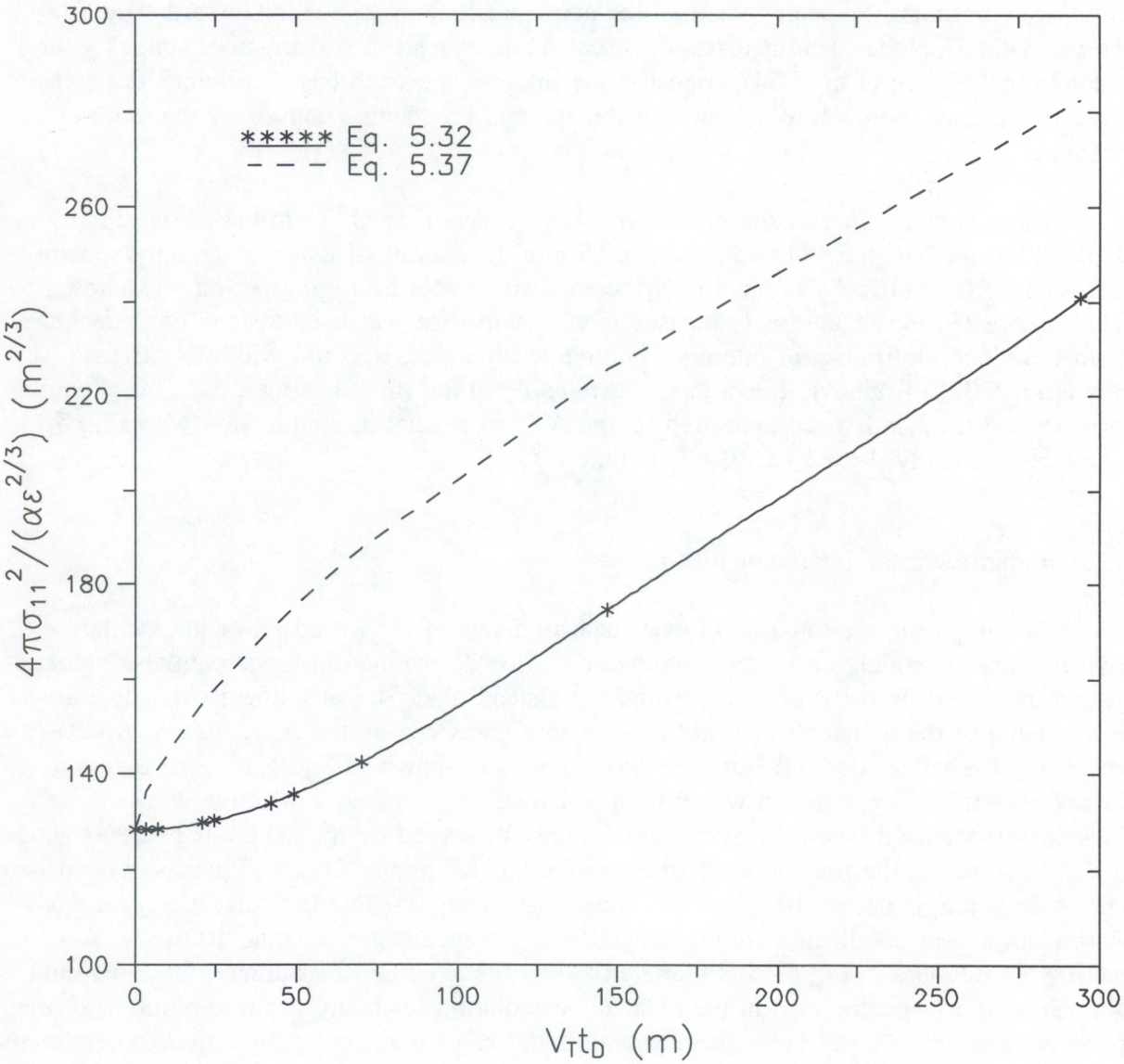

Figure 5.14. Two different velocity variance filter functions for the effects of pulse volume and dwell-time averaging on radar measurements of spectral width. The separation between the two curves is due to the different approaches used to calculate the dwell-time contribution (see text).

results of the integrations. The intersection of the curves with the y-axis gives the pulse volume averaging contribution to the variance. The two curves behave differently for low wind speeds. The primary difference between the two techniques is that the integral approach includes a continuum of scales for the time average filter, whereas the Gossard et al. (1990) approximation includes a limited range of scales represented in wavenumber space by the bounds for the integral in (5.34). Because the integral approach has no obvious deficiencies, I chose to use this approach to account for the spectral broadening caused by the radar sampling.

I can now summarize the procedure I used to estimate C_u^2 from the radar. First I obtained the median spectral width from a 15-min time series of Doppler velocity spectra measured by the vertically pointed radar beam. An 15-min averaging period was chosen to match the resolution of the tower measurement. A median was used instead of an average again to reduce the impact of outliers. I converted the radar spectral width to variance. I then used (5.22) to remove the variance attributable to the finite beamwidth. The remaining variance and the wind speed measured by the ATI were used in conjunction with Fig. 5.14 to calculate ε. Finally, I used (2.59) to compute C_u^2.

5.3.3 Radar/tower C_u^2 intercomparison

In comparing the radar and tower measurements of C_u^2 I used all of the available daytime data for which an inertial subrange could be determined in the streamwise velocity spectra measured by the ATI. I compared C_u^2 instead of C_w^2 because there was generally better signal in the u-spectra than in the w-spectra measured by the ATI. A scatterplot comparing the values derived from the two methods is shown in Fig. 5.15. All data are shown, except for two cases in which the radar method produced a negative value of C_u^2. These cases occurred when the horizontal velocity measured by the ATI was greater than 14 m s^{-1}. In addition, the four points farthest above the 1:1 line in Fig. 5.15 are associated with wind speeds ranging from 10-15 m s^{-1}. These results suggest that the corrections for finite beamwidth and/or dwell time are too severe for wind speeds greater than 10 m s^{-1}. A majority of the data in Fig 5.15 is scattered below the 1:1 line. I examined the individual Doppler velocity spectra used in the radar C_u^2 calculation for many of these points and often found enough erroneously large spectral widths in the 15-min averaging period to contaminate the median.

Figure 5.16 shows the scatterplot that results when the eight worst outliers in Fig. 5.15 (four from each side of the 1:1 line, which together account for only 6% of the data) are removed. A discussion of the uncertainties associated with the C_u^2 calculations is given in the Appendix. The correlation statistics shown in Fig. 5.16 are comparable to those obtained in a comparison of the vertical-velocity variances measured by a sodar and a sonic anemometer in unstable conditions (Gaynor and Kristensen, 1986). Curiously, the scatter increased when they applied a pulse volume filtering correction to the sodar measurements. Gossard et al. (1984) compared C_w^2 measured by sonic anemometers mounted on the BAO tower with radar-

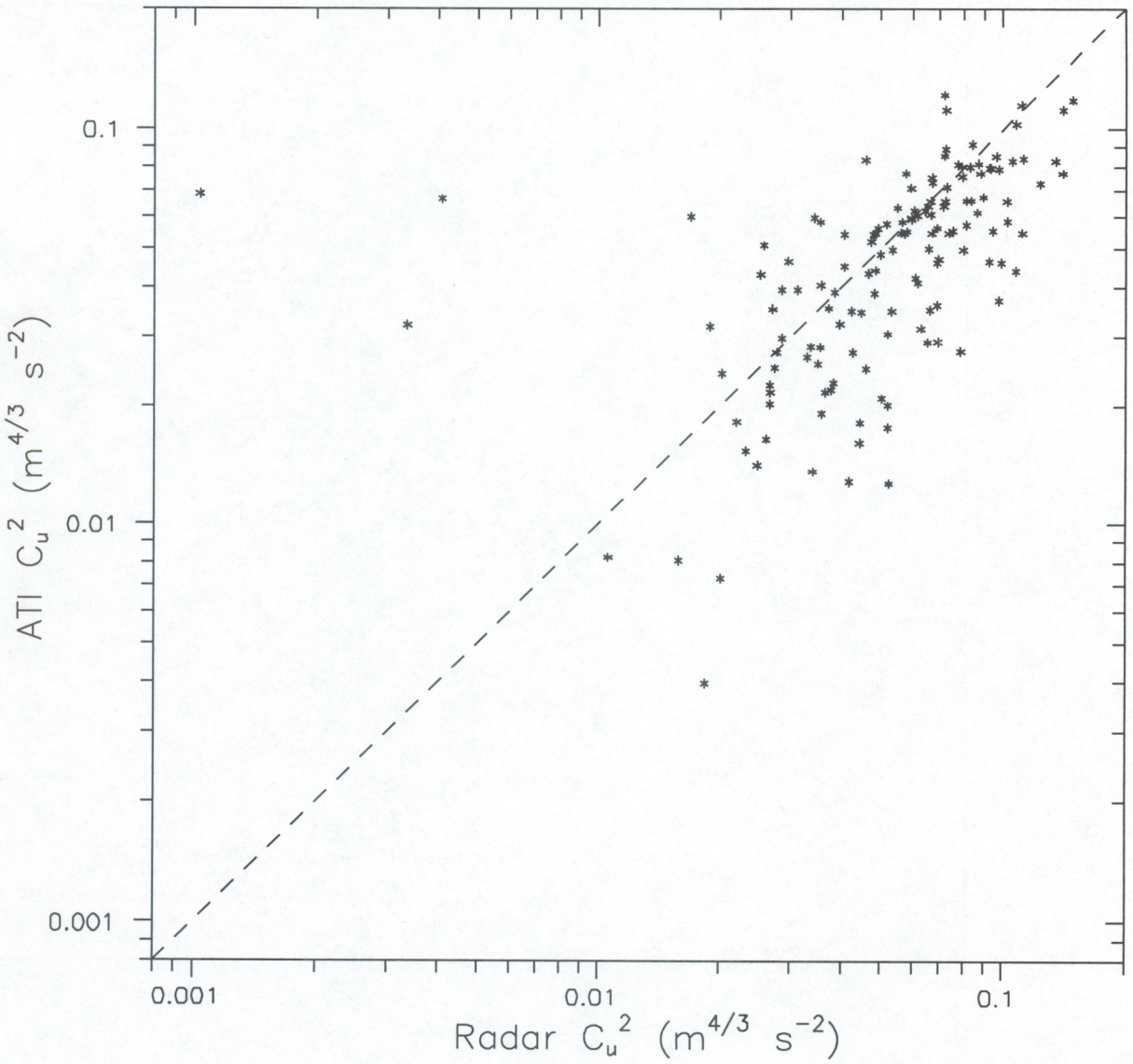

Figure 5.15. Scatterplot comparing C_u^2 calculated from the 14-min medians of spectral width measured by the radar with C_u^2 determined from the 14-min longitudinal velocity spectra measured with the ATI.

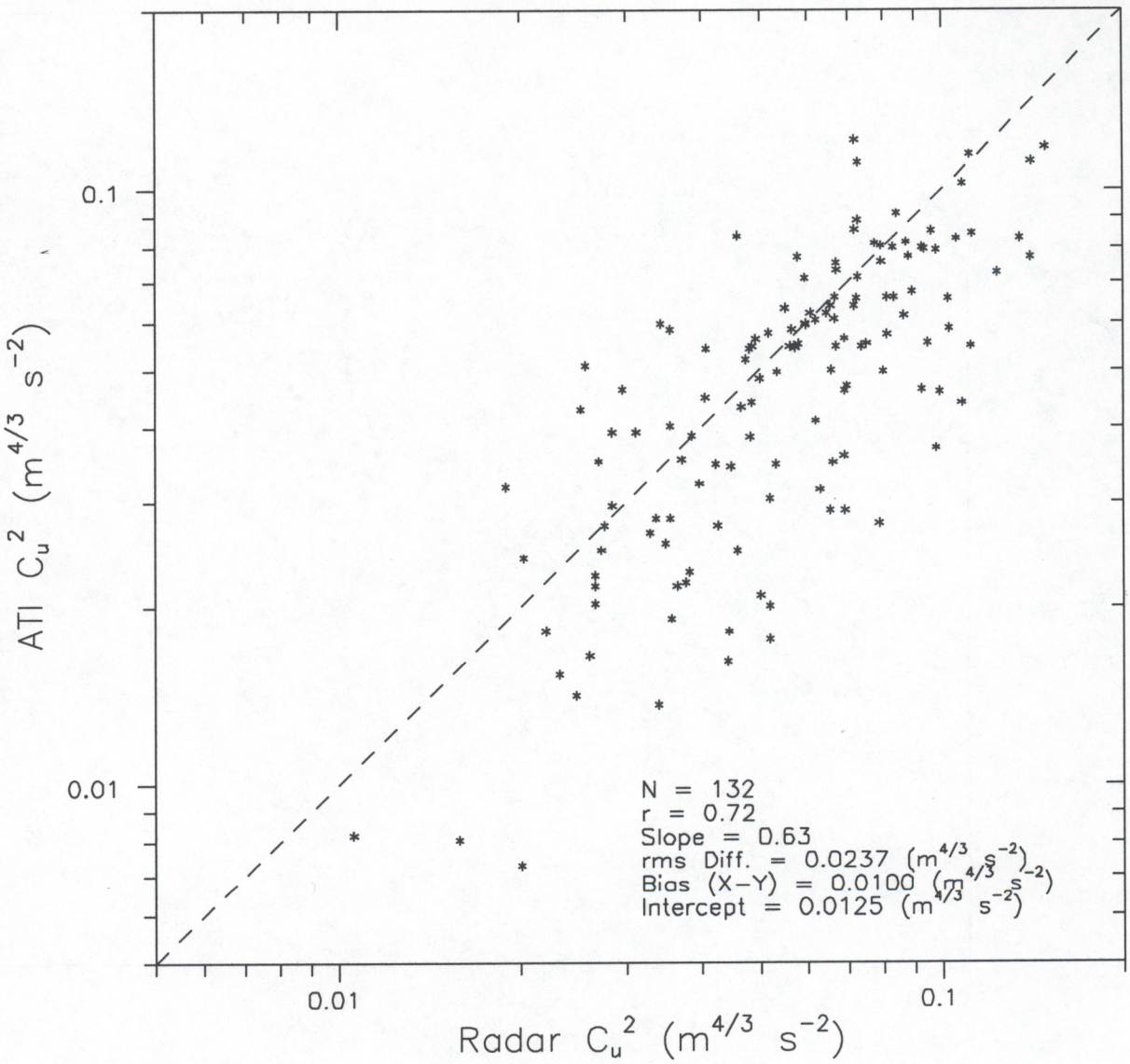

Figure 5.16. Same as Fig. 5.15, except with eight outliers removed. The number of observations, the correlation coefficient, and the results of linear regression analysis are given in the lower right.

measured values deduced from Doppler spectral width, but they were not satisfied with their results mainly because of spurious radar returns caused by side-lobe scattering from the tower structure. I know of no other similar comparisons. Gossard et al. (1995) calculated spectra from 20-min time series of radar-measured vertical velocity and compared them to the spectral density that resulted from the corresponding measurement of C_w^2 determined from the Doppler spectral width. The agreement was convincing, but only six range gates were examined during a single 20-min period.

The results shown in Fig. 5.16, along with the results given by Gossard et al. (1995), lend support to the usefulness of the radar technique. However, it is likely that improvements in the accuracy of radar measurements of velocity microturbulence could result from the development of new signal processing algorithms that compute spectral width more accurately.

6. RADAR OPERATING PARAMETER SENSITIVITY STUDIES

In this chapter I summarize the results of a series of experiments that were designed to investigate how the spectral moments are affected by changes in the fundamental radar signal processing parameters: n_c, n_f, and n_s. I use these studies to test the universality of the relationships that were used to derive C_n^2 and C_u^2 from radar measurements of reflectivity and spectral width. The results also suggest how the different segments of the radar dwell time should be allocated to optimize the radar's performance for different applications such as mean wind profiling and turbulence and to minimize (to the extent possible) the problems associated with radar measurements of turbulence discussed in Section 1.2.4.

I obtained the data for these analyses over a nine-day period (June 12–20, 1995) during which a commercial version of the radar described in Chapter 4 was operating at the Boulder Atmospheric Observatory (BAO) tower. I programmed the radar to point vertically during this period and turned off pulse coding, spectral windowing, and the ground clutter algorithm so as not to complicate the interpretation of the measurements. I conducted a number of experiments either using a constant set of signal processing parameters or alternating between two parameter sets for every average spectral cycle. All parameter sets used a 400-ns pulse, resulting in 60-m vertical resolution, a 23-μs interpulse period, and 33 gates. Table 6.1 lists the periods when data were collected, the mode of operation (constant or alternating parameter sets), the values of the parameters used, and the number of profiles measured. Table 6.2 lists the experiments conducted with the radar and gives schematic representations of the signal processing parameters used in each experiment. The results of these experiments are displayed as frequency distributions of the Doppler spectral moments measured at the third radar range gate, which is centered at a height of 240 m above ground level (AGL).

Table 6.1
Data collected for the radar operating parameter sensitivity studies.

Julian Day(s)	Times (MDT)	Mode	n_c	n_f	n_s	No. of Profiles
163	09:31-23:59	Constant	320	64	15	6383
164	00:00-11:10	Constant	320	64	15	4945
	11:11-23:59	Constant	320	64	100	914
165	00:00-11:15	Constant	320	64	100	803
	11:42-23:59	Alternating	320	256	15	706
			320	64	60	706
166	00:00-12:24	Alternating	320	256	15	712
			320	64	60	712
	13:37-23:59	Constant	320	64	100	741
167	00:00-11:56	Constant	320	64	100	853
	11:58-23:59	Alternating	320	64	30	1280
			80	256	30	1280
168-169	00:00-23:59	Alternating	320	64	30	5109
			80	256	30	5109
170	00:00-11:13	Alternating	320	64	30	1194
			80	256	30	1194
	11:28-23:59	Alternating	320	64	100	769
			320	64	15	769
171	00:00-08:42	Alternating	320	64	100	534
			320	64	15	534

Table 6.2
Radar signal processing parameter experiments.

Experiment Name (Section)	Signal Processing Stage and Resulting Radar Sampling Parameter					
	Coherent Integration (| = 40)	v_N (m/s)	FFT (| = 32)	Δv (cm/s)	Incoherent Integration (| = 10)	t_D (s)
Coherent Integration (6.1)	|||||||	11.1	||	3.5	|||	14.2
	||	44.6	|||||||	3.5	|||	14.2
Spectral Resolution (6.2)	|||||||	11.1	|||||||	0.87	||	28.3
	|||||||	11.1	||	3.5	||||||	28.3
Dwell Time (6.3)	|||||||	11.1	||	3.5	|||||||	47.1
	|||||||	11.1	||	3.5	||	7.1
					||	

Before proceeding with the results, it is appropriate to review briefly some of the concepts discussed in Chapter 4. The coherent integration period, Δt, is the amount of time required to produce a single point for the Fast-Fourier transform (FFT) and is found by multiplying n_c by the interpulse period (IPP). The Nyquist frequency associated with the resulting Doppler velocity spectrum is then given by $f_N = 1/(2\Delta t)$. The corresponding Nyquist velocity, or the maximum velocity magnitude that can be resolved unambiguously in the spectrum, v_N, is determined by inserting f_N in (4.5). Thus, $v_N = \lambda f_N/2$. The spectral velocity resolution, Δv, is given by taking the velocity interval, $2v_N$, and dividing it by the length of the FFT, i.e., $\Delta v = \lambda f_N/n_f$. The dwell time defined in (4.10) is the amount of time required for the profiler on-line program (POP) to collect and process all of the pulses ($n_c n_f n_s$) used to produce the average Doppler velocity spectrum.

6.1 Coherent Integration Period

In this experiment I programmed the radar to alternate between two parameter sets: one with $n_c = 80$, and one with $n_c = 320$. I kept the dwell time constant by changing the number of FFT points (see Table 6.1) so that the product $n_c n_f$ remained fixed for both parameter sets. In this case f_N changes, but Δv is constant.

Figure 6.1 shows frequency distributions of vertical velocity for each of the parameter sets. Aside from minor differences near 0 m s^{-1}, the two distributions are quite similar. The range-corrected signal-to-noise ratio (SNR) distributions are shown in Fig. 6.2. The SNR for the longer integration period is enhanced by approximately 6 dB. This increase is a direct result of coherent integration because, as described in Section 4.2.2, the coherent integration of n_c pulses improves the SNR by a factor of n_c (i.e., 320/80 = 4 = 6.02 dB). Thus, the radar C_n^2 equation given by (4.26) properly accounts for a change in the coherent integration period.

The frequency distributions for signal power and noise power are shown in Figs. 6.3 and 6.4. As explained in Section 4.2.2, the POP deals with an increase in n_c by reducing the noise power (Fig. 6.4) while keeping the signal power constant (Fig 6.3). The FFT is also a coherent process. However, if Δt is selected carefully to take advantage of the coherence time for atmospheric signals, then increasing the length of the FFT will not result in a further improvement in SNR. In other words, once the number of FFT points is adequate to resolve the spectrum, adding more points will not change the integrated power spectral density. The frequency distributions for Doppler width shown in Fig. 6.5 do not exhibit any notable differences but could if the SNR became too small.

The signal processing parameter changes made in this experiment do not affect radar performance for velocity turbulence applications because the velocity resolution and dwell time were the same for both parameter sets. However, an increased sensitivity to C_n^2 results because, although both parameter sets measure the same value of C_n^2, the parameter set that uses the longer coherent integration period has a higher SNR. The results here are also relevant to the applications of mean wind profiling and precipitation detection. Note that the

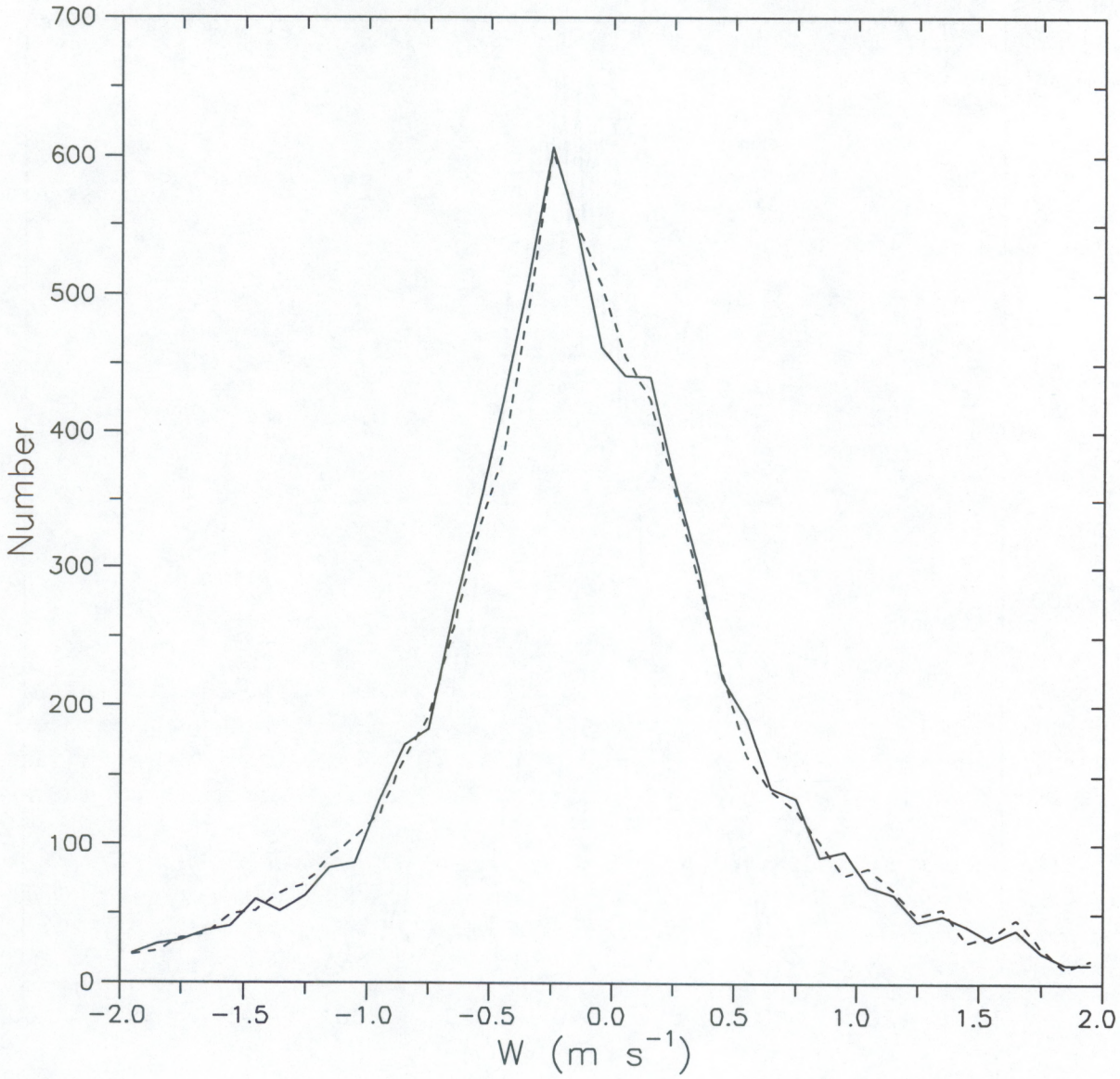

Figure 6.1. Frequency distributions of vertical velocity measured with a 915-MHz radar alternating between a long (n_c = 320) coherent integration period (solid curve) and a short (n_c = 80) coherent integration period (dashed curve). Each distribution contains 7,583 data from the third range gate centered at 240 m AGL. These data were collected over a four-day period (Julian days 167-170) in 1995 (see Table 6.1).

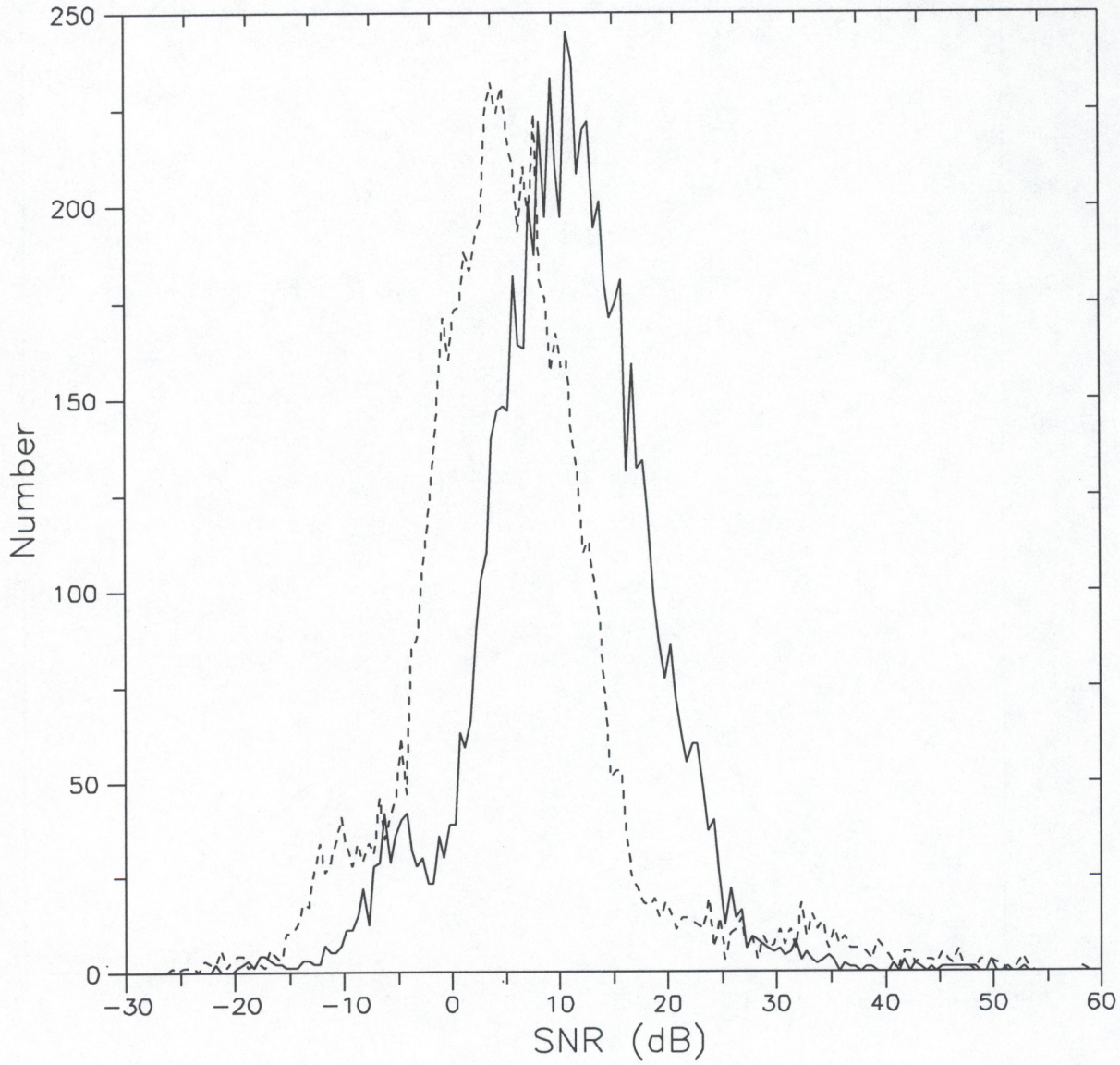

Figure 6.2. Frequency distributions of SNR for the long (solid curve) and short (dashed curve) coherent integration periods.

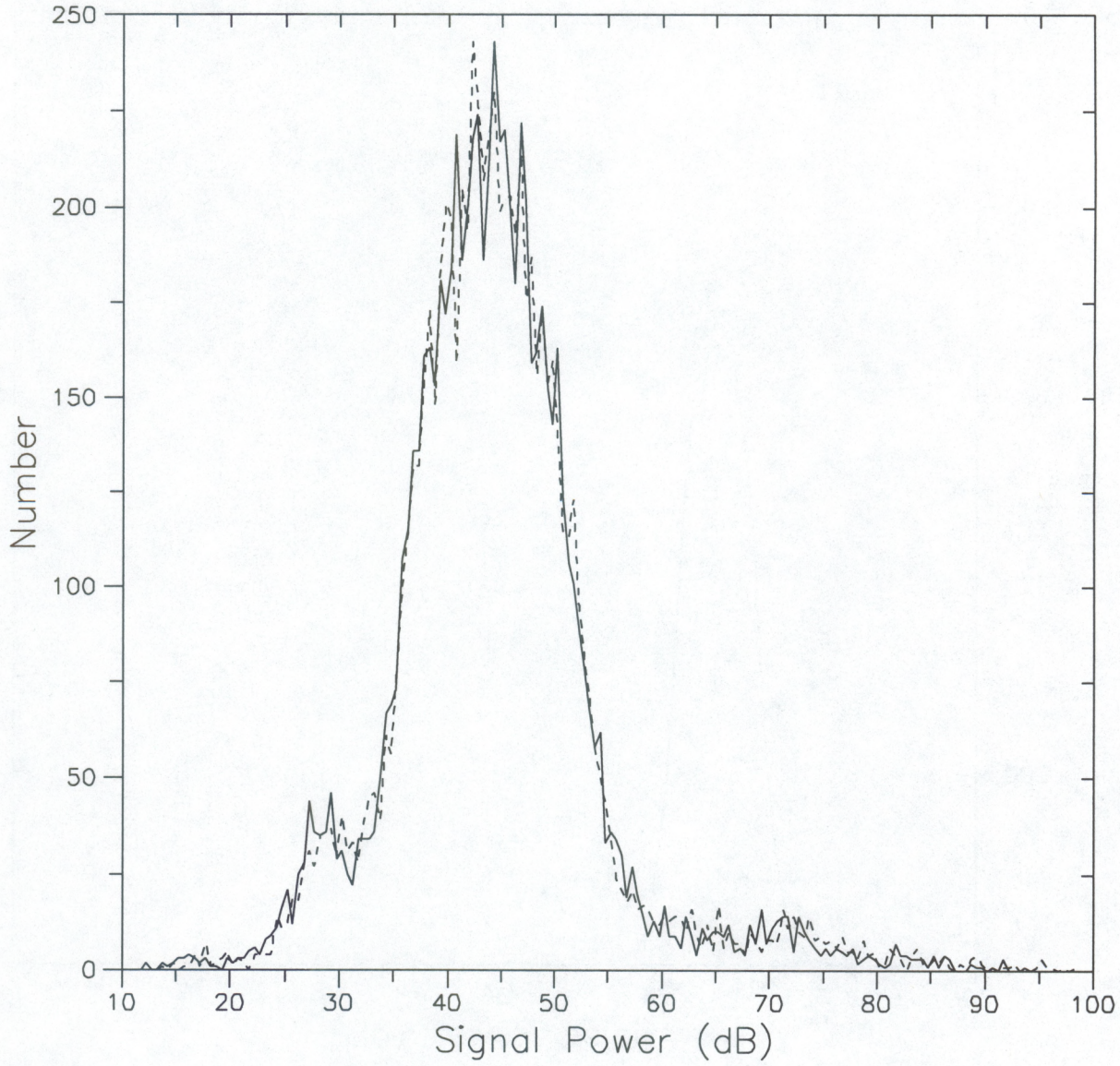

Figure 6.3. Frequency distributions of signal power for the long (solid curve) and short (dashed curve) coherent integration periods.

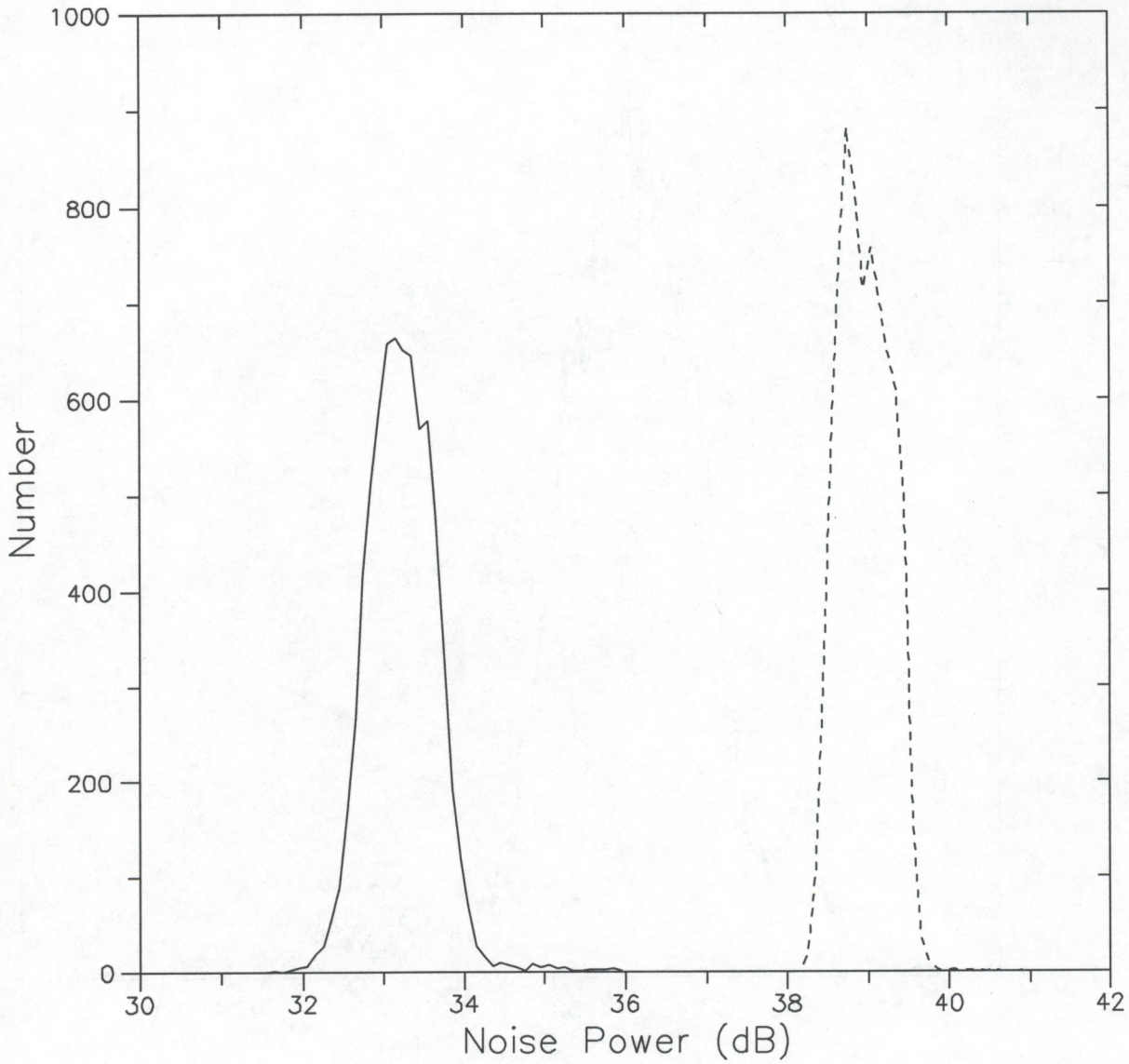

Figure 6.4. Frequency distributions of integrated noise power for the long (solid curve) and short (dashed curve) coherent integration periods.

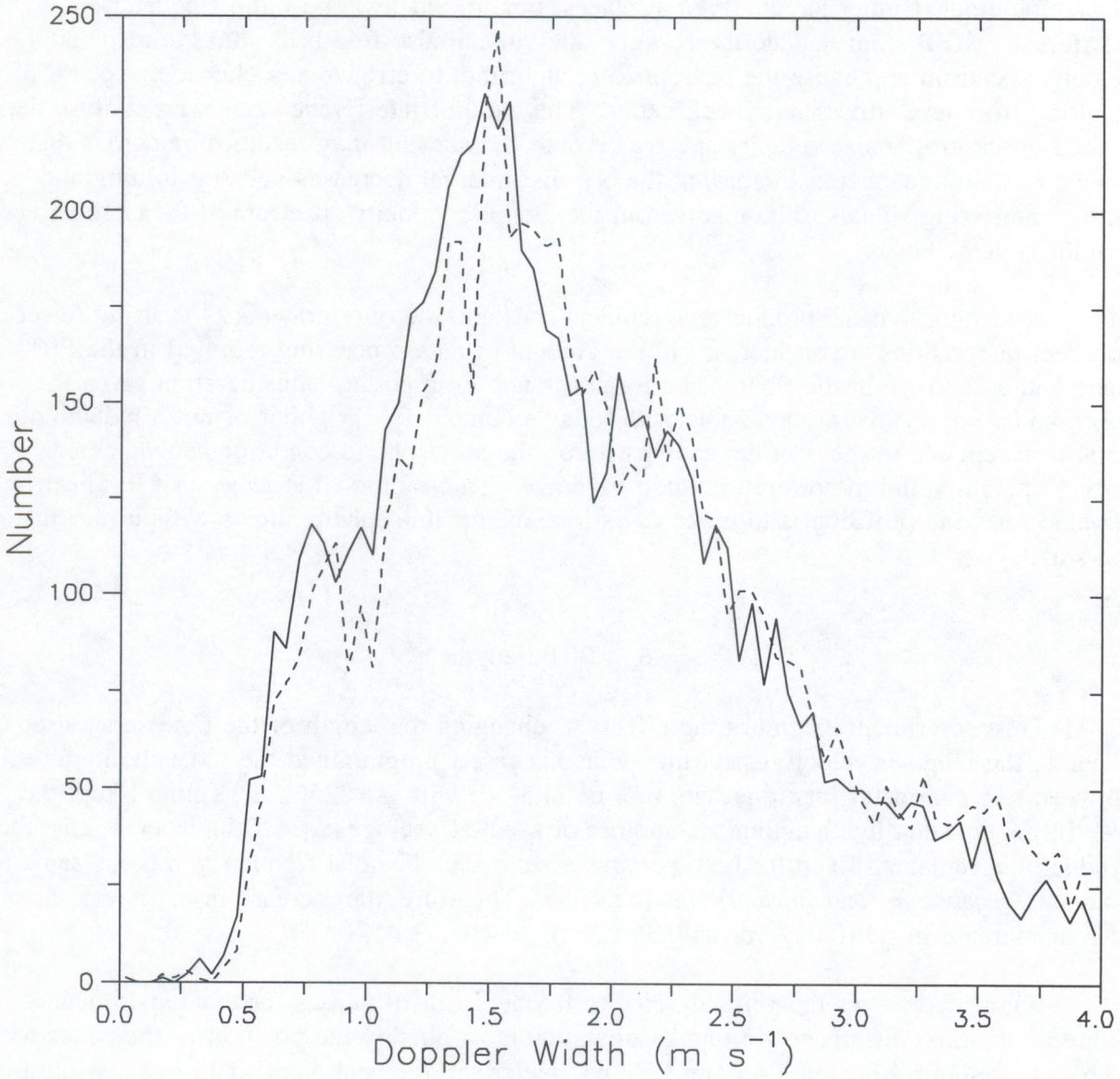

Figure 6.5. Frequency distributions of Doppler spectral width for the long (solid curve) and short (dashed curve) coherent integration periods.

shorter integration period leads to increases in f_N and v_N. A broader velocity range is advantageous for eliminating the problem of velocity folding (aliasing), which can occur when measuring a strong horizontal wind field or when the radar is used to detect the fall velocity of precipitation. Clutter targets (e.g., airplanes, motor vehicles) and radio frequency interference (RFI) from outside the Nyquist interval can also fold back into the resolved velocity spectrum and cause the peak picking algorithm to erroneously choose a spectral peak resulting from non-atmospheric backscatter. This kind of interference can even confuse the trained observer of radar velocity spectra because the aliasing may result in velocities that are typical of the atmosphere. Increasing the Nyquist interval decreases velocity folding and allows interfering signals to be resolved in the Doppler velocity spectrum at their proper (i.e., unfolded) velocities.

Assuming that the product $n_c n_f$ remains constant, the only drawbacks to using fewer coherent integrations are an increase in the amount of data processing required in the FFT stage and a decrease in the SNR. The former is not an important consideration given the speed and memory that are available with today's computers. Whether or not a reduction in SNR is acceptable to the user depends partly on the atmospheric conditions encountered during operation and the desired altitude coverage. The traditional strategy that has been adopted for wind profiling is to make Δt as long as the atmosphere allows without making v_N too small.

6.2 FFT Length

This experiment examines the effects of changing the length of the time series used to generate the Doppler velocity spectrum. For this case I programmed the radar to alternate between two parameter sets: one with $n_f = 64$ and one with $n_f = 256$. This time I kept the dwell time constant by changing the number of spectral averages (see Table 6.1), so that the product $n_f n_s$ remained fixed for both parameter sets. The Nyquist frequency was the same for both sets because n_c (and thus Δt) was the same. Therefore, the increase in n_f gives a factor-of-four increase in Δv (0.087 versus 0.35 m s^{-1}).

Figure 6.6 shows the vertical velocity frequency distributions for this experiment. There are marked differences in the distributions, most notably the position of the peaks with respect to velocity. For the 64-point FFT parameter set, the peak is at -0.25 m s^{-1}, while for the 256-point FFT parameter set, the peak is at -0.05 m s^{-1}. There are several reasons why these peaks may occur at negative velocities rather than at zero. First, synoptic conditions were favorable for large-scale subsidence. Secondly, because of westerly flow aloft and the nearby Rocky Mountains, the vertical-velocity distributions measured at the BAO site were likely influenced by the presence of a quasi-stationary lee wave. Thirdly, according to the times listed in Table 6.1, approximately one-third of the data for this experiment were collected in the daytime convective boundary layer (CBL). The frequency distributions of vertical velocity in the CBL are expected to have a negative mode because most of the

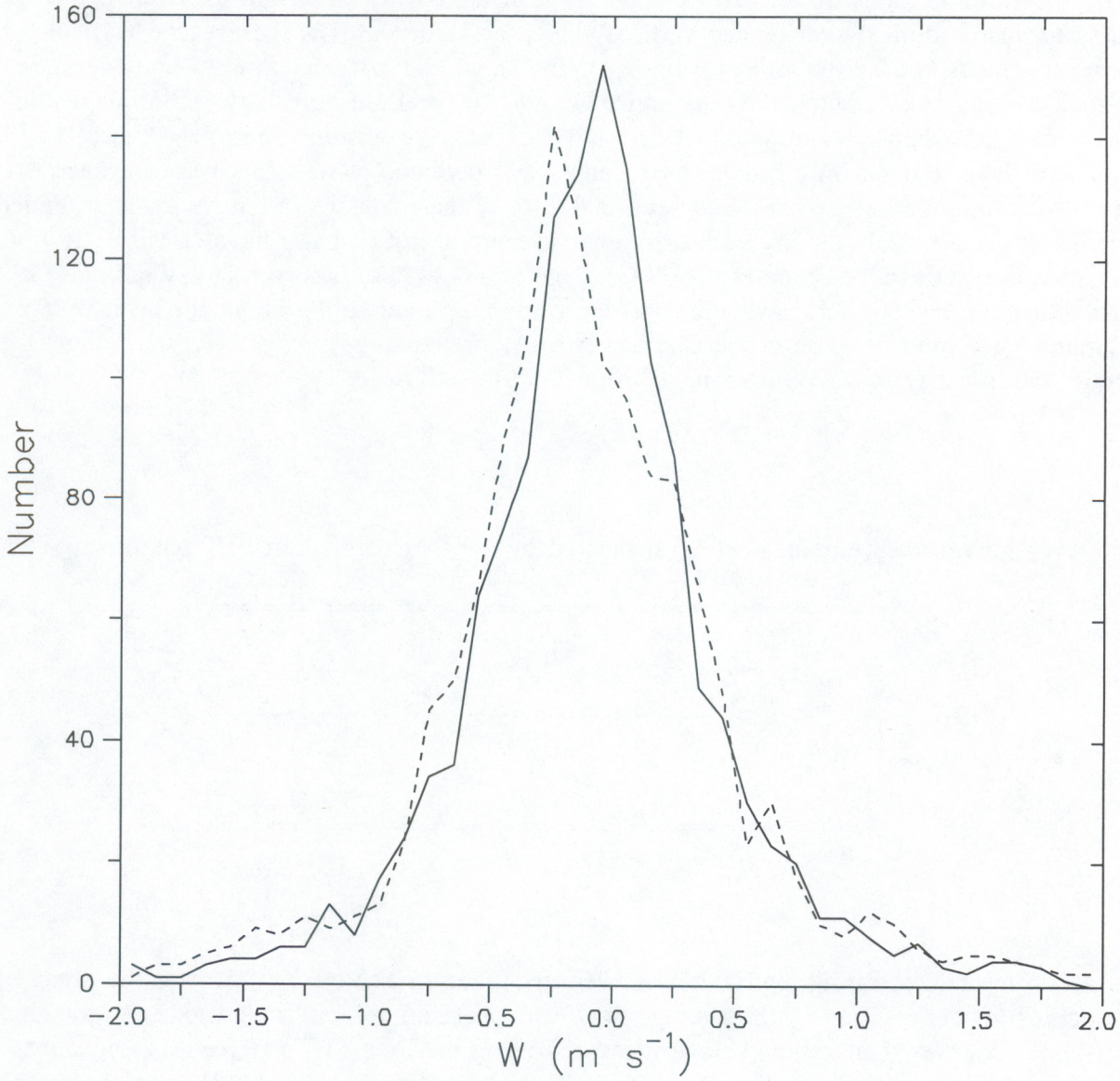

Figure 6.6. Frequency distributions of vertical velocity measured with the radar alternating between a long (256-point) FFT (solid curve) and a short (64-point) FFT (dashed curve). Each distribution contains 1,418 data from the third range gate centered at 240 m AGL. These data were collected on Julian days 165 and 166 (see Table 6.1).

upward mass transport occurs in intense, narrow updrafts, whereas mass balance is achieved by much weaker but more persistent subsidence.

While the mode of the vertical-velocity distribution in convection may be negative, mass balance requires a zero mean vertical velocity. Table 6.3 lists the average vertical velocities measured by the radar for the long and short FFT parameter sets. The average vertical velocities computed over the entire Nyquist interval are unrealistic. Similar results were obtained when the National Oceanic and Atmospheric Administration (NOAA) 915-MHz boundary-layer radar/wind profiler (NBL radar) was operated at sites that were far away from any major topographic features (see Section 1.2.4). Other investigators have taken extended time series of vertical velocity with different radar/wind profilers and have consistently found negative averages (e.g., Green et al., 1988; Gage et al., 1991). Nastrom and VanZandt (1994) proposed that the long-term average subsidence measured above the boundary layer by the Flatland VHF radar in Illinois was due to vertically propagating gravity waves. In their study, the monthly mean values ranged from -0.03 to -0.07 m s^{-1}.

Table 6.3

Average vertical velocities (m s^{-1}) measured by the long- and short-FFT parameter sets.

	$\overline{w}_{256}$	$\overline{w}_{64}$
$\lvert w \rvert \leq 2$ m s^{-1}	-0.08	-0.11
$\lvert w \rvert \leq v_N$	-0.27	-0.31

Another interesting feature of the averages given in Table 6.3 is that for the range of velocities between ±2 m s^{-1}, the average downward vertical velocity measured with the short FFT is 37.5% larger than the average measured using the long FFT. Here, it is relevant to consider the implications of direct current (DC) filtering (see Section 4.2.3). For the moment, assume there is no mean vertical motion during a particular radar measurement cycle. With DC filtering, the energy in the Doppler velocity spectrum at 0 m s^{-1} is removed or drastically reduced. Therefore, the peak picking algorithm searches for a signal peak in the velocity bins adjacent to DC. The moment algorithm can still calculate a velocity of 0 m s^{-1}, but only if the resulting signal after DC filtering is symmetric about DC. The frequency distributions shown in Fig. 6.6 show that, on average, DC filtering biases radar vertical-velocity measurements away from 0 m s^{-1} by an amount that is proportional to ΔV. The distributions also show that this bias can be reduced significantly by increasing velocity resolution, thereby allowing the POP to resolve smaller (magnitude) velocity fluctuations.

The SNR (Fig. 6.7) did not change appreciably in this experiment because the number of coherent integrations was the same in both parameter sets. In addition, because the SNR was unaffected, the signal power and noise power distributions (not shown) were quite similar as well.

On the other hand, the distributions for Doppler spectral width shown in Fig. 6.8 are significantly different. The addition of spectral points allows the POP to resolve narrower spectral peaks. In this case increasing the number of spectral points from 64 to 256 led to roughly a factor-of-two improvement in the minimum resolvable Doppler width or a factor-of-four improvement in the corresponding minimum resolvable variance. It is also interesting to note the behavior of the distribution tails, where the measured widths are large compared to the velocity resolutions and, therefore, should not be as sensitive to ΔV. However, for widths ranging from 2 to 4 m s^{-1}, the distribution for the 64-point FFT contains 58% more data than the distribution for the 256-point FFT. With the dwell time fixed, this result must be accounted for by the increase in the number of spectra averaged together for the shorter FFT. The equations used to derive C_u^2 from radar measurements of spectral width (see Section 5.3.2) do not account for this result because the increase in velocity resolution is not accompanied by an increase in dwell time.

This experiment has important implications for both mean wind profiling and applications involving turbulence. I first consider mean wind profiling and assume that the combined error introduced to the radial velocity estimate by the DC filter and a coarse resolution of the Doppler velocity spectrum is Δv. Over half of the distribution of vertical velocities shown in Fig. 6.6 for the 256-point FFT parameter set lie within the velocity range -0.35 to 0.35 m s^{-1}. Thus, for the parameter set that used the 64-point FFT and had a velocity resolution of 0.35 m s^{-1}, a large portion of the vertical-velocity measurements are dubious. The relative error for horizontal winds should not be as severe because the magnitudes of the oblique radial velocities are generally larger than the magnitude of the vertical radial velocity. Therefore, fewer observations from oblique pointing beams should be affected by the DC filter. On the other hand, the oblique radial velocities are multiplied by $1/\cos(\psi)$ to convert them to horizontal velocities. Since ψ is typically 75°, the absolute error for horizontal wind measurements that are affected by the DC filter is nearly a factor of four larger than the error for vertical velocity.

I did not use the time series of radial velocities measured by the radar except to demonstrate the averaging filter that is imposed by the radar sampling. However, other turbulence applications make direct use of these measurements. For example, Angevine et al. (1993b) used the velocity and temperature measurements from a 915-MHz wind profiler equipped with the radio acoustic sounding system (RASS) to calculate profiles of heat and momentum flux using the eddy correlation technique. Any improvement in the accuracy of radial velocity or spectral width will also lead to better estimates of variance, since the total variance measured by the radar is a combination of a resolved variance, which is controlled by the radar sampling, and an unresolved variance, which contributes directly to the broadening of the spectrum. We saw that an increase in spectral resolution also improved the

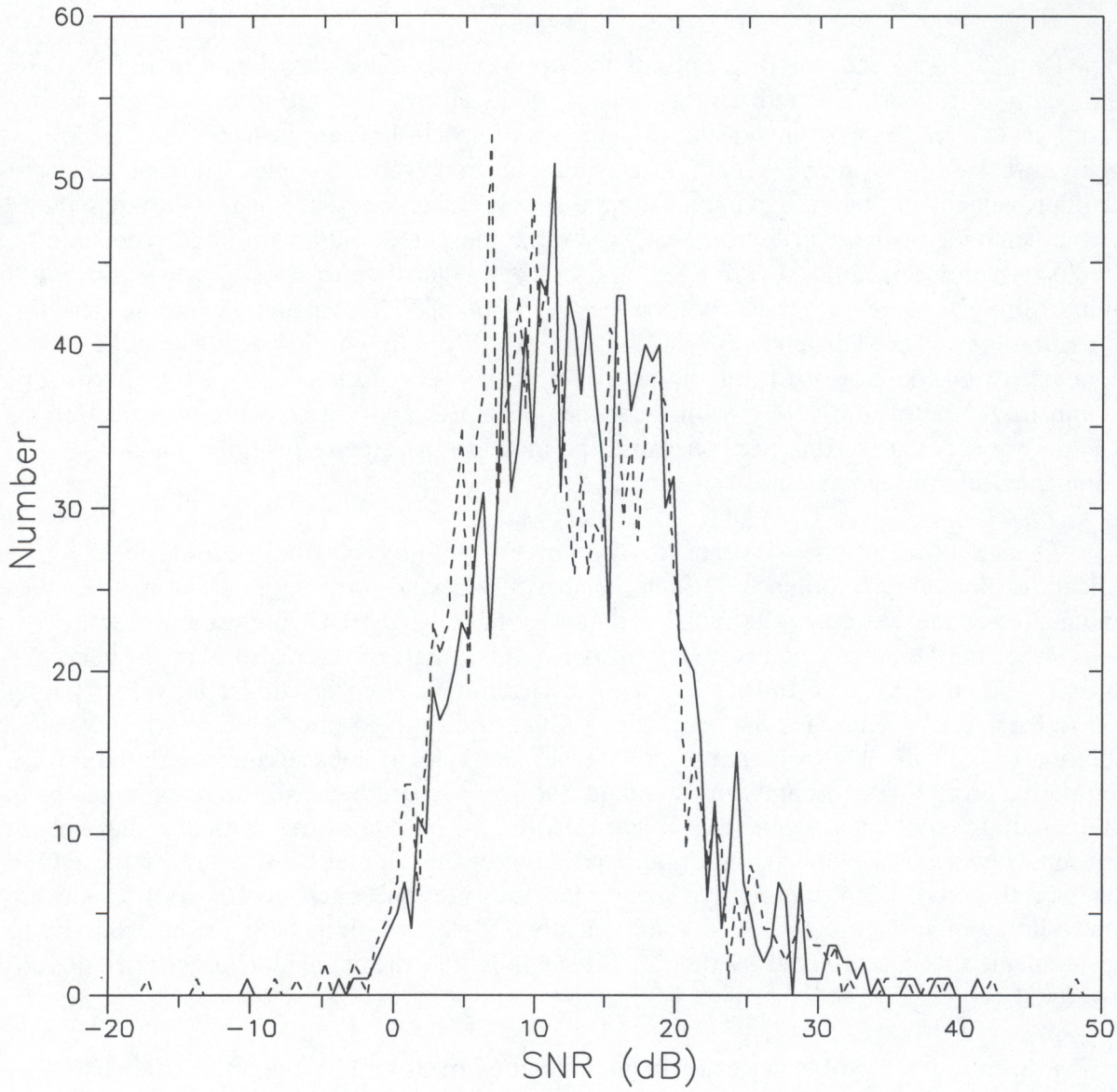

Figure 6.7. Frequency distributions of SNR for the long (solid curve) and short (dashed curve) FFTs.

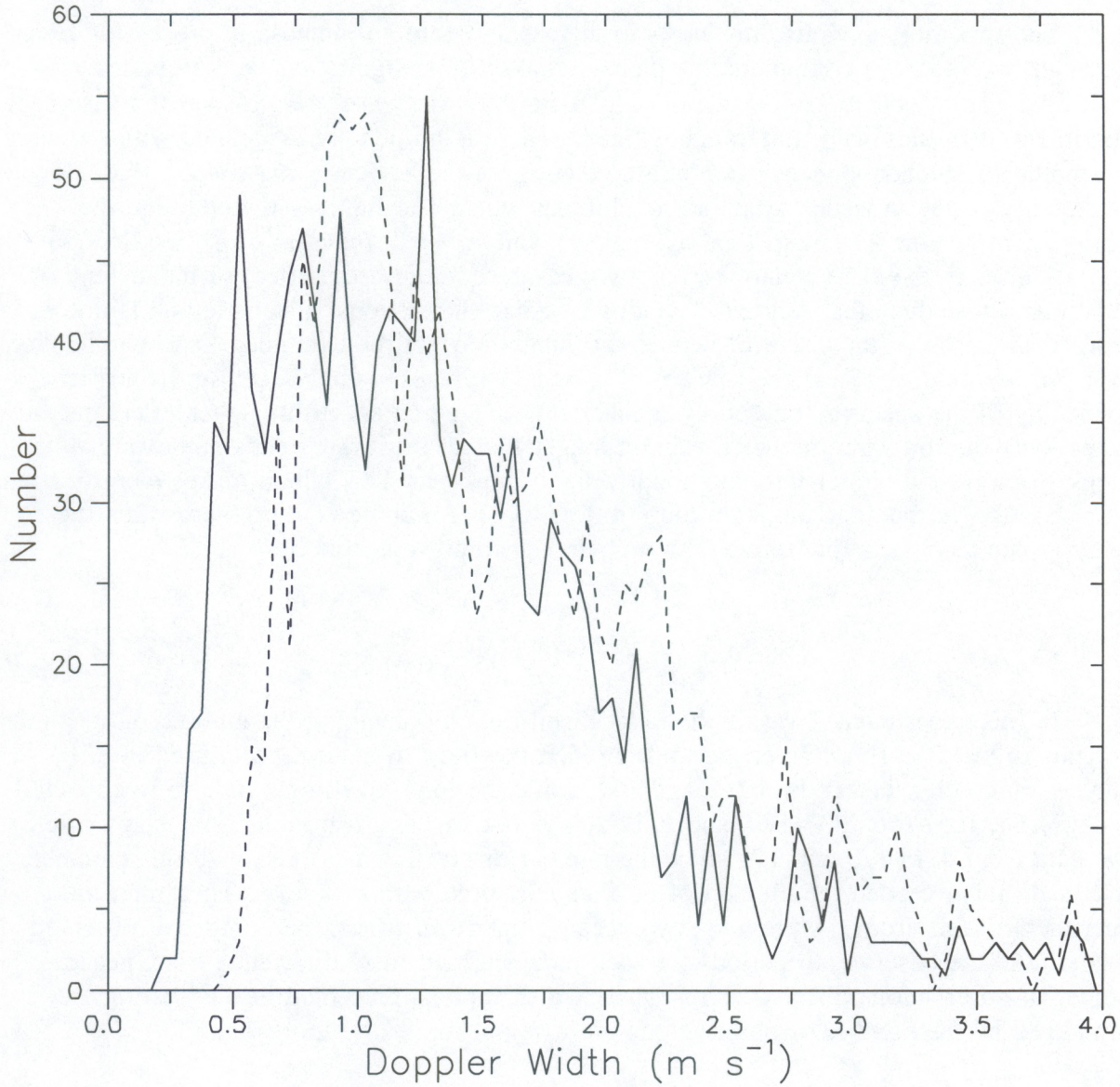

Figure 6.8. Frequency distributions of Doppler spectral width for the long (solid curve) and short (dashed curve) FFTs.

spectral width measurement by allowing narrower peaks to be resolved in the spectrum. This result would, for example, allow smaller values of C_u^2 to be estimated using the technique described in Section 5.3.2.

The two most obvious drawbacks to increasing n_f are an increase in processing time (although, with today's computers this increase should be insignificant) and an increase in dwell time. However, if the increase in n_f is offset by a decrease in n_s, as was the case in this experiment, then the dwell time remains fixed. There is no penalty associated with reducing the amount of incoherent integration at altitudes where the SNR is large enough that detectability is not an issue. Also, at the altitudes where detectability is important, the improvement resulting from spectral averaging is only a weak function of n_s (see Section 4.2.4). This improvement cannot be readily measured, because the effect of incoherent averaging is to reduce the standard deviation of noise fluctuations, a statistic that is not recorded in the POP (the effect of incoherent integration will be examined further in Section 6.3). Furthermore, reducing the number of spectral averages should decrease the artificial broadening of the spectrum caused by incoherently averaging spectra together. Perhaps the biggest obstacle to overcome when using a longer FFT at most radar sites is the spread of energy from ground clutter into additional velocity bins near DC, which makes identification and separation of the contamination more difficult. This is more of a problem when the clutter is due to objects that move with the wind, such as vegetation.

6.3 Dwell Time

In this experiment, I varied the radar dwell time by changing the number of spectral averages from 15 to 100. Referring to Table 6.1, the short dwell-time data used in this analysis were collected on days 163 and 164, while the long dwell-time data were collected on days 164, 165, 166, 167, 170, and 171. It was not necessary to include the short dwell-time data from days 170 and 171 since the number of profiles measured with this parameter set already far exceeded the number of profiles measured with $n_s = 100$. Therefore, this experiment differs from the previous two because the dwell times, the number of observed profiles, and the observation periods for each parameter set were different. Also, because the number of observations differed, the frequency distributions presented in this section are normalized by the number of observations occurring at the distribution peak.

The vertical-velocity distributions are shown in Fig. 6.9. The velocities corresponding to the peaks in the distributions are slightly different. This difference may not be significant because the velocity resolution in the Doppler spectrum for both cases was 0.35 m s^{-1}, whereas the peaks are separated by only 0.05 m s^{-1}, which corresponds to the resolution used to sample the distributions. Both distributions are notched at the first positive velocity bin. The underrepresentation of the small updraft velocities is caused by the DC filter and the biasing discussed in Section 6.2. I cannot explain why the notch is more severe for the short dwell-time parameter set, although the differences in the number of observations and the observation periods may have contributed to this outcome.

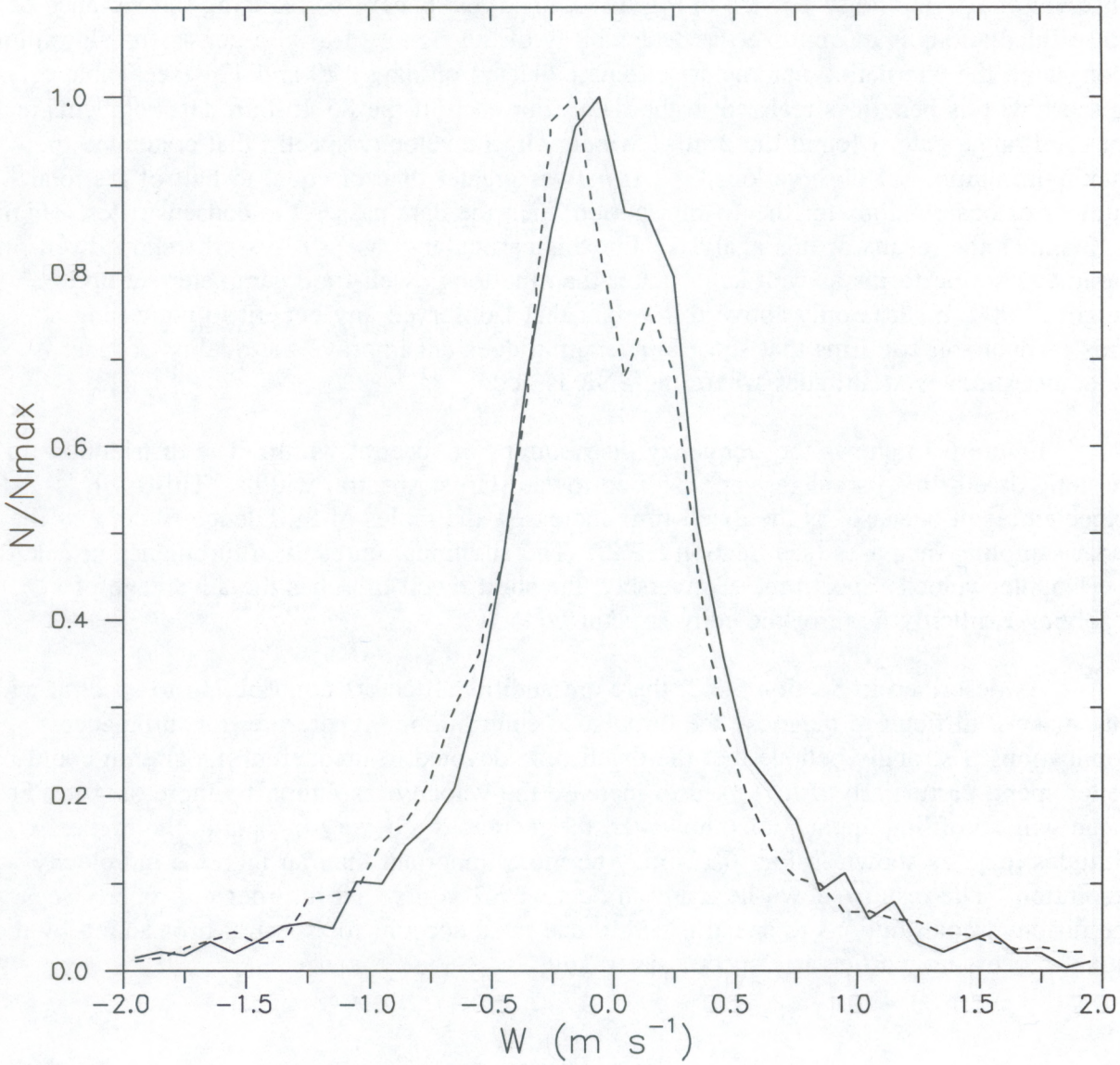

Figure 6.9. Frequency distributions of vertical velocity measured with the radar using either a long (n_s = 100) dwell time (solid curve) or a short (n_s = 15) dwell time (dashed curve). The short dwell-time distribution contains 11,328 data from Julian days 163 and 164. The long dwell-time distribution contains 4,614 data from Julian days 164-167, 170, and 171 (see Table 6.1). All data are from the third range gate centered at 240 m AGL.

The SNR distributions (Fig. 6.10) are quite similar, but the noise power distributions (Fig. 6.11) are noticeably different. According to Section 4.2.4, increasing n_s reduces the variance of noise fluctuations. This result is manifested by a narrowing of the distribution of observed integrated noise powers in Fig. 6.11. The real benefit of reducing the variance of noise fluctuations is to improve the detectability of the signal. I used a consensus algorithm, along with the alternating parameter set data collected on days 170 and 171 (see Table 6.1), to see how this benefit is realized in the data. For each of the 85 15-min data segments and for each range gate, I found the 2 m s^{-1} window in the velocity spectra that contained the maximum number of observations, n_m. If n_m was greater than or equal to half of the total number of observations for the 15-min period, then the data passed the consensus test. Figure 6.12 shows the results of this analysis. For this particular consensus test, the short dwell-time parameter set performs as well as or better than the long dwell-time parameter set up to a height of 900 m. It is only above this height that I observed any benefit to increasing n_s. This comparison confirms that spectral averaging does not improve the quality of radar velocity estimates at altitudes where the SNR is good.

Figure 6.13 shows the frequency distributions of spectral width. The distribution for the long dwell-time parameter set is shifted toward larger spectral widths. This is an expected result because, as the dwell time increases, the scales of turbulence filtered by the radar sampling increases (see Section 5.3.2). The additional unresolved turbulence broadens the Doppler velocity spectrum. Conversely, the short dwell time has the advantage of resolving explicitly more of the eddy structure.

As described in Section 5.3.2, there are additional factors contributing to spectral width that make it difficult to diagnose the turbulence contribution. Therefore, for turbulence applications, I strongly believe that the dwell time devoted to incoherent integration could be better spent, particularly if it is used to increase the velocity resolution by increasing n_f. For mean wind profiling applications, however, the increased recovery of data at the higher altitudes (e.g., as shown in Fig. 6.12) may be more important than an increase in velocity resolution. The results shown here and in Section 6.2 verify that in order to properly separate the different contributions to spectral width, one must account for spectral broadening by the signal processing, particularly spectral averaging.

6.4 Discussion

The results described above have a number of important implications for wind profiler research and applications. Because a number of studies have now shown that the NBL radar incorrectly measures the mean vertical velocity in convection, possibly because of Rayleigh scattering from insects or other particulates, any applications that make use of vertical-velocity fluctuations measured by the NBL radar must first remove the mean. In the absence of Rayleigh scatterers, a negative velocity bias may still exist, and Fig. 6.6 shows that this problem is exacerbated when a coarser spectral resolution is used.

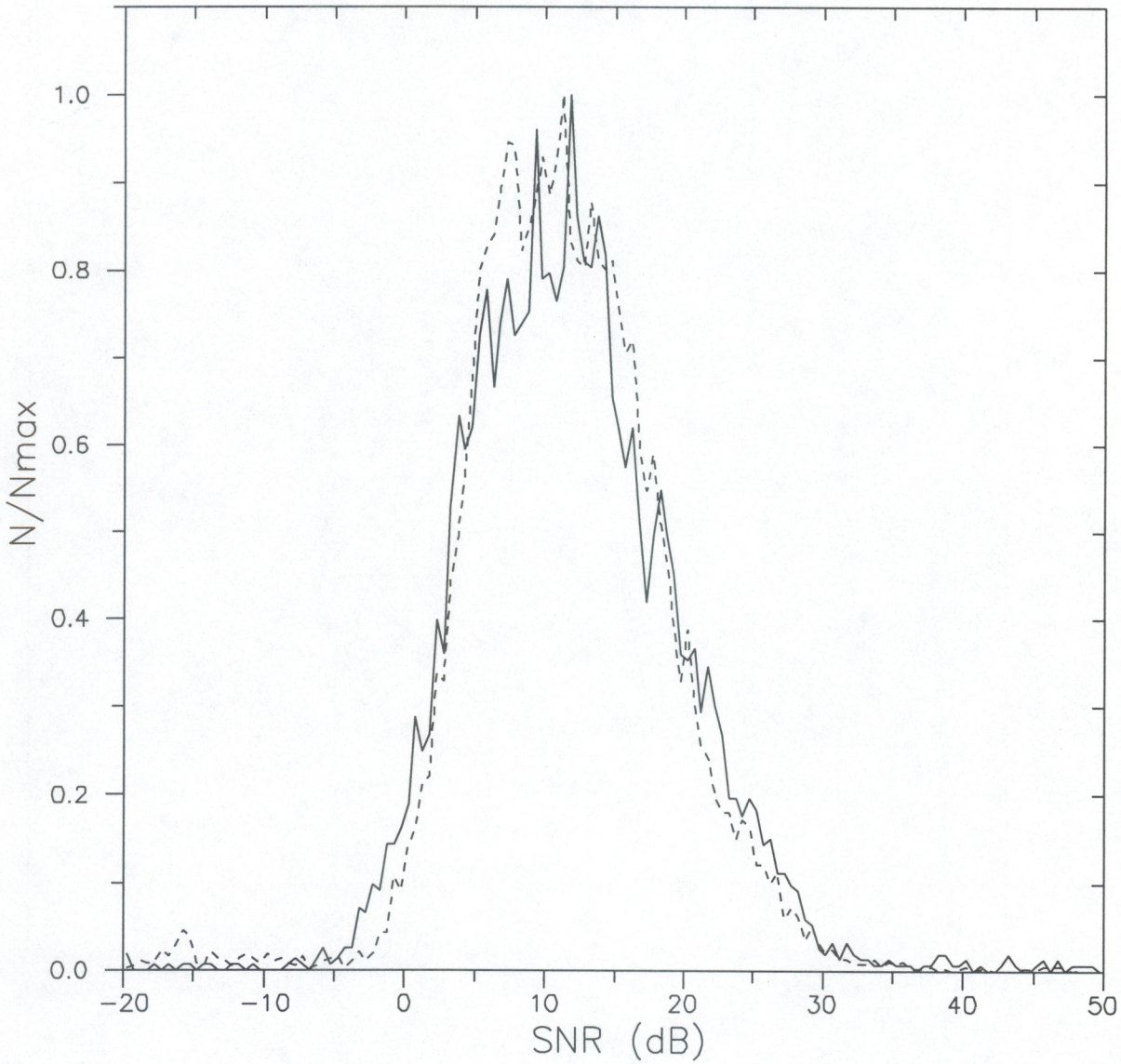

Figure 6.10. Frequency distributions of SNR for the long (solid curve) and short (dashed curve) dwell times.

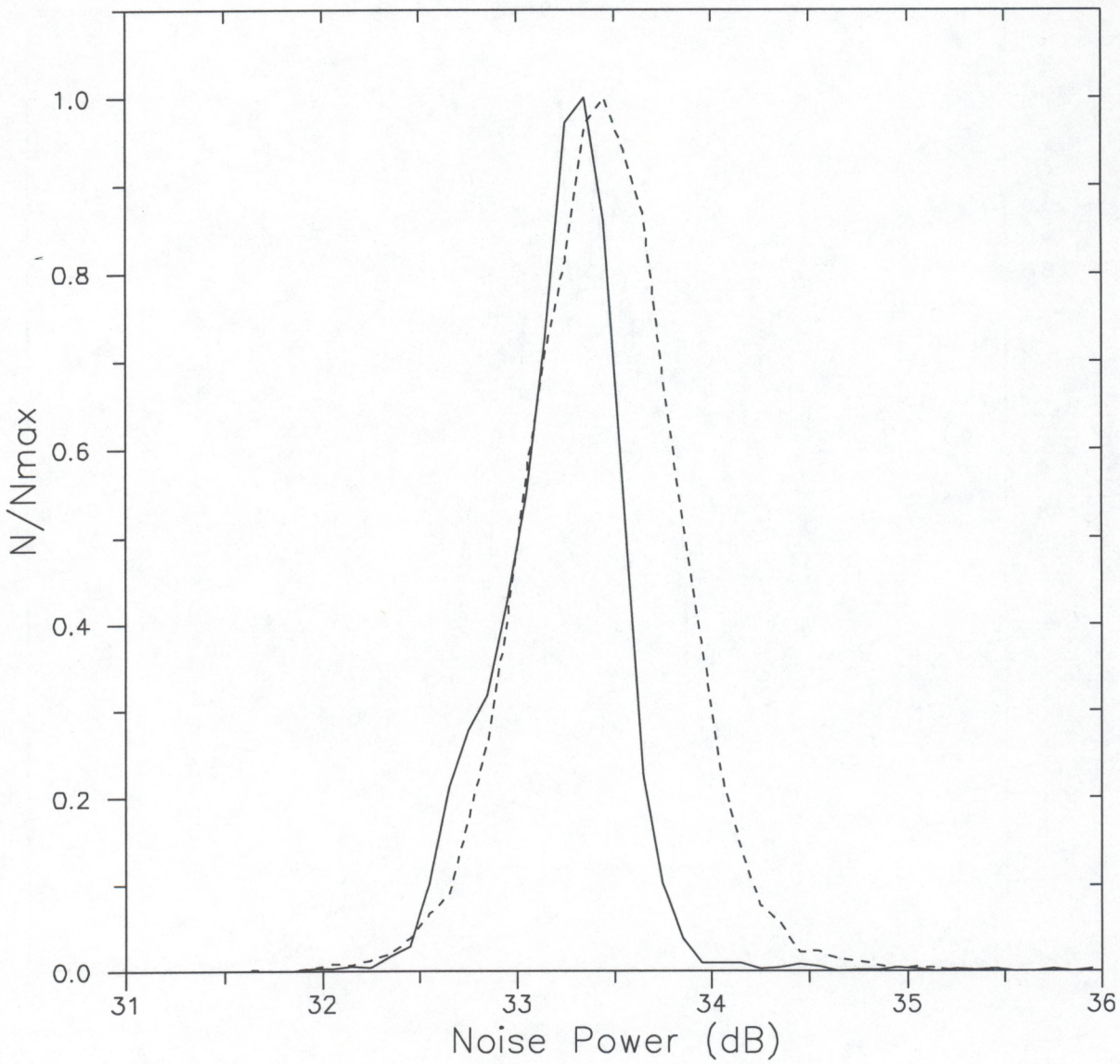

Figure 6.11. Frequency distributions of noise power for the long (solid curve) and short (dashed curve) dwell times.

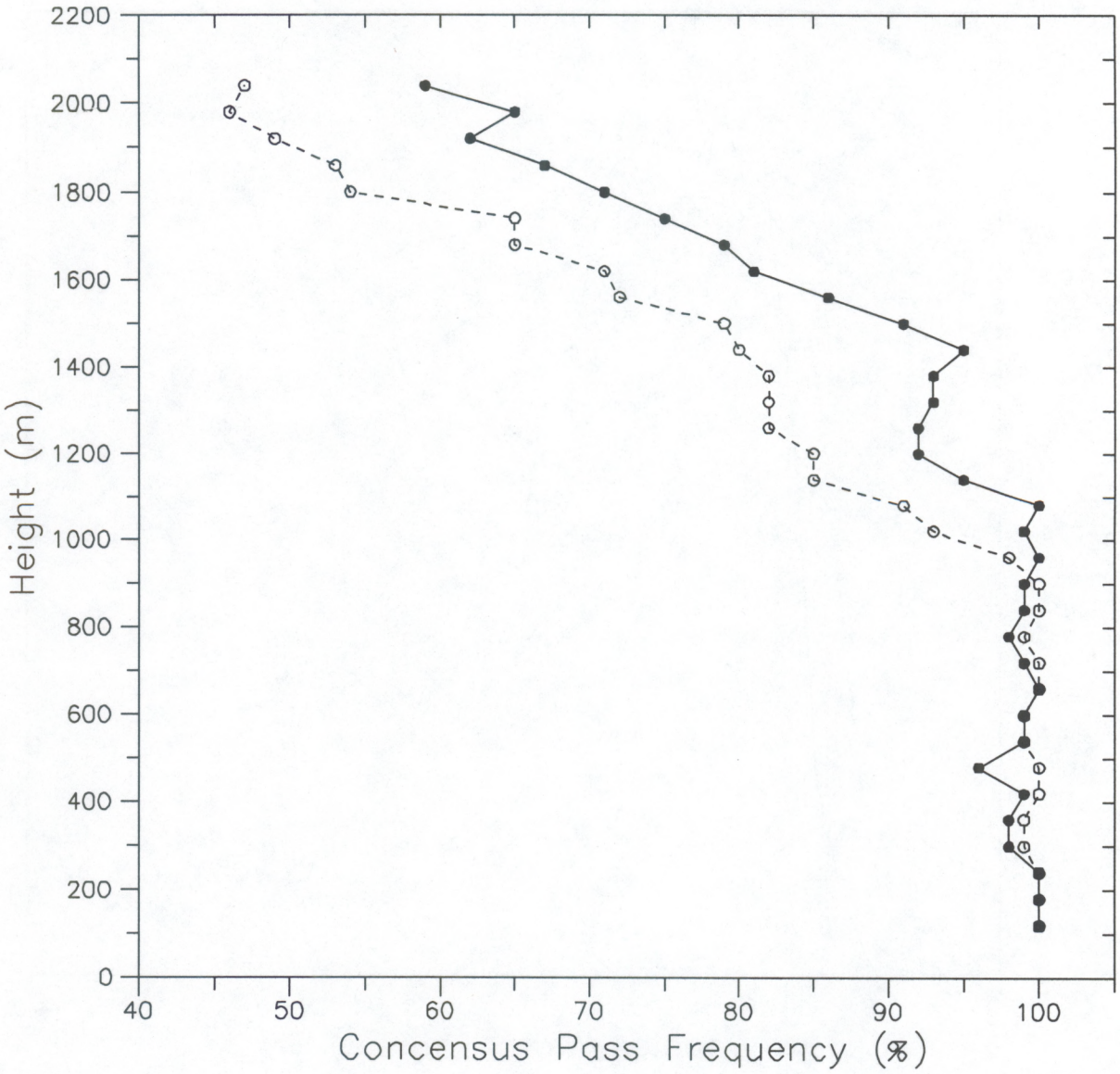

Figure 6.12. Height profiles for the long (solid curve with filled circles) and short (dashed curve with open circles) dwell-time parameter sets giving the percentage of 15-min vertical-velocity segments that passed the consensus algorithm described in the text.

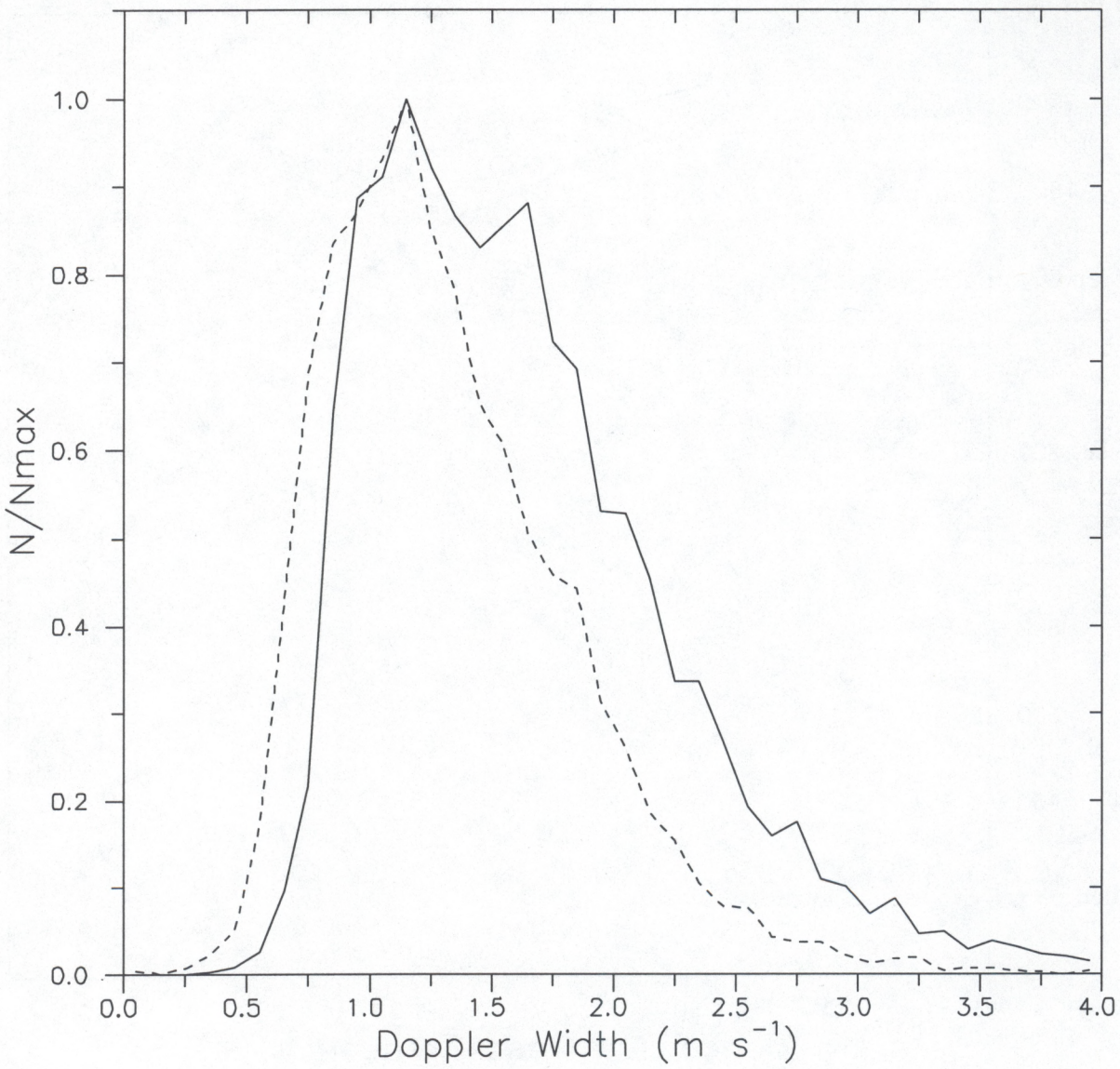

Figure 6.13. Frequency distributions of Doppler spectral width for the long (solid curve) and short (dashed curve) dwell times.

Determining the spectral broadening attributable to turbulence is not an easy task. First, there is the error imposed by the finite beamwidth, which, in the case of the NBL radar, is rather severe. Then there are the corrections for pulse volume and dwell-time averaging. In this chapter I demonstrated how specific stages of the signal processing can affect the measurements of spectral width. Perhaps not surprisingly, a substantial change in the distribution of spectral widths was observed when I varied the spectral resolution (or, alternatively, the number of FFT points). This is an important result because the current standard technique for interpreting spectral width does not include this effect. Additionally, placing more points in the spectrum allows the moment-generating algorithm to resolve smaller widths, thereby increasing the sensitivity of the radar for this particular measurement. I also showed (Fig. 6.13) that the number of spectral averages affects the distribution of observed spectral widths. Since increasing the number of spectral averages results in increasing the dwell time, the correction that I applied to account for dwell-time averaging should compensate for this effect.

Of the three operating parameters examined, only the number of coherent integrations affected the SNR. The equation used to calculate C_n^2 correctly accounts for this dependence because the ratio of SNR to n_c appears in (4.26). The radar C_n^2 equation should then generally be applicable given that the radar half-wavelength lies within the inertial subrange. An exception occurs when the turbulence does not fill the radar pulse volume. This is mainly a problem above the CBL or in the stably stratified boundary layer where the turbulence may be confined to layers thinner than the pulse length. In these cases the fraction F of the radar pulse volume filled with turbulence must be estimated or parameterized (Cohn, 1995).

7. SUMMARY AND CONCLUSIONS

In the past, comparisons between Doppler radar/wind profilers and in situ sensors often relied on radiosondes (and, on fewer occasions, aircraft and tethersondes) to serve as platforms for the in situ sensors. The improved resolution and low-altitude coverage provided by the recently developed boundary-layer radars have allowed comparisons between radars and towers. In this memorandum I described a comparison of scalar and velocity microturbulence statistics measured by the National Oceanic and Atmospheric Administration (NOAA) 915-MHz boundary-layer radar/wind profiler (NBL radar) and by turbulence sensors mounted on a 300-m tower.

The first purpose of this comparison was to obtain a calibration for radar reflectivity measurements, which are used to calculate C_n^2. The capability of Doppler radars to measure C_n^2 is well established, but a calibration of this type had not previously been attempted. Based on the results presented in Section 5.2.3, the calibration was a success. The radar and tower measurements of C_n^2 are well correlated with a correlation coefficient of 0.83. The relative uncertainty in the calibration based on the scatter in the data is 14%. As demonstrated in the Appendix, approximately half of the 3.53 dB scatter is attributable to

sampling uncertainty. Other factors that contributed to the scatter include the separation between the tower and the radar and the fact that the radar signal processing program at times improperly identified the clear-air return in the Doppler velocity spectrum.

The reflectivity calibration determined in this analysis should generally be applicable to cases other than the convective planetary boundary layer and at sites other than the Boulder Atmospheric Observatory (BAO). However, if the radar is set up to use a much longer pulse than was used in this study, then the turbulence may not fill the pulse volume. This is especially true above the boundary layer and in the stable boundary layer where the turbulence may be confined to narrow layers. In these cases, it is necessary to estimate the fraction of the radar scattering volume that is turbulent (see Cohn, 1995).

The second purpose of the radar-tower comparison was to investigate the use of radars to measure velocity statistics. I first demonstrated the filtering imposed on the velocity fluctuations measured by the radar as a result of the space-and-time averaging that is inherent in the radar sample. These effects must be accounted for in estimates of second- and higher-order velocity statistics computed from the velocity time series measured by the radar. I derived a transfer function that can be applied to the spectra computed from time series of radar-measured vertical velocities to compensate for the filters. I then modified a technique that uses the spectral width measured by the radar to deduce the small-scale velocity structure that is unresolved by the radar velocity measurement, thereby allowing the radar to provide estimates of the turbulent kinetic energy dissipation rate, or alternatively, C_u^2. I made the modification to account for the broadening of the radar beam resulting from temporal averaging.

I compared the estimates of C_u^2 deduced by the radar technique to the measurements of C_u^2 obtained on the tower. This comparison yielded only moderate correlation, with a correlation coefficient of 0.72. An error analysis showed that sampling uncertainty accounts for most of the scatter. This analysis also showed large uncertainties in the radar C_u^2 measurements. This result points out the difficulty in obtaining second-order velocity statistics from the radar. Part of the problem is due to the way in which the Doppler spectral moments are calculated. Improvements in the accuracy of the moments may result from implementing more sophisticated signal processing algorithms than are currently used today. The NOAA/Environmental Technology Laboratory (ETL) recently formed a task force to address this question.

The averaging of returns from a large number of radar pulses was once a necessity because of computing limitations, but today it is merely a matter of convenience. Therefore, in Chapter 6 I reported the results of three separate sensitivity studies. In each study, I varied one of the three primary signal processing parameters. The purpose of these experiments was twofold: first, I wanted to test the radar equations used to derive C_n^2 and C_u^2 for correct responses to changes in the parameters and, second, I wanted to see if the parameter settings traditionally used for mean wind profiling could be adjusted to improve radar performance for turbulence measurements.

I observed an improvement in signal-to-noise ratio (SNR) when the number of coherent integrations increased. This improvement occurred because of the way in which SNR is calculated in the radar processing program and should not be construed as having resulted from a change in the coherence time of the atmosphere. The radar reflectivity equation used in this memorandum properly accounts for the relationship between coherent integration and SNR.

Changes to the distribution of spectral widths observed by the radar occurred when the velocity resolution was changed and when the dwell time was altered. The radar C_u^2 equation I used should account for the dwell-time effect, but I could not verify this hypothesis because wind-speed data were not available for the sensitivity studies. The velocity resolution factors into the minimum width that can be resolved in the Doppler velocity spectrum. In Fig. 6.8, the widths most noticeably affected are less than about 0.75 m s^{-1}, suggesting that there is a wind-speed dependence to the velocity resolution effect as well.

The results presented in Chapter 6 indicate that improvements in the accuracy and sensitivity of the first and second Doppler velocity spectral moments occur when the velocity resolution increases. I showed that lack of resolution in the Doppler velocity spectrum is partly responsible for the negative bias observed in the frequency distributions of vertical velocity measured in convection. In addition, I observed a factor-of-four improvement in the minimum resolvable spectral width when the velocity resolution was increased by a factor of four.

For turbulence measurements, the primary result of increasing the dwell time (e.g., through an increase in the number of incoherent integrations) is to decrease the range of velocity scales resolved by the first moment and thereby increase the unresolved variance (i.e., increase the spectral width). Because of the large uncertainties associated with diagnosing the turbulence contribution to spectral width, this result is undesirable. It is, therefore, my recommendation that the time allotted for incoherent integration be used either to increase the velocity resolution or to decrease the dwell time.

Finally, the usefulness of Doppler wind-profiling radars is enhanced when they are deployed as part of a suite of instruments. An example is the Department of Energy's Atmospheric Radiation Measurement (ARM) Program, in which scientists are using a wide array of ground-based and airborne sensors along with multiple radars operating at different frequencies (Stokes and Schwartz, 1994). Programs such as this will provide the data necessary to further evaluate radar techniques for measuring turbulence.

ACKNOWLEDGMENTS

I would like to express my deepest appreciation to all who have contributed to this work: J. Brasseur, D. Thomson, J. Wyngaard, and G. Young, all of The Pennsylvania State

University; C. Fairall, E. Gossard, J. Jordan, R. Lataitis, W. Neff, R. Strauch, and R. Weber, all of NOAA/ETL. In addition, I thank retired NOAA employee R. Lawrence for his assistance with numerical integrations and S. Abott, J. Leach, C. Russell, and N. Szczepczynski for deploying and maintaining the radar and tower instruments.

Funding for this research was provided by the Department of Energy Atmospheric Radiation Measurement Program, the NOAA Climate and Global Change Program, and the Office of Naval Research Marine Boundary-Layers Program.

REFERENCES

Angevine, W.M., 1996: Errors in mean vertical velocities measured by boundary layer wind profilers. *J. Atmos. Ocean. Technol.*, submitted.

Angevine, W.M., S.K. Avery, W.L. Ecklund, and D.A. Carter, 1993a: Fluxes of heat and momentum measured with a boundary-layer wind profiler radar-radio acoustic sounding system. *J. Appl. Meteor.*, **32**, 73–80.

Angevine, W.M., S.K. Avery, and G.L. Kok, 1993b: Virtual heat flux measurements from a boundary-layer profiler-RASS compared to aircraft measurements. *J. Appl. Meteor.*, **32**, 1901–1907.

Angevine, W.M., A.B. White, and S.K. Avery, 1994: Boundary layer depth and entrainment zone characterization with a boundary layer profiler. *Bound.-Layer Meteor.*, **68**, 375–385.

Angevine, W.M., W.L. Clark, and J.M. Warnock, 1996: Entrainment velocity and vertical velocity measurements in convective boundary layers with a triangle of wind profilers. *Bound.-Layer Meteor.*, submitted.

Ashkenazy, J., P. Perlmutter, and D. Treves, 1983: A modular approach for the design of microstrip array antennas. *IEEE Trans. Anten. Prop.*, **AP-31**, 190–193.

Balsley, B.B., and K.S. Gage, 1982: On the use of radars for operational wind profiling. *Bull. Amer. Meteor. Soc.*, **63**, 1009–1018.

Batchelor, G.K., 1956: *The Theory of Homogeneous Turbulence*. Cambridge University Press, Cambridge, 197 pp.

Battan, L.J., 1973: *Radar Observation of the Atmosphere.* University of Chicago Press, Chicago, 323 pp.

Bendat, J.S., and A.G. Piersol, 1986: *Random Data: Analysis and Measurement Procedures.* John Wiley & Sons, Inc., New York, 566 pp.

Burk, S.D., 1980: Refractive index structure parameters: Time-dependent calculations using a numerical boundary-layer model. *J. Appl. Meteor.*, **19**, 562–576.

Burk, S.D., and W.T. Thompson, 1989: A vertically nested regional numerical weather prediction model with second-order closure physics. *Mon. Wea. Rev.*, **117**, 2305–2324.

Caughey, S.J., and S.G. Palmer, 1979: Some aspects of turbulence structure through the depth of the convective boundary layer. *Quart. J. Roy. Meteor. Soc.*, **105**, 811–827.

Chadwick, R.B., 1986: Wind profiler demonstration system. Handbook of MAP, Vol. 20, June 1986, URSI/SCOPTEP Workshop on Technical and Scientific Aspects of MST Radar, 336–337.

Cohn, S.A., 1995: Radar measurements of turbulent eddy dissipation rate in the troposphere: A comparison of techniques. *J. Atmos. Oceanic Technol.*, **12**, 85–95.

Corrsin, S., 1951: On the spectrum of isotropic temperature fluctuations in isotropic turbulence. *J. Appl. Phys.*, **22**, 469–473.

Coulter, R.L., and M.L. Wesley, 1980: Estimates of surface heat flux from sodar and laser scintillation measurements in the unstable boundary layer. *J. Appl. Meteor.*, **19**, 1209–1222.

Davidson, K.L., T.M. Houlihan, C.W. Fairall, and G.E. Schacher, 1978: Observation of the temperature structure parameter, C_T^2, over the ocean. *Bound.-Layer Meteor.*, **19**, 453–469.

Davies-Jones, R., 1993: Useful formulas for computing divergence, vorticity, and their errors from three or more stations. *Mon. Wea. Rev.*, **121**, 713–725.

Deardorff, J.W., 1970: Convective velocity and temperature scales for the unstable planetary boundary layer and for Rayleigh convection. *J. Atmos. Sci.*, **27**, 1211–1213.

Deardorff, J.W., 1974: Three-dimensional numerical study of turbulence in an entraining mixed layer. *Bound.-Layer Meteor.*, **7**, 199–206.

Deardorff, J.W., 1979: Prediction of convective mixed-layer entrainment for realistic capping inversion structure. *J. Atmos. Sci.*, **36**, 424–436.

Doviak, R.J., and D.S. Zrnić, 1984: *Doppler Radar and Weather Observations.* Academic Press, Orlando, 458 pp.

Druilhet, A., J.P. Frangi, D. Guedalia, and J. Fontan, 1983: Experimental studies of the turbulence structure parameters of the convective boundary layer. *J. Clim. Appl. Meteor.*, **22**, 594–608.

Ecklund, W.L., D.A. Carter, and B.B. Balsley, 1988: A UHF wind profiler for the boundary layer: Brief description and initial results. *J. Atmos. Ocean. Tech.*, **5**, 432–441.

Ecklund, W.L., P.E. Johnston, W.L. Clark, J.M. Warnock, T.E. VanZandt, and K.S. Gage, 1995: Scattering from clear air, precipitation, and biological targets: Multiple frequency profiler studies. *Proceedings, 7th Conference on MST Radar*, Hilton Head Island, South Carolina, October, 1995.

Frisch, A.S., and S.F. Clifford, 1974: A study of convection capped by a stable layer using Doppler radar and acoustic echo sounders. *J. Atmos. Sci.*, **31**, 1622–1628.

Fairall, C.W., 1984: Wind shear enhancement of entrainment and refractive index structure parameter at the top of a turbulent mixed layer. *J. Atmos. Sci.*, **41**, 3472–3484.

Fairall, C.W., 1987a: Similarity theories and microturbulence in the atmospheric mixed layer. *Dynamics of the Oceanic Surface Mixed Layer*, P. Muller and D. Henderson, Eds., University of Hawaii Publication, 265–290.

Fairall, C.W., 1987b: A top-down and bottom-up diffusion model of C_T^2 and C_Q^2 in the entraining convective boundary layer. *J. Atmos. Sci.*, **44**, 1009–1017.

Fairall, C.W., 1991: The humidity and temperature sensitivity of clear-air radars in the convective boundary layer. *J. Appl. Meteor.*, **30**, 1064–1074.

Fairall, C.W. and S.E. Larsen, 1986: Inertial dissipation methods and turbulent fluxes at the air-ocean interface. *Bound.-Layer Meteor.*, **34**, 287–301.

Fairall, C.W., R. Markson, G.E. Schacher and K.L. Davidson, 1980: An aircraft study of turbulence dissipation and temperature structure parameter in the unstable marine atmospheric boundary layer. *Bound.-Layer Meteor.*, **19**, 453–469.

Fairall, C.W., A.B. White, J.B. Edson, and J.E. Hare, 1996: Integrated shipboard measurements of the marine boundary layer. *J. Atmos. Ocean. Technol.*, in press.

Forbes, G.S., and Carroll, III, L.A., 1987: Initial results from the Penn State wind profiler in MIST/SPACE. *Vaisala News*, No. 111/112, 20–23.

Frisch, A.S., and S.F. Clifford, 1974: A study of convection capped by a stable layer using Doppler radar and acoustic echo sounders. *J. Atmos. Sci.*, **31**, 1622–1628.

Fritschen, L.J., and L.W. Gay, 1979: *Environmental Instrumentation.* Springer-Verlag, New York, pp. 2–9.

Gage, K.S., J.R. McAfee, D.A. Carter, W.L Ecklund, A.C. Riddle, G.C. Reid, and B.B. Balsley, 1991: Long-term mean vertical motion over the tropical Pacific: Wind-profiling Doppler radar measurements. *Science*, **254**, 1771–1773.

Gaynor, J.E., and L. Kristensen, 1986: Errors in second moments estimated from monostatic Doppler sodar winds. Part II: Application to field measurements. *J. Atmos. Ocean. Technol.*, **3**, 529–534.

Ghebrebrhan, O., 1990: Full decoding of truncated ranges for ST/MST radar applications. *IEEE Trans. Geosci. Remote Sens.*, **28**, 14–18.

Gorelick, A.G., and Yu. V. Mel'nichuk, 1963: Radar study of dynamic process in the atmosphere. *Tr. Vses. Nav. Meteor. Souesh.*, No. 5.

Gorelick, A.G., and Yu. V. Mel'nichuk, 1968: A new method for measuring dissipation rate of turbulence in clouds and precipitation using conventional radar. *Proc. Third All-Union USSR Radar Meteor. Conf.*, 150–156.

Gossard, E.E., 1990: Radar research on the atmospheric boundary layer. *Radar in Meteorology,* D. Atlas, Ed., Amer. Meteor. Soc., Boston, 447–527.

Gossard, E.E., 1994: Measurement of cloud droplet size spectra by Doppler radar. *J. Atmos. Ocean. Technol.*, **11**, 712–726.

Gossard, E.E., and R.G. Strauch, 1983: *Radar Observation of Clear Air and Clouds.* Elsevier, Amsterdam, 280 pp.

Gossard, E.E., and R.G. Strauch, 1989: Further guide for the retrieval of drop-size distributions in water clouds with a ground-based clear-air-sensing Doppler radar. NOAA Environmental Research Laboratories, 48 pp.

Gossard, E.E., R.B. Chadwick, R.T. Detman, and J. Gaynor, 1984: Capability of surface-based, clear-air Doppler radar for monitoring meteorological structure of elevated layers. *J. Clim. Appl. Meteor.*, **23**, 474–490.

Gossard, E.E., D.C. Welsh, and R.G. Strauch, 1990: Radar-measured height profiles of C_n^2 and turbulence dissipation rate compared with radiosonde data during October 1989 at Denver. NOAA Tech. Report ERL 442-WPL 63, Environmental Research Laboratories, 115 pp.

Gossard, E.E., R.G. Strauch, B.B. Stankov, and D.E. Wolfe, 1995: Measurement of property gradients and turbulence aloft with ground-based Doppler radars. NOAA Tech. Memo. ERL 453-ETL 67, NOAA Environmental Technology Laboratory, Boulder, CO, 31 pp.

Green, J.L., K.S. Gage, T.E. VanZandt, W.L. Clark, J.M. Warnock, and G.D. Nastrom, 1988: Observations of vertical velocity over Illinois by the Flatland radar. *Geophys. Res. Lett.*, **15**, 269–272.

Hardy, K.R., D. Atlas, and K.M. Glover, 1966: Multiwavelength backscatter from the clear atmosphere. *J. Geophys. Res.*, **71**, 1537–1552.

Harris, F.J., 1978: On the use of windows for harmonic analysis with the discrete Fourier transform. *Proc. IEEE*, **66**, 51–83.

Haugen, D.A., J.C. Kaimal, C.J. Readings, and R. Rayment, 1975: A comparison of balloon-borne and tower-mounted instrumentation for probing the atmospheric boundary layer. *J. Appl. Meteor.*, **14**, 540–545.

Hildebrand, P.H., and R.S. Sekhon, 1974: Objective determination of the noise level in Doppler spectra. *J. Appl. Meteor.*, **13**, 808–811.

Hill, R.J., 1996: Corrections to Taylor's frozen turbulence approximation. *Atmos. Res.*, **40**, 153–175.

Hocking, W.K., 1985: Meausrement of turbulent eddy dissipation rates in the middle atmosphere by radar techniques: A review. *Radio Sci.*, **20**, 1403–1422.

Jordan, J.R., 1995: Personal communication.

Kaimal, J.C., and J.J. Finnigan, 1994: *Atmospheric Boundary Layer Flows: Their Structure and Measurement.* Oxford University Press, New York, 289 pp.

Kaimal, J.C., J.C. Wyngaard, D.A. Haugen, O.R. Coté, Y. Izumi, S.J. Caughey, and C.J. Readings, 1976: Turbulence structure in the convective boundary layer. *J. Atmos. Sci.*, **33**, 2152–2169.

Kaimal, J.C., N.L. Abshire, R.B. Chadwick, M.T. Decker, W.H. Hooke, R.A. Kropfli, W.D. Neff, and F. Pasqualucci, 1982: Estimating the depth of the daytime convective boundary layer. *J. Appl. Meteor.*, **21**, 1123–1129.

Kaimal, J.C., S.F. Clifford, and R.J. Lataitis, 1989: Effect of finite sampling on atmospheric spectra, *Bound.-Layer Meteor.*, **47**, 337–347.

Kaimal, J.C., J.E. Gaynor, H.A. Zimmerman, and G.A. Zimmerman, 1990: Minimizing flow distortion errors in a sonic anemometer. *Bound.-Layer Meteor.*, **53**, 103–115.

Kohsiek, N., 1982: Measuring C_T^2, C_q^2, and C_{Tq} in the unstable surface layer, and relations to the vertical fluxes of heat and moisture. *Bound.-Layer Meteor.*, **24**, 89–107.

Kolmogorov, A.N., 1941: The local structure of turbulence in incompressible viscous fluid for very large Reynolds' numbers. *C.R. Acad. Sci. URSS*, **30**, 301–305.

Kristensen, L., 1971: The effect of aliasing, averaging and smoothing in digital spectrum analysis. *Statistical Methods and Instrumentation in Geophysics*, A.G. Kjelaas, Ed., Teknologisk Forlag, Oslo, 1–24.

Kuo, Y.-H., E.G. Donall, and M.A. Shapiro, 1987: Feasibility of short-range numerical weather prediction using observations from a network of profilers. *Mon. Wea. Rev.*, **115**, 2402–2427.

Kustas, W.P., and W. Brutsaert, 1987. Budgets of water vapor in the unstable boundary layer over rugged terrain. *J. Clim. Appl. Meteor.*, **26**, 607–620.

Labbitt, M., 1981: Coordinated radar and aircraft observations of turbulence. MIT Lincoln Laboratory Rep. ATC-108, Lexington, MA, 40 pp.

Lenschow, D.H., and B.B. Stankov, 1986: Length scales in the convective boundary layer. *J. Atmos. Sci.*, **43**, 1198–1209.

Lenschow, D.H., J.C. Wyngaard, and W.T. Pennell, 1980: Mean-field and second-moment budgets in a baroclinic, convective boundary layer. *J. Atmos. Sci.*, **37**, 1313–1326.

Lumley, J.L., and H.A. Panofsky, 1964: *The Structure of Atmospheric Turbulence*. John Wiley & Sons, Inc., New York, 239 pp.

Martner, B.E., D.B. Wuertz, B.B. Stankov, R.G. Strauch, E.R. Westwater, K.S. Gage, W.L. Ecklund, C.L. Martin, and W.F. Dabberdt, 1993: An evaluation of wind profiler, RASS, and microwave radiometer performance. *Bull. Amer. Meteor. Soc.*, **74**, 599–613.

Moeng, C.-H., and J.C. Wyngaard, 1984: Statistics of conservative scalars in the convective boundary layer. *J. Atmos. Sci.*, **41**, 3162–3169.

Moeng, C.-H., and J.C. Wyngaard, 1989: Evaluation of turbulent transport and dissipation closures in second-order modeling. *J. Atmos. Sci.*, **46**, 2311–2330.

Nastrom, G.D., and T.E. VanZandt, 1994: Mean vertical motions seen by radar wind profilers. *J. Appl. Meteor.*, **33**, 984–995.

Neff, W.D., 1975: Quantitative evaluation of acoustic echoes from the planetary boundary layer. Technical Report ERL 322-WPL, NOAA Environmental Research Laboratories, 34 pp.

Neff, W.D., C.W. King, J.R. Jordan, S.W. Abbott, J.L. Leach, L.K. Lewis, D. Welsh, L. Zhang, B. Weber, D. Wuertz, R. Fritz, J. Gaynor, D. Gregg, D. Ruffieux, C. Russell, S. Szczepczynski, A. White, J.M. Wilczak, D. Wolfe, J.P. Ye, S. Bernal, and S. Petrie, 1994: A multi-year observational study of atmospheric transport corridors and processes in California. Final Report to California Air Resources Board, Agreement No. A032-145, NOAA Environmental Technology Laboratory, Boulder, CO, 111 pp.

Nieuwstadt, F.T.M., 1984: The turbulent structure of the stable nocturnal boundary layer. *J. Atmos. Sci.*, **41**, 2202–2216.

Panofsky, H.A., 1962: Scale analysis of atmospheric turbulence at 2 meters. *Quart. J. Roy. Meteor. Soc.*, **88**, 57–69.

Panofsky, and J.A. Dutton, 1984: *Atmospheric Turbulence*. John Wiley & Sons, Inc., New York, 397 pp.

Peltier, L.J., and J.C. Wyngaard, 1995: Structure function parameters in the convective boundary layer from large-eddy simulation. *J. Atmos. Sci.*, **52**, 3641–3660.

Peters, G., H. Hinzpeter, and G. Baumann, 1985: Measurements of heat flux in the atmospheric boundary layer by sodar and RASS: A first attempt. *Radio Sci.*, **6**, 1555–1564.

Probert-Jones, J.R., 1962: The radar equation in meteorology. *Quart. J. Roy. Meteor. Soc.*, **88**, 485–495.

Ralph, F.M., 1995: Using radar-measured radial vertical velocities to distinguish precipitation scattering from clear-air scattering. *J. Atmos. Ocean. Technol.*, **12**, 257–267.

Röttger, J., 1988: The instrumental principles of MST radars and incoherent scatter radars and the configuration of radar system hardware. Lecture notes from the International School on Atmospheric Radar (E.S. Fukao, Ed.), November 24–28, 1988, Kyoto, Japan, 81 pp.

Russell, C.A., and J.R. Jordan, 1991: Portable clutter fence for UHF wind profiling radar. Preprints, *Seventh Symp. on Meteor. Obs. and Instrum. and Special Session on Laser Atmos. Studies*, Amer. Meteor. Soc., Boston, 152–156.

Seaman, N.L., 1992: Private communication.

Smith, S.D., R.J. Anderson, G.D. Hartog, D.R. Topham, and R.G. Perkin, 1983: An investigation of a Polyna in the Canadian Archipelagos, structure of turbulence and heat flux. *J. Geophys. Res.*, **88**, 2900–2910.

Srivastava, R.C., and D. Atlas, 1972: The effects of a finite radar pulse volume on turbulence measurements. *Preprints, 15th Radar Meteor. Conf.*, Amer. Meteor. Soc., Boston, 297–302.

Stauffer, D.R., and N.L. Seaman, 1994: Multiscale four-dimensional data assimilation. *J. Appl. Meteor.*, **33**, 416–434.

Stokes, G.M., and S.E. Schwartz, 1994: Atmospheric Radiation Measurement (ARM) Program: Programmatic background and design of the radiation testbed. *Bull. Amer. Meteorol. Soc.*, **75**, 1201–1221.

Tatarski, V.I., 1961: *Wave Propagation in a Turbulent Medium.* Dover Publications, Inc., New York, 285 pp.

Taylor, G.I., 1938: The spectrum of turbulence. *Proc. R. Soc. London Ser. A*, **164**, 476–490.

Tennekes, H. and A.G.M. Driedonks, 1981: Basic entrainment equations for the atmospheric boundary layer. *Bound.-Layer Meteor.*, **20**, 515–531.

Thomson, D.W., R.L. Coulter, and Z. Warhaft, 1978: Simultaneous measurements of turbulence in the lower atmosphere using sodar and aircraft. *J. Appl. Meteor.*, **17**, 723–734.

Tsuda, T., 1988: Data acquisition and processing. Lecture notes from the International School on Atmospheric Radar (E.S. Fukao, Ed.), November 24–28, 1988, Kyoto, Japan, 38 pp.

VanZandt, T.E., J.L. Green, K.S. Gage, and W.L. Clark, 1978: Vertical profiles of refractivity turbulence structure constant: Comparison of observations by the Sunset Radar with a new theoretical model. *Radio Sci.*, **13**, 819–829.

Vincent, R.A., and I.M. Reid, 1983: HF Doppler measurements of mesospheric gravity wave momentum fluxes. *J. Atmos. Sci.*, **40**, 1321–1333.

Wakasugi, K., Mizutani, A., Matsuo, M., Fukao, S., and Kato, S., 1986: A direct method for deriving drop-size distribution and vertical air velocities from VHF Doppler radar spectra. *J. Atmos. Ocean. Technol.*, **3**, 623–629.

Wakasugi, K., Balsley, B.B., and Clark, T.L., 1987: The VHF Doppler radar as a tool for cloud and precipitation studies. *J. Atmos. Ocean. Technol.*, **4**, 273–280.

Weber, B.L., D.B. Wuertz, R.G. Strauch, D.A. Merritt, K.P. Moaran, D.C. Law, D. van de Kamp, R.B. Chadwick, M.H. Ackely, M.F. Barth, N.L. Abshire, P.A. Miller, and T.W. Schlatter, 1990: Preliminary evaluation of the first NOAA Demonstration Network wind profiler. *J. Atmos. Ocean. Technol.*, **7**, 909–918.

Wesley, M.L., 1976: Combined effect of temperature and humidity fluctuations on refractive index. *J. Appl. Meteor.*, **15**, 43–49.

White, A.B., 1993: Mixing depth detection using 915-MHz radar reflectivity data. Preprint Vol., *Eighth Symp. on Observations and Instrumentation*, Amer. Meteor. Soc., Boston, 248–250.

White, A.B., and C.W. Fairall, 1991: Convective boundary layer structure observed during ROSE-I using the NOAA 915-MHz radar wind profiler. NOAA Tech. Memo. ERL WPL-205, NOAA Environmental Research Laboratories, 58 pp.

White, A.B., C.W. Fairall, and D.W. Thomson, 1991: Radar observations of humidity variability in and above the marine atmospheric boundary layer. *J. Atmos. Ocean. Technol.*, **8**, 639–658.

White, A.B., C.W. Fairall, A.S. Frisch, B.W. Orr, and J.B. Snider, 1996: Recent radar measurements of turbulence and microphysical parameters in marine boundary layer clouds. *Atmos. Res.*, **40**, 177–221.

Wilczak, J.M., R.G. Strauch, F.M. Ralph, B.L. Weber, D.A. Merritt, J.R. Jordan, D.E. Wolfe, L.K. Lewis, D.B. Wuertz, and J.E. Gaynor, 1995: Contamination of wind profiler data by migrating birds: Characteristics of corrupted data and potential solutions. *J. Atmos. Oceanic Technol.*, **12**, 449–467.

Willis, G.E., and J.W. Deardorff, 1974: A laboratory model of the unstable planetary boundary layer, *J. Atmos. Sci.*, **31**, 1297–1307.

Willis, G.E., and J.W. Deardorff, 1976: On the use of Taylor's translation hypothesis for diffusion in the mixed layer. *Quart. J. Roy. Meteor. Soc.*, **102**, 817–822.

Wyngaard, J.C., 1992: Atmospheric Turbulence. *Ann. Rev. Fluid Mech.*, **24**, 205–233.

Wyngaard, J.C., and O.R. Coté, 1971: The budgets of turbulent kinetic energy and temperature variance in the atmospheric surface layer. *J. Atmos. Sci.*, **28**, 190–201.

Wyngaard, J.C., and S.F. Clifford, 1977: Taylor's hypothesis and high frequency turbulence spectra, *J. Atmos. Sci.*, **34**, 922–929.

Wyngaard, J.C., and M.A. LeMone, 1980: Behavior of the refractive index structure parameter in the entraining convective boundary layer. *J. Atmos. Sci.*, **35**, 1573–1585.

Wyngaard, J.C., and R.A. Brost, 1984: Top-down and bottom-up diffusion of a scalar in the convective boundary layer. *J. Atmos. Sci.*, **41**, 102–112.

Wyngaard, J.C., Y. Izumi, and S.A. Collins, 1971a: Behavior of the refractive index structure parameter near the ground. *J. Opt. Soc. Am.*, **61**, 1646–1650.

Wyngaard, J.C., O.R. Coté, and Y. Izumi, 1971b: Local free convection, similarity, and the budgets of shear stress and heat flux. *J. Atmos. Sci.*, **28**, 1171–1182.

APPENDIX: ERROR ANALYSIS

In this appendix I investigate the different sources of uncertainty associated with the C_n^2 and C_u^2 measurements presented in Chapter 5. I classify these errors under two categories: random errors and systematic errors. Random errors are associated with the statistical variability of the atmosphere ("sampling uncertainty") and with particular elements of the techniques used to derive C_n^2 and C_u^2 ("random measurement uncertainty"). Systematic errors are associated with any instrument errors ("instrument uncertainty") and with other elements of the measurement techniques ("systematic measurement uncertainty"). Random errors contribute to the scatter shown in Figs. 5.9 and 5.16. Systematic errors contribute to the bias in the C_u^2 scatterplot (Fig. 5.16) and, in the case of C_n^2, to an error in the calibration constant derived from comparing radar and tower estimates of C_n^2 (Fig. 5.9).

A.1 Sampling Uncertainty

The sampling uncertainty can be estimated using the time-averaging formula (e.g., Lumley and Panofsky, 1964)

$$\frac{T}{\Im} = \frac{2\overline{f'^2}}{\sigma^2}, \tag{A.1}$$

where $\Im$ is the integral time scale of a stationary random function of time, σ^2 is the ensemble variance of the time average f_T (for averaging period T) about the ensemble mean $\overline{f}$, and $\overline{f'^2}$ is the ensemble variance of f about $\overline{f}$. Here we are concerned with the sampling uncertainty associated with two measurements taken at the same time but separated by a distance δ. If $\delta = 0$, such that the radar and tower sample approximately the same air, then sampling uncertainty is not an issue. For $\delta > 0$, the variance of interest becomes

$$\overline{f'^2} = \overline{[f'(r) - f'(r+\delta)]^2}. \tag{A.2}$$

Assuming local homogeneity,

$$\overline{[f'(r+\delta)]^2} = \overline{[f'(r)]^2}, \tag{A.3}$$

such that

$$\overline{f'^2} = 2\{\overline{[f'(r)]^2} - \overline{f'(r)f'(r+\delta)}\}. \tag{A.4}$$

The right-hand term in the brackets is the correlation function, $R(\delta)$. To proceed, I assume that $R(\delta)$ is given by

$$R(\delta) = \overline{f'(r)^2}\exp(-\delta/\lambda_l), \tag{A.5}$$

where λ_l is the integral length scale. This expression has the correct property that when normalized by the variance, $R(\delta)$ integrates to give λ_l. However, the correlation may drop off much faster than in (A.5), especially if the separation is not aligned with the mean wind. In this case it is difficult to determine the appropriate integral length scale.

Assuming that (A.5) is valid, (A.4) can be rewritten as

$$\overline{f'^2} = 2\overline{[f'(r)]^2}\,[1 - \exp(-\delta/\lambda_l)]. \tag{A.6}$$

Substituting (A.6) in (A.1) and letting $\Im \approx \lambda_l / U$, we arrive at

$$\frac{\sigma^2}{\overline{[f'(r)]^2}} = \frac{4\lambda_l[1 - \exp(-\delta/\lambda_l)]}{UT}. \tag{A.7}$$

In the limit of $\delta \rightarrow 0$, (A.7) gives the expected result that the sampling uncertainty becomes negligible. For $\delta >> \lambda_l$, (A.7) gives twice the sampling uncertainty that would be calculated in (A.1). This result makes sense because for large separations the two instruments sample volumes of air that are statistically independent.

I first apply (A.7) to the C_n^2 analysis. For λ_l, I use the integral length scale for scalar variances in the convective boundary layer (CBL) given by Lenschow and Stankov (1986):

$$\lambda_l = \lambda_{\theta^2} = z_i\left(\frac{z}{z_i}\right)^{1/2}. \tag{A.8}$$

The actual integral length scale for C_n^2 may be different because structure functions by definition neglect the largest scales in the flow. With z = 250 m and z_i = 1400 m, $\lambda_l \approx$ 600 m. For δ = 200 m, U = 4.1 m s^{-1}, and T = 14 min, taking the square root of (A.7) gives a sampling uncertainty of 44%. A factor of 1.44 converts to 1.58 dB. The scatter observed in Fig. 5.9 was 3.53 dB, or a factor of 2.25. The contribution of sampling uncertainty to the scatter is found by taking the ratio of the squares of these factors. Based on this analysis, sampling uncertainty accounts for roughly half of the scatter in Fig. 5.9. If I had used 1-h averages instead of 14-min averages, the sampling uncertainty calculated with (A.7) would have improved to 21%.

For the C_u^2 analysis, I used the integral length scale for the horizontal velocity variances in the CBL given by Lenschow and Stankov (1986):

$$\lambda_l = \lambda_{v_H^2} = 0.3 z_i, \tag{A.9}$$

with z_i = 1400 m, $\lambda_l \approx$ 420 m. The same values of δ and T used above apply to the C_u^2 analysis, but here U = 4.5 m s^{-1}. Inserting these values in (A.7) gives a sampling uncertainty of 41%. The scatter in Fig. 5.16 is 1.65 dB, or a factor of 1.46. Based on this analysis, sampling uncertainty accounts for nearly all (93%) of the scatter in the C_u^2 comparison.

A.2 Radar C_n^2

Most of the uncertainty in the radar C_n^2 measurement is associated with the radar reflectivity equation [see (4.25)]. Additional uncertainty comes from the inertial subrange requirement used to derive (4.14). To estimate the error in η in terms of the uncertainty in the radar parameters, I use the standard error approach (e.g., Fristchen and Gay, 1979), where the uncertainty in a function $G(x,y)$ is expressed as

$$\delta G = \frac{\partial G}{\partial x}\delta x + \frac{\partial G}{\partial y}\delta y. \tag{A.10}$$

Equation (A.10) can be simplified using the rules of logarithmic differentiation. For example, if we let $G = x/y$, then taking the natural logarithm of both sides gives us

$$\ln G = \ln x - \ln y. \tag{A.11}$$

By differentiating logarithmically, we obtain

$$\begin{aligned} \frac{\partial \ln G}{\partial x} &= \frac{\partial \ln x}{\partial x} = \frac{1}{x} \\ \frac{\partial \ln G}{\partial y} &= -\frac{\partial \ln y}{\partial y} = -\frac{1}{y}. \end{aligned} \tag{A.12}$$

Then, using the identity

$$\frac{\partial \ln G}{\partial G} = \frac{1}{G} \tag{A.13}$$

and the chain rule, we can rewrite (A.10) as

$$\frac{\delta G}{G} = \frac{\delta x}{x} - \frac{\delta y}{y}. \tag{A.14}$$

Put into words, (A.14) says that the relative uncertainty in G is given by the sum of the relative uncertainties in x and y. The sign of the individual terms is important if one or more like terms are to be combined. If x and y are independent variables and δx and δy are uncorrelated, then the most probable uncertainty in G is given by the sum of the squares of the individual terms:

$$\frac{\delta G}{G} = \left[\left(\frac{\delta x}{x}\right)^2 + \left(\frac{\delta y}{y}\right)^2\right]^{1/2}. \tag{A.15}$$

Because (4.25) involves only products, it is well-suited to this approach. Following the above example, I write an equation for the relative uncertainty in radar reflectivity,

$$\frac{\delta \eta}{\eta} \approx \frac{\delta T_{rx}}{T_{rx}} + \frac{2\delta R}{R} + \frac{\delta \mathrm{SNR}}{\mathrm{SNR}} - \frac{\delta P_t}{P_t} - \frac{2\delta(\Delta R)}{\Delta R}, \tag{A.16}$$

where the uncertainties of the constants and beam elevation angle in (4.25) are assumed to be negligible. All of the errors on the right-hand side of (A.16) are instrument errors, except for the relative uncertainty in the signal-to-noise ratio (SNR), which is a random measurement error.

The relative uncertainty in T_{rx} is estimated to be 10% and is based on the operating specifications reported by the manufacturers of the different receiver components. Radar engineers have also calibrated the mean noise temperature of the receiver in the laboratory by disconnecting the antenna and using a (calibrated) noise diode in its place to inject a signal. This noise calibration becomes uncertain in an operational sense because of losses in the antenna and the addition of sky noise. I neglected sky noise in the radar reflectivity equation (see Section 4.5), because in the mean and at 915 MHz, the sky is much colder than the receiver. On the other hand, when the beam is pointed directly at a radio star and/or when there is increased sunspot activity, the sky noise temperature at 915 MHz could approach 200 K (Doviak and Zrnić, 1984). Because in (4.21) T_s is multiplied by α, I estimate the combined error in T_{rx} to be $0.24\times200 \pm 15 = 48 \pm 15$ K. Therefore, the relative uncertainty in T_{rx} for any one particular radar reflectivity measurement could be as high as 42%.

The relative uncertainty in R translates to how accurately the delay time between the transmitter and the antenna is known. This delay is measured at each radar site using a delay line and an oscilloscope. The estimated uncertainty is ±10 m. However, an additional delay

occurs in the receiver, which increases the uncertainty by a factor of two. Therefore, I estimate the relative uncertainty in R at R = 278 m to be 7%.

The relative uncertainty in ΔR translates into the uncertainty in τ since $\Delta R = c\tau/2$. The relative uncertainty in τ is quite small – on the order of 1%. However, the transmitter does not produce a perfectly square pulse, so the edge effects may result in additional uncertainty. For this reason, I estimate the relative uncertainty in ΔR to be approximately 10%.

Unfortunately, the average peak power in the pulses transmitted by the National Oceanic and Atmospheric Administration (NOAA) 915-MHz boundary layer radar/wind profiler (NBL radar) was not measured during the Boulder Atmospheric Observatory (BAO) radar calibration experiment. Instead, I assumed a nominal value of 500 W. The transmit power varies over the life of the transmitter and is also slightly temperature dependent. For the transmitters used with the NBL radars, the peak pulse power varies from about 300 to 700 W. Therefore, the relative uncertainty in P_t is 40%.

The relative uncertainty in the SNR can be analyzed in terms of the individual uncertainties in the signal power, S, and noise power, N:

$$\frac{\delta \mathrm{SNR}}{\mathrm{SNR}} = \frac{1}{\mathrm{SNR}} \delta\left(\frac{S}{N}\right) = \left(\frac{\delta S}{S} \pm \frac{\delta N}{N}\right). \qquad \textbf{(A.17)}$$

Referring to Fig. 4.2, determining the relative uncertainty of the noise power is the same as determining the relative uncertainty in P_N because noise power is calculated by multiplying P_N by a constant (i.e., the length of the spectrum). The uncertainty in P_N is given by

$$\delta P_N = \frac{\sigma_N}{\sqrt{n_f - n_p}}, \qquad \textbf{(A.18)}$$

where n_p is the number of spectral points used to define the signal peak. However, as shown in Section 4.2.4, incoherent integration (spectral averaging) reduces the intensity of noise fluctuations such that $\sigma_N = P_N/n_s^{1/2}$. As a result, the relative uncertainty in noise power is given by

$$\frac{\delta N}{N} = \frac{\delta P_N}{P_N} = \pm \frac{1}{\sqrt{n_s(n_f - n_p)}}. \qquad \textbf{(A.19)}$$

In this case, n_s = 30 and n_f = 64. If I take n_p to be 5, then the relative uncertainty of the noise power is roughly 2%.

Estimating the error in the signal power is not as straightforward because the shape of the curve under which the area is calculated varies from spectrum to spectrum, and, in general, is more complicated than the rectangle used in the noise power calculation. Referring to Fig. 4.2, the signal power is given approximately by

$$S \approx \frac{1}{2} n_p \Delta v \, (P_s - P_N). \tag{A.20}$$

Therefore, the relative uncertainty in S is given by

$$\frac{\delta S}{S} \approx \frac{1}{2} n_p \Delta v \left(\frac{\delta P_s}{S} \pm \frac{\delta P_N}{S} \right). \tag{A.21}$$

To calculate the uncertainty in P_S, I assume that the fluctuations in the signal are comparable to the fluctuations in the noise:

$$\delta P_S \approx \frac{\sigma_N}{\sqrt{n_p}} = \frac{P_N}{\sqrt{n_p n_s}}. \tag{A.22}$$

Substituting (A.22) in (A.21) and using (A.19) along with the identity $S = (\mathrm{SNR}) P_N n_f (\Delta v)$, I obtain

$$\frac{\delta S}{S} \approx \frac{n_p}{2 n_f \sqrt{n_s}\ \mathrm{SNR}} \left(\frac{1}{\sqrt{n_p}} \pm \frac{1}{\sqrt{n_f - n_p}} \right). \tag{A.23}$$

For SNR > -8 dB, the relative error is less than 3%. There is also an uncertainty associated with determining the endpoints where the signal crosses the noise floor, but these regions do not contribute significantly to the signal power for reasonable values of SNR. Using (A.17), the relative uncertainty in SNR becomes 5%. Summing the squares of the other errors in (A.16), I estimate the instrument error associated with the radar to be 63%.

A.3 Tower C_n^2

The first error I consider for the tower C_n^2 measurement is the separation between the two turbulence sensors, since the fluctuations measured by both instruments were used to calculate the refractivity spectrum. This error results in underestimating the high-frequency contributions to the temperature-humidity cospectrum for $f \geq U/(2\pi\delta_s)$, where $\delta_s = 1$ m is the separation between the two instruments. For the spectra used to compute C_n^2, the average

wind speed was 4.1 m s^{-1}. In this case, the separation becomes important for frequencies larger than about 0.65 Hz. To identify the inertial subrange in the N spectra, I used only the portion of the spectra between 0.1 and 0.5 Hz. Therefore, I can neglect the instrument separation in my computations of C_n^2.

I next consider the error associated with inaccuracies in Taylor's hypothesis and anisotropy in the inertial subrange. Wyngaard and Clifford (1977) give factors to correct scalar and velocity spectra for these effects. For scalars, the factor is given by

$$F_N = \left(1 - \frac{1}{9}\frac{\sigma_u^2}{\overline{u}^2} + \frac{1}{3}\frac{\sigma_v^2}{\overline{u}^2} + \frac{1}{3}\frac{\sigma_w^2}{\overline{u}^2} \right)^{-1}. \qquad \textbf{(A.24)}$$

I used the 15-min variances and mean wind speeds measured by the Applied Technologies, Inc. sonic anemometer (ATI) in (A.24). This application is not strictly correct because the 15-min averages do not necessarily represent ensemble statistics. In addition, the variances measured by the ATI were often suspect because of high-frequency contamination caused by noise spikes (see Kaimal and Finnigan, 1994). To combat this problem, I used the median variances and average wind speed from the 96 samples used in the C_n^2 analysis. With σ_u^2 = 0.90 m^2 s^{-2}, σ_v^2 = 1.05 m^2 s^{-2}, σ_w^2 = 1.20 m^2 s^{-2}, and $\overline{u}$ = 4.1 m s^{-1}, F_N = 0.96, which means that the tower values of C_n^2 are overestimated by 4%. I classify this error as a systematic measurement error.

In the interest of comparing these variances with those measured in previous studies, I use the mixed-layer scaling described in Section 3.1.2. Here, the appropriate velocity scale is w_*. To use (3.11) I linearly extrapolate the heat flux measured by the ATI at 250 m down to the surface, assuming the flux profile crosses zero at a height of 1400 m. The average heat flux measured by the ATI is 150 W m^{-2}, giving a value of 180 W m^{-2} for the surface heat flux. With $T \simeq 300$ K and $z_i \simeq 1400$ m, w_* = 2.0 m s^{-1}. The median velocity variances measured by the ATI, when nondimensionalized by w_*, are in good agreement with the observations of Kaimal et al. (1976) and Caughey and Palmer (1979).

Another uncertainty in the tower C_n^2 measurements is due to the uncertainty of fitting a line to the inertial subrange in the refractivity spectra, which I classify as a random measurement uncertainty. The normalized error in a spectral estimate is given by (Lumley and Panofsky, 1964):

$$\frac{\delta S(f)}{S(f)} = \left(\frac{\sqrt{2}}{T\Delta f} \right)^{1/2}. \qquad \textbf{(A.25)}$$

Here, the relevant frequency interval is 0.4 Hz, because this corresponds to the range of

frequencies I used to determine the line. The relative uncertainty associated with finding the inertial subrange is then 7%.

Instrument errors also contribute to the uncertainty in the tower C_n^2 measurements. For example, long-term comparisons of humidity fluctuations measured by the Ophir infrared hygrometer and a psychrometer have shown that the Ophir hygrometer underestimates humidity fluctuations on average by 3% (Fairall et al., 1996). The resulting error in C_Q^2 or C_n^2 is 6%. The two most important systematic errors for the sonic thermometer are sensitivities to humidity and to the wind component normal to the path (which for the temperature measurement is the same path used to measure vertical velocity). With the ATI, the latter effect is compensated for in the real-time processing of the temperature signals. But, as pointed out by Kaimal and Finnigan (1994), both errors are negligible under daytime unstable conditions when temperature fluctuations are large. A limitation of the frequency response for measuring temperature fluctuations is imposed by the line averaging occurring along the acoustic path. The range for useful measurements is given by λ (or $\overline{u}/f$) > $2\pi \times 15$ cm (Kaimal and Finnigan, 1994), which in this case corresponds to $f < 4.0$ Hz. The range of frequencies used to determine C_n^2 is well within this range.

A.4 Tower C_u^2

The sources of uncertainty for the tower C_u^2 measurements are similar to those described above for the tower C_n^2 measurements. For instance, the same uncertainty in finding the inertial subrange applies here because the same approach was used to analyze both the velocity and refractivity spectra. However, the factor to account for inaccuracies in Taylor's hypothesis and anisotropy in the inertial subrange for velocity spectra is slightly different and is given by (Wyngaard and Clifford, 1977):

$$F_u = \left(1 - \frac{1}{9}\frac{\sigma_u^2}{\overline{u}^2} + \frac{2}{3}\frac{\sigma_v^2}{\overline{u}^2} + \frac{2}{3}\frac{\sigma_w^2}{\overline{u}^2} \right)^{-1}. \qquad \textbf{(A.26)}$$

To evaluate (A.26) I used the median variances and average wind speed from the C_u^2 analysis. With $\sigma_u^2 = 0.93$ m^2 s^{-2}, $\sigma_v^2 = 0.97$ m^2 s^{-2}, $\sigma_w^2 = 1.06$ m^2 s^{-2}, and $\overline{u} = 4.5$ m s^{-1}, $F_u = 0.94$, suggesting that on average, the ATI overestimated C_u^2 by 6%.

The same limitation to the frequency response of the sonic thermometer applies to the sonic anemometer because the path lengths are identical for all three axes. Therefore, the range of frequencies used to determine C_u^2 is well outside the range of contaminated frequencies. However, the streamwise and cross-stream velocity components u and v are also affected by the separation between the two horizontal paths. The range of useful wavelengths becomes $\lambda > 2\pi \times 37$ cm (Kaimal and Finnigan, 1994), which in this case corresponds to

$f < 1.6$ Hz. Thus, the C_u^2 estimates should still be unaffected by the spatial averaging characteristics of the ATI probe. Flow distortion and transducer shadowing effects are compensated for in real time (Kaimal and Finnigan, 1994). The algorithms used to correct for these errors are based on calibration tests performed in wind tunnels and in the atmosphere (Kaimal et al., 1990).

A.5 Radar C_u^2

The total uncertainty in radar measurements of C_u^2 is attributable to uncertainties contained in the formulas used to correct the spectral width for the effects of finite beamwidth and spatial and temporal averaging, as well as the uncertainty in σ_t^2 calculated from the Doppler velocity spectrum. Considering the latter, the normalized random error for an estimate of the variance is given approximately by (Bendat and Piersol, 1986):

$$\varepsilon_r[\sigma_x^2] \approx \left(\frac{N}{2}\right)^{-1/2}, \tag{A.27}$$

where N is the number of points used to estimate the variance. Here, the relevant N is given by the product $n_p n_s$. If I assume $n_p = 5$, then the relative uncertainty in σ_t^2 is approximately 12%. There is an additional uncertainty in the second moment associated with determining the endpoints where the signal crosses the noise floor, but this error is negligible for reasonable values of SNR.

Next, I consider the correction for finite beamwidth. Using (5.22), the relative uncertainty in σ_a can be expressed as

$$\frac{\delta\sigma_a}{\sigma_a} \approx \frac{\delta V_T}{V_T} + \frac{\delta\theta_h}{\theta_h}. \tag{A.28}$$

The wind speed used in (5.22) was measured by the ATI. This poses a random measurement uncertainty because the tower and radar were separated by roughly 200 m. For this problem I can use (A.7) by replacing $\overline{[f'(r)]^2}$ with σ_u^2. Using $\sigma_u^2 = 0.9$ m s^{-2}, $\lambda_l = 420$ m, $\delta = 200$ m, $U = 4.5$ m s^{-1}, and $T = 14$ min, I estimate the uncertainty in V_T caused by the separation between the tower and radar to be approximately 0.4 m s^{-1}, which gives a relative uncertainty of about 10%. Additional systematic measurement uncertainty in (5.22) comes from the relative uncertainty in the radar half-beamwidth, which I estimate to be 10%. The relative uncertainty in σ_a is then 14%, and the relative uncertainty in σ_a^2 is $2\delta\sigma_a/\sigma_a$, or 28%.

The corrections for spatial and temporal averaging are contained in (5.32). Because of the difficulty in defining the random errors in this equation, I analyze the random errors in the corrected form of the approximation given by Gossard et al. (1990) [see (5.36)]. Combining numerical constants and known parameters in (2.60) and (5.36), the path to C_u^2 for

the radar can be summarized by

$$C_u^2 = 2.08\varepsilon^{2/3} = \frac{\sigma_{11}^2}{1.04\gamma^2 a^{2/3} + 0.21(V_T t_D)^{2/3}} = \frac{\sigma_{11}^2}{D_1 + D_2}. \quad \textbf{(A.29)}$$

The uncertainty in C_u^2 is then expressed as

$$\delta C_u^2 = \frac{(D_1 + D_2)\delta\sigma_{11}^2 \pm \sigma_{11}^2(\delta D_1 + \delta D_2)}{(D_1 + D_2)^2}. \quad \textbf{(A.30)}$$

For this study, $D_1 = 8.53\ m^{2/3}$ and $D_2 = 3.63\ m^{2/3}$. In (5.21), we found that $\sigma_{11}^2 \approx \sigma_t^2 - \sigma_a^2$. Consequently,

$$\delta\sigma_{11}^2 = 2\sigma_{11}\delta\sigma_{11} \approx \sigma_t^2 \frac{\delta\sigma_t^2}{\sigma_t^2} \pm \sigma_a^2 \frac{\delta\sigma_a^2}{\sigma_a^2}. \quad \textbf{(A.31)}$$

In the discussion above I estimate the relative uncertainties in σ_t^2 and σ_a^2 to be 12% and 28%, respectively. The average spectral width (converted to variance) measured by the radar is $0.65\ m^2\ s^{-2}$. The value of σ_a^2 calculated from (5.22) using the average wind speed of $4.5\ m\ s^{-1}$ is $0.08\ m^2\ s^{-2}$. Therefore, $\delta\sigma_{11}^2 \approx 0.10\ m^2\ s^{-2}$. The average value of σ_{11}^2 calculated by taking the average difference between σ_t^2 and σ_a^2 is $0.54\ m^2\ s^{-2}$, such that the relative uncertainty in σ_{11}^2 is 19%. Note that approximately 65% of this error is due to random measurement uncertainty. The other 35%, which is due to the uncertainty in the radar beamwidth, is a systematic measurement uncertainty.

To determine δD_1, I start by noting that

$$\delta D_1 = D_1\left(\frac{2\delta\gamma}{\gamma} + \frac{2}{3}\frac{\delta a}{a}\right). \quad \textbf{(A.32)}$$

From (5.33) and to a first approximation, $\gamma \propto b/a$, such that

$$\frac{\delta\gamma}{\gamma} \approx \frac{\delta b}{b} - \frac{\delta a}{a}, \quad \textbf{(A.33)}$$

and thus,

$$\delta D_1 \approx D_1\left(\frac{2\delta b}{b} - \frac{4}{3}\frac{\delta a}{a}\right). \tag{A.34}$$

From (5.17), $a \propto R\theta_h$ and $b \propto \Delta R$, which gives us

$$\frac{\delta a}{a} \approx \frac{\delta R}{R} + \frac{\delta \theta_h}{\theta_h} \tag{A.35}$$

and

$$\frac{\delta b}{b} \approx \frac{\delta(\Delta R)}{\Delta R}. \tag{A.36}$$

These error estimates assume that the Gaussian pulse dimensions given by (5.17) accurately describe the actual shape of the radar pulse volume. Earlier, I estimated the relative uncertainties in R, θ_h, and ΔR to be 7%, 10%, and 10%, respectively. From (A.36), the relative uncertainty in b is 10%. By taking the sum of the squares of the relative uncertainties in R and θ_h, I estimate the relative uncertainty in a to be 12%. Because the errors in a and b are uncorrelated, the best estimate of the uncertainty in D_1 is found by taking the sum of the squares of the individual terms in (A.34). The result is given by $\delta D_1 = 0.26 D_1$. The uncertainty in D_2 is given by

$$\delta D_2 = \frac{2}{3}\frac{\delta V_T}{V_T} D_2 = 0.07 D_2. \tag{A.37}$$

Since δD_1 deals with uncertainties in the radar pulse volume dimensions, I classify it as a systematic measurement uncertainty. On the other hand, δD_2 is essentially the error in V_T, which I classified earlier as a random measurement uncertainty.

Substituting the values of D_1, D_2, $\delta\sigma_{11}^2$, δD_1, and δD_2 given above in (A.30), I obtain $\delta C_u^2 \approx 0.02$ m$^{4/3}$ s^{-2}. For $C_u^2 = 0.06$ m$^{4/3}$ s^{-2} (the average value measured by the radar), the relative uncertainty is 33%. Table A.1 summarizes the results of the entire error analysis.

Table A.1
Results of the error analysis.

	Random Errors		Systematic Errors	
	Sampling Uncertainty	Random Measurement Uncertainty	Instrument Uncertainty	Systematic Measurement Uncertainty
C_n^2	44%	9%	63%	4%
C_u^2	41%	16%	--	28%

*U.S.GOVERNMENT PRINTING OFFICE 1997-0-573-018/40037